NASA/CR—2004-213199/VOL6

# Numerical, Analytical, Experimental Study of Fluid Dynamic Forces in Seals

## Volume 6—Description of Scientific CFD Code SCISEAL

Mahesh Athavale and Andrzej Przekwas
CFD Research Corporation, Huntsville, Alabama

October 2004

The NASA STI Program Office . . . in Profile

Since its founding, NASA has been dedicated to the advancement of aeronautics and space science. The NASA Scientific and Technical Information (STI) Program Office plays a key part in helping NASA maintain this important role.

The NASA STI Program Office is operated by Langley Research Center, the Lead Center for NASA's scientific and technical information. The NASA STI Program Office provides access to the NASA STI Database, the largest collection of aeronautical and space science STI in the world. The Program Office is also NASA's institutional mechanism for disseminating the results of its research and development activities. These results are published by NASA in the NASA STI Report Series, which includes the following report types:

- TECHNICAL PUBLICATION. Reports of completed research or a major significant phase of research that present the results of NASA programs and include extensive data or theoretical analysis. Includes compilations of significant scientific and technical data and information deemed to be of continuing reference value. NASA's counterpart of peer-reviewed formal professional papers but has less stringent limitations on manuscript length and extent of graphic presentations.

- TECHNICAL MEMORANDUM. Scientific and technical findings that are preliminary or of specialized interest, e.g., quick release reports, working papers, and bibliographies that contain minimal annotation. Does not contain extensive analysis.

- CONTRACTOR REPORT. Scientific and technical findings by NASA-sponsored contractors and grantees.

- CONFERENCE PUBLICATION. Collected papers from scientific and technical conferences, symposia, seminars, or other meetings sponsored or cosponsored by NASA.

- SPECIAL PUBLICATION. Scientific, technical, or historical information from NASA programs, projects, and missions, often concerned with subjects having substantial public interest.

- TECHNICAL TRANSLATION. English-language translations of foreign scientific and technical material pertinent to NASA's mission.

Specialized services that complement the STI Program Office's diverse offerings include creating custom thesauri, building customized databases, organizing and publishing research results . . . even providing videos.

For more information about the NASA STI Program Office, see the following:

- Access the NASA STI Program Home Page at ***http://www.sti.nasa.gov***

- E-mail your question via the Internet to help@sti.nasa.gov

- Fax your question to the NASA Access Help Desk at 301–621–0134

- Telephone the NASA Access Help Desk at 301–621–0390

- Write to:
  NASA Access Help Desk
  NASA Center for AeroSpace Information
  7121 Standard Drive
  Hanover, MD 21076

NASA/CR—2004-213199/VOL6

# Numerical, Analytical, Experimental Study of Fluid Dynamic Forces in Seals

## Volume 6—Description of Scientific CFD Code SCISEAL

Mahesh Athavale and Andrzej Przekwas
CFD Research Corporation, Huntsville, Alabama

Prepared under Contract NAS3–25644

National Aeronautics and
Space Administration

Glenn Research Center

October 2004

Available from

NASA Center for Aerospace Information
7121 Standard Drive
Hanover, MD 21076

National Technical Information Service
5285 Port Royal Road
Springfield, VA 22100

Available electronically at http://gltrs.grc.nasa.gov

## FORWARD

The Computational Fluid Dynamics (CFD) computer codes and Knowledge-Based System (KBS) were generated under NASA contract NAS3-25644 originating from the Office of Advanced Concepts and Technology and administered through NASA-Lewis Research Center. The support of the Program Manager, Anita Liang, and the advice and direction of the Technical Monitor, Robert Hendricks, are gratefully appreciated. Major contributors to code development were:

- Dr. Bharat Aggarwal: KBS and OS/2 PC conversion of labyrinth seal code KTK
- Dr. Antonio Artiles: cylindrical and face seal codes ICYL and IFACE
- Dr. Mahesh Athavale and Dr. Andrzej Przekwas: CFD code SCISEAL
- Mr. Wilbur Shapiro: gas cylindrical and face seal codes GCYLT, GFACE, and seal dynamics code DYSEAL
- Dr. Jed Walowit: spiral groove gas and liquid cylindrical and face seal codes SPIRALG and SPIRALI.

The labyrinth seal code, KTK, was developed by Allison Gas Turbine Division of General Motors Corporation for the Aero Propulsion Laboratory, Air Force Wright Aeronautical Laboratories, Wright-Patterson Air Force Base, Ohio. It is included as part of the CFD industrial codes package by the permission of the Air Force.

## TABLE OF CONTENTS

TABLE OF CONTENTS
(continued)

## LIST OF FIGURES

## LIST OF FIGURES
(continued)

## LIST OF FIGURES
**(continued)**

# NOMENCLATURE

Roman Symbols

| | |
|---|---|
| A | Area |
| a | Link coefficient |
| C | Convective flux at a cell face, damping coefficient |
| $C_P$ | Specific heat at constant pressure |
| $C_{\varepsilon 1}$ | Coefficient of production of ε in ε-equation |
| $C_{\varepsilon 2}$ | Coefficient of destruction of ε in ε-equation |
| $C_\mu$ | Coefficient in the eddy viscosity relation in k-ε model |
| c | Species molar concentration |
| D | Diffusive flux at a cell face |
| d | damping coefficient or blending factor |
| $e_i$ | Covariant base unit vector |
| $e^i$ | Contravariant base unit vector |
| f | Mixture fraction |
| F | Seal pressure force |
| G | Mass flux at a cell face |
| g | Acceleration due to gravity |
| H | Stagnation or total enthalpy |
| h | Static enthalpy, magnitude of a covariant base vector |
| i | $\sqrt{-1}$ |
| K | Thermal conductivity, stiffness coefficient |
| k | Turbulent Kinetic Energy (TKE), stiffness coefficient |
| l | Turbulent length scale |
| M | Molecular weight, inertia coefficient |
| m | Mass, inertia coefficient |
| $n_i$ | Number of moles of $i^{th}$ species |
| P | Rate of production of turbulent kinetic energy |
| p | Pressure |
| q | Heat flux |
| R | Universal gas constant |
| Re | Reynolds number |
| $\vec{r}, \vec{R}$ | Radius, position vectors |

| | |
|---|---|
| $T$ | Temperature |
| $T^+$ | Normalized temperature in wall units |
| $t$ | time |
| $U$ | Contravariant component of velocity |
| $u$ | Cartesian component of velocity in x-direction |
| $u_i$ | Cartesian component of velocity in $i^{th}$ direction |
| $u_\tau$ | Friction velocity |
| $u^+$ | Normalized velocity in wall units |
| $V$ | Velocity vector |
| $v$ | Cartesian component of velocity in y-direction |
| $w$ | Cartesian component of velocity in z-direction |
| $x$ | Cartesian coordinate |
| $x_i$ | mole fraction of $i^{th}$ species |
| $Y_i$ | mass fraction of $^{th}$ species |
| $y$ | Cartesian coordinate |
| $y^+$ | Normalized distance from the wall in wall units |
| $z$ | Cartesian coordinate |

Greek Symbols

| | |
|---|---|
| $\alpha$ | Direction cosine |
| $\beta$ | Direction cosine, parameter in Osher-Chakravarthy scheme |
| $\Gamma$ | Diffusion coefficient |
| $\gamma$ | Direction cosine |
| $\varepsilon$ | Rate of turbulence dissipation |
| $\eta$ | Curvilinear coordinate |
| $\theta$ | Curvilinear coordinate |
| $\phi$ | Generic transport variable |
| $\kappa$ | Von-Karman constant |
| $\mu$ | Molecular (laminar) dynamic viscosity |
| $\mu_t$ | eddy (turbulent) dynamic viscosity |
| $\nu$ | Molecular (laminar) kinematic viscosity |
| $\nu_t$ | eddy (turbulent) kinematic viscosity |
| $\xi$ | Curvilinear coordinate |
| $\rho$ | Density |

| | |
|---|---|
| $\sigma$ | Laminar Prandtl or Schmidt number, scattering coefficient |
| $\sigma_t$ | Turbulent Prandtl or Schmidt number, scattering coefficient |
| $\tau_{ij}$ | Shear stress tensor |
| $\tau_w$ | Wall shear stress |
| $\omega$ | frequency, spin speed |
| $\Omega$ | Whirl speed |
| $\zeta$ | Curvilinear coordinate |

Subscripts

| | |
|---|---|
| E | Node or cell on the East side |
| e | Cell face on the East side |
| i | Cell or nodal index in $\xi$ direction |
| j | Cell or nodal index in $\eta$ direction |
| k | Cell or nodal index in $\zeta$ direction |
| N | Node or cell on the North side |
| n | Cell face on the North side |
| P | Node, cell center, or control volume |
| S | Node or cell on the South side |
| s | Cell face on the South side |
| W | Node or cell on the West side |
| w | Cell face on the West side |
| y, z | Cartesian y and z directions |

Superscripts

| | |
|---|---|
| n | Time level |
| + | Wall units |

## 1.0 INTRODUCTION

NASA's advanced engine programs are aimed at progressively higher efficiencies, greater reliability, and longer life. Recent studies have indicated that significant engine performance advantages can be achieved by employing advanced seals, and dramatic life extensions can also be achieved. Advanced seals are not only required to control leakage, but are necessary to control lubricant and coolant flow, prevent entrance of contamination, inhibit the mixture of incompatible fluids, and assist in the control of rotor response.

Recognizing the importance and need of advanced seals, NASA, in 1990, embarked on a five-year program (Contract NAS3-25644) to provide the U.S. aerospace industry with computer codes that would facilitate configuration selection and the design and application of advanced seals.

The program included four principal activities:

1. Development of a scientific code called SCISEAL, which is a Computational Fluid Dynamics (CFD) code capable of producing full three-dimensional flow field information for a variety of cylindrical configurations. The code is used to enhance understanding of flow phenomena and mechanisms, to predict performance of complex situations, and to furnish accuracy standards for the industrial codes. The SCISEAL code also has the unique capability to produce stiffness and damping coefficients that are necessary for rotordynamic computations.

2. Generation of industrial codes for expeditious analysis, design, and optimization of turbomachinery seals. The industrial codes consist of a series of separate stand-alone codes that were integrated by a Knowledge-Based System (KBS).

3. Production of a KBS that couples the industrial codes with a user friendly Graphical User Interface (GUI) that can in the future be

integrated with an expert system to assist in seal selection and data interpretation and provide design guidance.

4. Technology transfer via four multiday workshops at NASA facilities where the results of the program were presented and information exchanged among suppliers and users of advanced seals. A Peer Panel also met at the workshops to provide guidance and suggestions to the program.

This final report has been divided into separate volumes, as follows:

Volume 1: Executive Summary and Description of Knowledge-Based System
Volume 2: Description of Gas Seal Codes GCYLT and GFACE
Volume 3: Description of Spiral-Groove Codes SPIRALG and SPIRALI
Volume 4: Description of Incompressible Seal Codes ICYL and IFACE
Volume 5: Description of Seal Dynamics Code DYSEAL and Labyrinth Seal Code KTK
Volume 6: Description of Scientific CFD Code SCISEAL

This report summarizes the work performed on the Scientific Seals code (SCISEAL) under NASA Contract NAS3-25634, during the period of February 1990 to May 1995. The work for the first three years (February 1990 – September 1993) consisted of development of the single domain version of SCISEAL. Starting from REFLEQS-3D, a 3D code developed by CFDRC, several capabilities were added, which included Colocated grids, rotating frames, moving grids, high-order differencing and 2-layer turbulence models. Two rotordynamic coefficient calculation modules were added (whirling rotor method and N-S perturbation method), as well as other seal specific modules and boundary conditions. The preprocessor SCIPRE was modified to include automated grid generation capabilities for cylindrical seals. During the period of October 1994 – May 1995, upon recommendations from CFDRC, MTI and the Peer Review Committee, the code was enhanced by incorporation of multi-domain capability, ability to treat 2D and 3D problems, and extension of the rotordynamics modules to multi-domain format; this is the current status of SCISEAL.

## 2.0 CAPABILITIES

The objective of this task is to develop a 3-D CFD code for the analysis of fluid flows and forces in a variety of seals including cylindrical seals (tapered, annular, stepped) labyrinth seals, rim seals, tip seals and face seals. This code is to serve as a tool for detailed, and accurate analysis of flows in existing seal design as well as new concept seals. It can also be used as an accuracy check for the simplified Industrial codes which use simplified models for fast turnarounds. Finally, SCISEAL can be used to provide detailed flow analyses in secondary flow systems where seals are usually coupled with other flow elements such as disk cavities. Such systems need to be solved together and in a coupled manner, which is currently beyond the capabilities of the seals codes based on the simplified flow models.

The solver module consists of two separate codes:

a. The preprocessor SCIPRE, which reads in an input file in a text format and converts it into another file that is readable by the main flow solver. The preprocessor has capabilities of grid generation, problem setup, boundary condition setup and checks for internal consistency for the problem as defined by the user in the input file. Detailed descriptions of problem setup, command structure *etc.* is given in the Users' Manual for the SCISEAL code.[1]

b. Flow solver SCISEAL is the module which reads in the data files created by the preprocessor and does the flow computations. At the end of execution of SCISEAL, a number of output files are created that can be used for restarting a continuation run and plotting with graphical packages; these files also contain information on code convergence and integrated seal quantities. A description of the various files also is given in the SCISEAL Users' Manual.

### 2.1 Salient Features of SCISEAL

The flow solver, SCISEAL, was written in ANSI FORTRAN-77 with emphasis on portability and modularity. The basic flow analysis methodology utilizes advanced

numerical techniques for accuracy, efficiency and robustness. Features of the code include:

- Finite volume discretization for integration of Favre-averaged Navier-Stokes (N-S) flow equations;
- Implicit multi-domain treatment with one-to-one and one-to-many cell connections at the interfaces;
- Cartesian, polar, and non-orthogonal Body-Fitted Coordinates (BFC).
- Colocated (non-staggered) grid;
- Strong conservative form of momentum equations with Cartesian components as dependent variables;
- Stationary as well as rotating frames of reference for rotary flow problems;
- Pressure-based solution algorithm including a variant of SIMPLEC and PISO, which allows the treatment of both incompressible and compressible flows;
- Concentrated and distributed porosity-resistivity technique for treatment of internal solid objects;
- High order spatial differencing schemes (including upwind, central, MUSCL and Osher-Chakravarthy) and temporal schemes (Euler backwards and Crank-Nicholson);
- Steady-State and time-accurate solution capability;
- A space-conserving moving grid formulation that allows the treatment of moving-deforming grid systems encountered with whirling rotor; and
- Symmetric whole-field equation solvers based on Stone's implicit methods and a conjugate gradient squared solver for linear equation solutions.

The SCISEAL code also has a variety of physical models that are needed in the solutions of the flows encountered in seals. These models include:

- JANNAF property tables for selected species, useful in tracer gas simulations with passive scaler transport;
- Variable viscosity with Sutherland's Law;
- Advanced turbulence models:

  - Mixing length model (Baldwin and Lomax)
  - Standard k-ε model with wall functions (Launder and Spalding)
  - Low-Reynolds number k-ε model (Chien)
  - 2-layer k-ε model for rotating flows and for narrow flow passages
- Isotropic surface roughness treatment; and
- Comprehensive set of boundary conditions including seal specific conditions such as:
  - pre-swirl specifications
  - entrance loss factor.

## 2.2 Seal Rotordynamics

The flow changes in seals due to rotor motion can generate significant fluid force changes and affect the overall stability of the rotor system. This effect is introduced through the seal rotordynamic coefficients, and two methods are available in SCISEAL to calculate the coefficients:

a. Whirling rotor method: This method uses full CFD solutions for a nominally centered rotor whirling in a circular orbit. the solution method provides the skew-symmetric set of rotordynamic coefficients associated with a centered rotor.

b. Small perturbation method: The N-S equations are perturbed to generate 1st order flow equations that describe the flow changes due to small rotor motions. These equations are solved to generate the full set of rotordynamic coefficients. This method can be used to treat both centered and eccentric seals.

Both of the methods are fully automated and can be invoked with simple commands in the input file.

Several additional features that are available for seals problems are:

- Easy grid generation setup for cylindrical seals;
- Calculation of seal loads, torque and power; and

- Facility to read externally created seal grids and use into flow as well as rotordynamics modules.

The following section describes the treatment of flow equations, discretization methods and boundary conditions treatment. Descriptions of the physical models used in the code and the rotordynamics models follow the numerical models.

An extensive series of validation and demonstration problems were solved using SCISEAL to assess the accuracy of the numerical and physical models and a list of these problems is included in Section 4, with a brief description and relevant results for each of these problems.

# 3.0 THEORY

## 3.1 Geometry and Flow-Domain Modeling

The SCISEAL code uses a structured grid approach to discretize a given flow domain. Several powerful concepts have been built into the code to simplify the grid generation procedure, optimize the cell numbers and allow for simpler problem definition. these capabilities are:

a. Generalized non-orthogonal Body-fitted-coordinate (BFC) grids;
b. Multi-domain capability; and
c. Internal blockage concept.

Given a complex flow domain, one or more of these capabilities can be utilized to simplify the grid generation process for optimum and accurate flow solutions. This section deals with geometry definition, BFC grids, multi-domain approach and the internal blockage concept.

### 3.1.1 Geometry and Grid Generation

The seals code uses a finite volume approach, where the flow domain is discretized into a number of cells or finite volumes and the flow equations are numerically integrated over each finite volume. The discrete representation of the flow domain in the computational grid. Furthermore, the grid needs to be of a structured form. A grid is considered to be structured if there exists three grid lines (for a 3D problem) to identify three distinctive directions and any face of a control volume is on two grid lines. In other words, a single (i,j,k) index can be used to identify a cell or a point of a structured grid.

The structured grids can further be divided into single block or multi-block types. The single block (or domain) grid has only one set of **i**, **j** and **k** index axes over the complete domain. A multi-block grid has several blocks with individual definitions of **i**, **j**, and **k** axes, with interfaces at places where the blocks meet. The orientation of the axes in the individual blocks is independent of the neighboring blocks. This concept is illustrated in Figure 1.

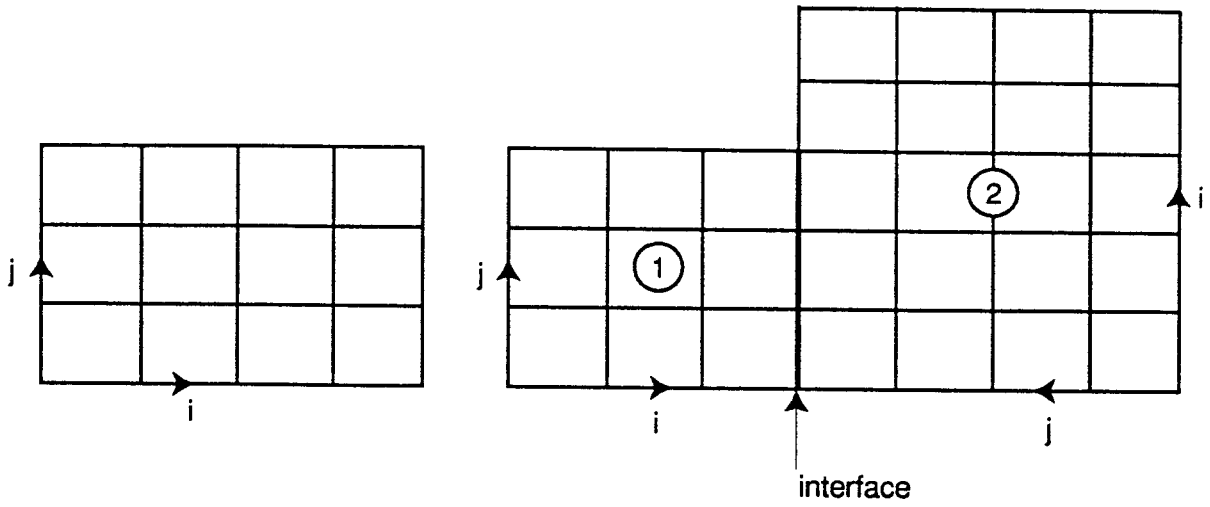


Figure 1. Single and Multiblock Grid Concept

The ability to divide a complex flow problem into several domains is very powerful, since this capability allows the user to use grids only on flow areas for optimum cell numbers. In addition, the division of flow problem can be made such that the grids stay as near orthogonal as possible, *i.e.* the grid quality can be improved. The current capabilities include a one-to-one match as well as a one-to-multi match of cells at the interface. This concept is shown in Figure 2.

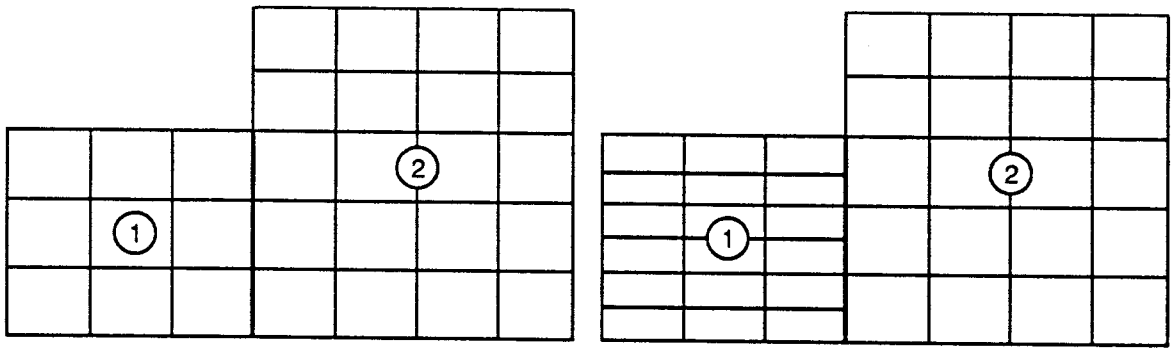


(a) one-to-one interface (b) one-to-many interface

Figure 2. Types of Interfaces Allowed in SCISEAL

The ability to locally refine the grids at domain interfaces further enhances the code capabilities. Several seal applications have flow domains where a relatively large

domain interfaces with a narrow domain, and the multi-to-one interface can be used to provide sufficient resolution in the narrow passage, and also reduce the number of cells in the large passage through a multi-to-one connection at the interface.

### 3.1.2 Coordinate Systems

When solving complex flow problems, definition of curved boundary surfaces with Cartesian rectangular grids is difficult and will result in accuracy loss. To be able to follow curved lines/surfaces in the flow domain, the so-called body-fitted coordinate (BFC) system is necessary. The BFC grids also have 2/3 coordinate axes, however they may not necessarily be parallel to any Cartesian axes and may not be locally orthogonal to each other. The SCISEAL code has the options to treat Cartesian, orthogonal BFC as well as non-orthogonal BFC grids, and such grids can be used in conjunction with the multi-domain capability. Cartesian grids require least storage and yield highest accuracy, and non-orthogonal BFC grids require the highest storage.

Mathematically, a BFC system can be viewed as a coordinate transformation from physical domain to computational domain as illustrated in Figure 3 for a seal sector grid. The $\eta$ and $\zeta$ coordinates run along the radial and circumferential direction and have a direct correlation with the **j** and **k** indices. The axial grid lines run along the $\xi$ direction and are related to the **i** index. The grid is always represented in a Cartesian system in the physical domain. The coordinate transformation converts this curvilinear grid to an orthogonal grid in the transformed space.

$$\begin{aligned} &\xi = \xi(x, y, z),\ \eta = \eta(x, y, z),\ \zeta = \zeta(x, y, z) \\ &\textit{or}\quad x = X(\xi, \eta, \zeta),\ y = Y(\xi, \eta, \zeta),\ z = Z(\xi, \eta, \zeta) \end{aligned} \tag{1}$$

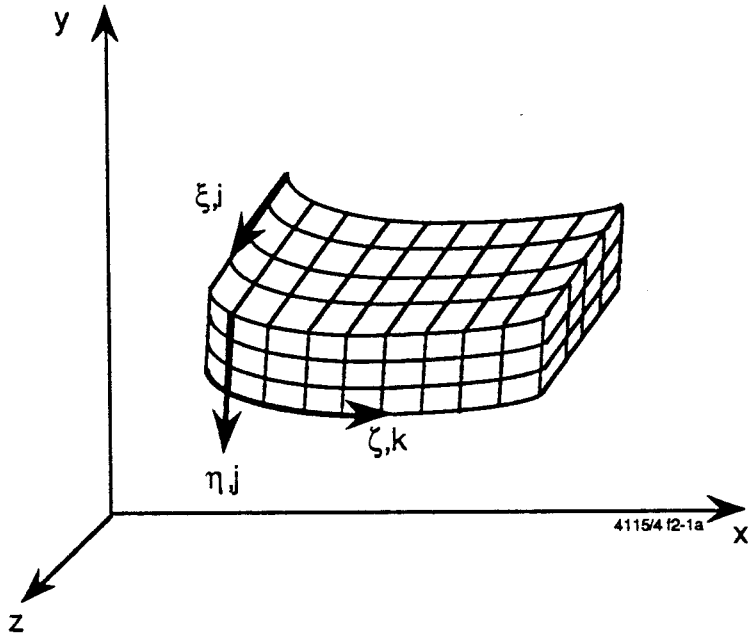


(a) physical domain

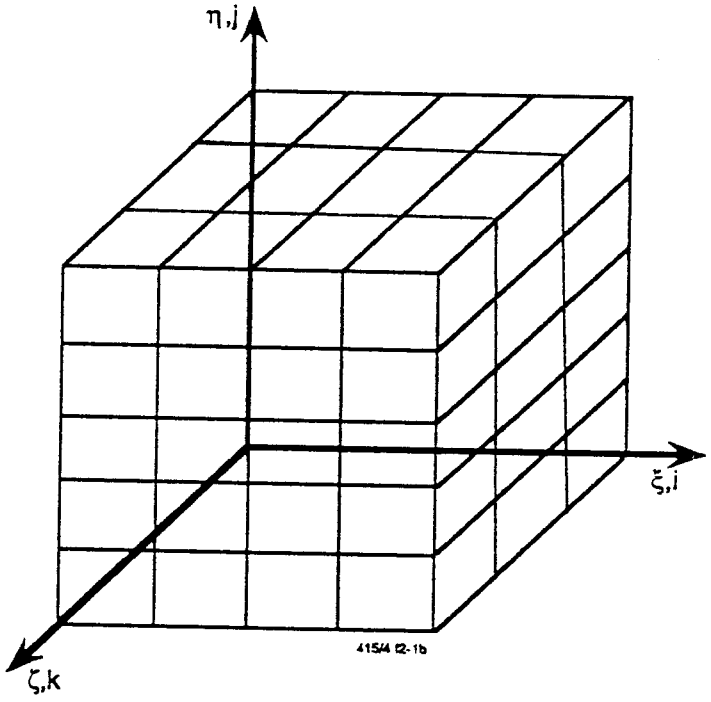


(b) computational domain

Figure 3. An Illustration of the Transformation from Physical to Computational Domain for a Seal Sector Grid

Therefore, each point on a physical domain can be identified by a triplet (x, y, z). This triplet is a function of $\xi$, $\eta$ and $\zeta$ or is associated with a particular (i, j, k) index. Thus SCISEAL works on a BFC grid system expressed on a base Cartesian coordinate system. Note that a physical domain is always transformed to a rectangular domain as shown in Figure 3.

For future reference, a brief introduction of the BFC coordinate system is given below. A comprehensive description of BFC coordinate system can be found in the work of Thompson *et al*.,[2] For derivation convenience, ($\xi_1$ $\xi_2$, $\xi_3$) is used to replace ($\xi$, $\eta$, $\zeta$). In a BFC coordinate system, ($\xi_1$, $\xi_2$, $\xi_3$), the covariant base vectors are defined as

$$\vec{\varepsilon}_j = \frac{\partial \vec{r}}{\partial \xi_j} \; ; j = 1, 2, 3 \tag{2}$$

where $\vec{r}$ is the displacement vector and is equal to $x\,\hat{i} + y\,\hat{j} + z\,\hat{k}$ , and contravariant base vectors are defined as

$$\vec{\varepsilon}^1 = \frac{\vec{\varepsilon}_2 \times \vec{\varepsilon}_3}{J} \; ; \; \vec{\varepsilon}^2 = \frac{\vec{\varepsilon}_3 \times \vec{\varepsilon}_1}{J} \; ; \; \vec{\varepsilon}^3 = \frac{\vec{\varepsilon}_1 \times \vec{\varepsilon}_2}{J} \tag{3}$$

where $J$ is the Jacobian defined as $J = (\vec{\varepsilon}_1 \times \vec{\varepsilon}_2) \cdot \vec{\varepsilon}_3$ . Basically, $\varepsilon_j$ is a base vector along $\xi_j$ coordinate line and $\vec{\varepsilon}^j$ is a base vector normal to the surface formed by $\vec{\varepsilon}_i$ and $\vec{\varepsilon}_k (i \neq j \neq k)$ . But note that $\varepsilon_j$ and $\vec{\varepsilon}^j$ are not unit bases and unit bases can be defined as

$$\vec{e}_j = \frac{\vec{\varepsilon}_j}{h_j} \; , h_j = |\vec{\varepsilon}_j| = \sqrt{\left(\frac{\partial x}{\partial \xi_1}\right)^2 + \left(\frac{\partial y}{\partial \xi_2}\right)^2 + \left(\frac{\partial z}{\partial \xi_3}\right)^2} \tag{4}$$

and

$$\vec{e}^{\,j} = \frac{\vec{\varepsilon}^{\,j}}{\left|\vec{\varepsilon}^{\,j}\right|} \quad (no\ summation\ on\ j) \tag{5}$$

where $h_j$ is usually called scale factors.

It is easy to show that the covariant and contravariant base vectors satisfy the basic relationship:

$$\vec{\varepsilon}_i \cdot \vec{\varepsilon}^{\,j} = \delta_{ij} \tag{6}$$

where $\delta_{ij}$ is the Kronecker delta.

In the BFC system, the gradient, divergence, curl, and Laplacian operators can be expressed in conservative form as

Gradient: $$\nabla f = \frac{1}{J}\frac{\partial}{\partial \xi_k}\left(J\vec{\varepsilon}^{\,k} f\right) \tag{7}$$

Divergence: $$\nabla \cdot \vec{V} = \frac{1}{J}\frac{\partial}{\partial \xi_k}\left(J\vec{\varepsilon}^{\,k} \cdot \vec{V}\right) \tag{8}$$

Curl: $$\nabla \times \vec{V} = \frac{1}{J}\frac{\partial}{\partial \xi^k}\left(J\,\vec{\varepsilon}^{\,k} \times \vec{V}\right) \tag{9}$$

Laplacian: $$\nabla^2 f = \frac{1}{J}\frac{\partial^2}{\partial \xi^i \partial \xi^j}\left[J f\,\vec{\varepsilon}^{\,i} \cdot \vec{\varepsilon}^{\,j}\right] \tag{10}$$

The geometric meaning of the above quantities can be easily explained on 2D curvilinear coordinates at point P as shown in Figure 4. For a BFC grid, the Jacobian is simply the volume of each cell.

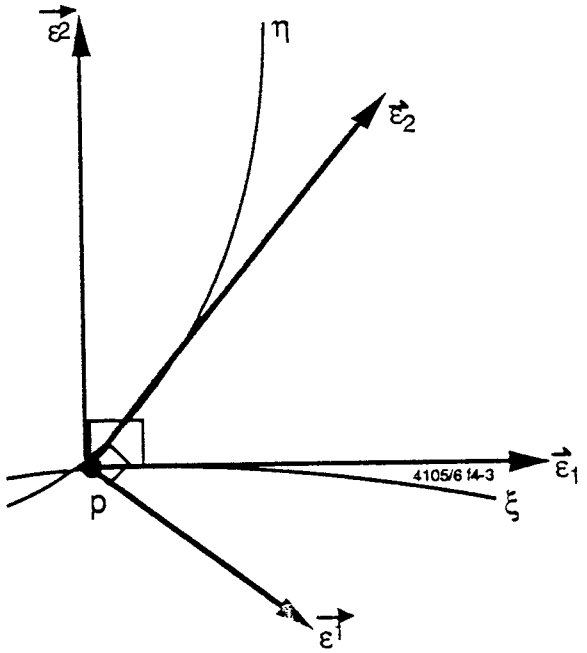


Figure 4. Geometrical Meaning of Covariant and Contravariant Bases for a 2D BFC System

### 3.1.3 Blockage Concept

In many engineering problems the boundaries of the flow problems can be very complicated, and there can be internal solid obstacles. In some cases such obstacles also need to be included for performing conjugate heat transfer analysis. Treatment of such internal objects can either be done through using the multi-domain approach or through using the so-called blockage concept. With blockage capability, several parts of the flow domain can be excluded from the calculations or such parts can be treated as solids, to be included in the flow calculations for conjugate heat transfer. The blocked region concept is particularly useful in the treatment of seals such as stepped cylindrical seals and labyrinth seals. A labyrinth seal is shown in a section along the axis in Figure 5.

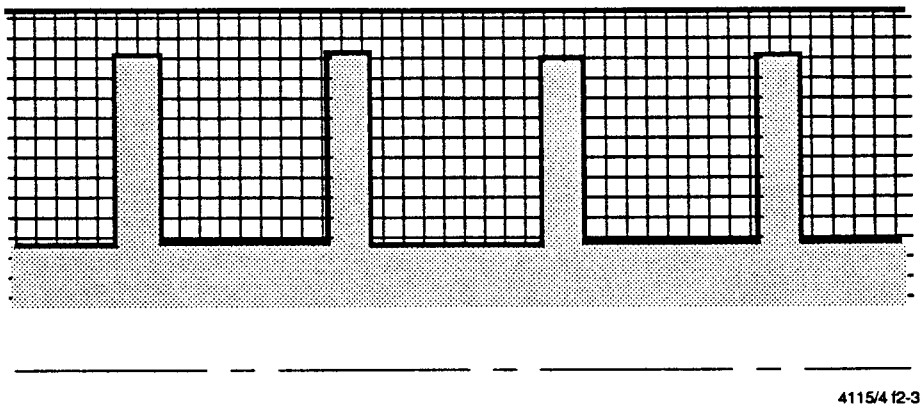


Figure 5. Cross-Sectional View of a Labyrinth Seal with Blocked Cells for Teeth Region

In such a problem, a BFC grid can also be employed to cover the computational domain, however, such a grid is difficult to generate, and will have very skewed cells, especially near the corners, which can affect the solution accuracy. With the blocked-cell concept a Cartesian orthogonal grid can be utilized. The computational cells in the labyrinth seal teeth now can be treated as blocked-off or included in the energy equation for conjugate heat transfer. In this case, use of orthogonal grid both yields ease of grid generation, better accuracy and computational speed, although the blocked cells do represent a penalty in terms of computational effort needed to treat non-flow cells.

### 3.2 Basic Governing Equations

The fluid flows are simulated by numerically solving partial differential equations that govern the transport of flow variables. These variables include mass, momentum, energy, turbulence quantities, and mixture fractions. The variables for which transport equations have to be solved will depend on the nature of the flow problem. In this section, the basic governing equations for the conservation of mass, momentum, energy are presented. The user will be introduced to the transport equations for other flow variables such as turbulence quantities in a following sub-section.

SCISEAL employs conservative finite-volume methodology and accordingly all the governing equations are expressed in conservative form. Cartesian coordinate

system and tensor notation are generally employed in which repeated indices imply summation over all coordinate directions. The user should note that SCISEAL solves the governing equations in cylindrical coordinate system for 2D axisymmetric flow problems. Presented here are the flow equations that correspond to the 3D representation.

### 3.2.1 Continuity Equation

In any fluid flow in which the continuum hypothesis holds mass conservation can be expressed as

$$\frac{\partial \rho}{\partial t} + \frac{\partial}{\partial x_j}(\rho u_j) = 0 \tag{11}$$

where $u_j$ is the $j^{th}$ Cartesian component of the instantaneous velocity, and $\rho$ is the fluid density.

### 3.2.2 Momentum Equations

These equations are derived from the law of conservation of momentum.

$$\frac{\partial}{\partial t}(\rho u_i) + \frac{\partial}{\partial x_j}(\rho u_i u_j) = -\frac{\partial p}{\partial x_i} + \frac{\partial \tau_{ij}}{\partial x_j} + \rho f_i \tag{12}$$

In the preceding equation $p$ is the static pressure, $\tau_{ij}$ is the viscous stress tensor and $f_i$ is the body force. The viscous shear stress, $\tau_{ij}$, is related to the mean shear rate (strain rate) tensor, $\gamma_{ij}$, by

$$\tau_{ij} = \mu\gamma_{ij} - \frac{2}{3}\mu\frac{\partial u_k}{\partial x_k}\delta_{ij} \tag{13}$$

where $\delta_{ij}$ is the Kronecker delta and

$$\gamma_{ij} = \left(\frac{\partial u_i}{\partial x_j} + \frac{\partial u_j}{\partial x_i}\right) \tag{14}$$

and $\mu$ is the fluid dynamic viscosity which, in general, can be a function of temperature, species composition, position, shear rate, *etc*. If viscosity does not depend on shear rate, the fluid is called Newtonian and $\tau_{ij}$ is a linear function of velocity gradients

$$\tau_{ij} = \mu\left(\frac{\partial u_i}{\partial x_j} + \frac{\partial u_j}{\partial x_i}\right) - \frac{2}{3}\mu\left(\frac{\partial u_k}{\partial x_k}\right)\delta_{ij} \tag{15}$$

Substitution of Equation (15) in Equation (12) results in the Navier-Stokes Equations

$$\frac{\partial}{\partial t}(\rho u_i) + \frac{\partial}{\partial x_j}(\rho u_i u_j) = -\frac{\partial p}{\partial x_i} + \frac{\partial}{\partial x_j}\left\{\mu\left(\frac{\partial u_i}{\partial x_j} + \frac{\partial u_j}{\partial x_i}\right) - \frac{2}{3}\mu\frac{\partial u_k}{\partial x_k}\delta_{ij}\right\} + \rho f_i \tag{16}$$

### 3.2.3 Energy Equation

The equation for the conservation of energy can take several forms and different forms are suitable for different classes of problems. In SCISEAL, the user may choose either *static enthalpy* or *stagnation enthalpy* depending on the application. The static enthalpy form of the energy equation can be expressed as

$$\frac{\partial}{\partial t}(\rho h) + \frac{\partial}{\partial x_j}(\rho u_j h) = -\frac{\partial q_j}{\partial x_j} + \frac{\partial p}{\partial t} + u_j\frac{\partial p}{\partial x_j} + \tau_{ij}\frac{\partial u_i}{\partial x_j} \tag{17}$$

Here, $q_j$ is the j-component of the heat flux. Fourier's Law is employed to model the heat flux

$$q_j = -K\frac{\partial T}{\partial x_j} \tag{18}$$

where $K$ is the thermal conductivity. By algebraic manipulation, the heat flux can be expressed in terms of the enthalpy gradient as shown below.

$$q_j = -\frac{K}{C_p}C_p\frac{\partial T}{\partial x_j} = -\Gamma\frac{\partial h}{\partial x_j} \tag{19}$$

Here $C_p$ is the fluid specific heat and $\Gamma$ is known as the diffusion coefficient and is related to the fluid dynamic viscosity through the Prandtl number $\sigma$.

$$\Gamma = \frac{K}{C_p} = \frac{\mu}{\sigma} \tag{20}$$

The static enthalpy equation can be rewritten as

$$\frac{\partial}{\partial t}(\rho h) + \frac{\partial}{\partial x_j}(\rho u_j h) = \frac{\partial}{\partial x_j}\left(\Gamma \frac{\partial h}{\partial x_j}\right) + \frac{\partial p}{\partial t} + u_j \frac{\partial p}{\partial x_j} + \tau_{ij} \frac{\partial u_i}{\partial x_j} \tag{21}$$

Note that the above equation is not strictly conservative by its nature and is recommended for incompressible and low Mach number flows. On the other hand, the total enthalpy form of the energy equation is fully conservative and is recommended for high speed compressible flows. The total enthalpy $H$ is defined as

$$H = h + \frac{u_j u_j}{2} \tag{22}$$

and the governing equation for $H$ is obtained by adding the fluid kinetic energy equation to the static enthalpy equation

$$\frac{\partial}{\partial t}(\rho H) + \frac{\partial}{\partial x_j}(\rho u_j H) = \frac{\partial}{\partial x_j}\left(\Gamma \frac{\partial H}{\partial x_j}\right) + \frac{\partial}{\partial x_j}\left\{(\mu - \Gamma)\frac{\partial}{\partial x_j}\left(\frac{1}{2} u_k u_k\right)\right\} + \frac{\partial p}{\partial t} + \frac{\partial}{\partial x_i}(\tau_{ij} u_j) \tag{23}$$

### 3.2.4 Favre Averaged Equations

The fundamental equations of fluid dynamics that have been introduced in the preceding sections are, in general, applicable to Newtonian fluid flow under steady or transient, incompressible or compressible, laminar, transitional or turbulent conditions. The nonlinearity of the Navier-Stokes equations, coupled with the

complexity of the boundary conditions, makes it impossible to obtain analytical solutions for all but a limited number of flows of engineering interest. Hence one is forced to resort to approximate or numerical methods. As most engineering applications only require time-mean quantities, the Navier-Stokes equations are usually averaged over time or ensemble of statistically equivalent flows to yield averaged equations. In the averaging process, a flow quantity $\phi$ is decomposed into mean and fluctuating parts. The following two types of averaging are generally used.

Reynolds (or time) Averaging:

$$\phi = \bar{\phi} + \phi' \text{ where } \bar{\phi} = (1/T)\int_{t_o}^{t_o+T} \phi\, dt \tag{24}$$

Favre (or density) Averaging:

$$\phi = \tilde{\phi} + \phi'' \text{ where } \tilde{\phi} = \overline{\rho\phi}/\bar{\rho} \tag{25}$$

Note that overbar denotes Reynolds averaging while tilde denotes Favre averaging. The time period of averaging, $T$, should be large compared to the fluctuation time scale so that mean quantities are stationary over a number of samples. The user also should bear in mind that the mean quantities can vary in time on a scale much larger than $T$.

Applying the Favre averaging procedure to Equation (11), we get the Favre-averaged continuity equation

$$\frac{\partial \bar{\rho}}{\partial t} + \frac{\partial}{\partial x_j}\left(\bar{\rho}\,\tilde{u}_j\right) = 0 \tag{26}$$

Similarly when the Navier-Stokes equations (Equation 12) are averaged, we obtain the Favre-averaged Navier-Stokes (FANS) equations given below. (For detailed derivation, see Cebeci and Smith[3]).

$$\frac{\partial}{\partial t}\left(\bar{\rho}\,\tilde{u}_j\right) + \frac{\partial}{\partial x_j}\left(\bar{\rho}\,\tilde{u}_i\,\tilde{u}_j\right) = -\frac{\partial \bar{p}}{\partial x_i} + \frac{\partial}{\partial x_j}\left[\bar{\mu}\left(\frac{\partial \tilde{u}_i}{\partial x_j} + \frac{\partial \tilde{u}_j}{\partial x_i} - \frac{2}{3}\frac{\partial \tilde{u}_m}{\partial x_m}\delta_{ij}\right)\right] + \frac{\partial}{\partial x_j}\left(-\bar{\rho}\,\widetilde{u_i'' u_j''}\right) \tag{27}$$

The FANS equations contain less information than the full NS equations, but have additional unknown terms $-\bar{\rho}\widetilde{u_i''u_j''}$ called the Reynolds stresses. These correlations between the fluctuating components arise in the averaging process, and need to be modeled to achieve closure of the FANS equations. All the turbulence models available in SCISEAL employ the generalized Boussinesq eddy viscosity concept in which the Reynolds stress $-\bar{\rho}\widetilde{u_i''u_j''}$ is treated as a linear function of the mean strain rate

$$-\bar{\rho}\widetilde{u_i''u_j''} = \mu_t\left(\frac{\partial\tilde{u}_i}{\partial x_j} + \frac{\partial\tilde{u}_j}{\partial x_i} - \frac{2}{3}\frac{\partial\tilde{u}_m}{\partial x_m}\delta_{ij}\right) - \frac{2}{3}\bar{\rho}k\,\delta_{ij} \tag{28}$$

Here $\mu_t$ is known as the turbulent eddy viscosity and $k$ is half the trace of the Reynolds stress tensor.

$$k = \frac{1}{2}\widetilde{u_k''u_k''} \tag{29}$$

By substituting Equation (28) in Equation (27), we obtain the modeled FANS equations

$$\frac{\partial}{\partial t}\left(\bar{\rho}\tilde{u}_j\right) + \frac{\partial}{\partial x_j}\left(\bar{\rho}\tilde{u}_i\tilde{u}_j\right) = -\frac{\partial\bar{p}}{\partial x_i} + \frac{\partial}{\partial x_j}\left[\left(\bar{\mu} + \mu_t\right)\left(\frac{\partial\tilde{u}_i}{\partial x_j} + \frac{\partial\tilde{u}_j}{\partial x_i} - \frac{2}{3}\frac{\partial\tilde{u}_m}{\partial x_m}\delta_{ij}\right)\right] - \frac{2}{3}\frac{\partial}{\partial x_i}\left(\bar{\rho}k\right) \tag{30}$$

When the averaging procedure is applied to the static enthalpy equation, additional terms containing fluctuating enthalpy and velocity components appear which are generally modeled with the Boussinesq concept as follows

$$-\bar{\rho}\widetilde{u_j''h''} = \Gamma_t\frac{\partial\tilde{h}}{\partial x_j} \tag{31}$$

The term $\Gamma_t$ is known as the turbulent or eddy diffusivity and is related to the turbulent viscosity through the turbulent Prandtl number $\sigma_t$.

$$\Gamma_t = \frac{\mu_t}{\sigma_t} \tag{32}$$

The mean total enthalpy equation is derived by adding the mean kinetic energy equation to the mean static enthalpy equation. Without any formal derivation, the modeled mean enthalpy equations are

$$\frac{\partial \bar{\rho}\tilde{h}}{\partial t} + \frac{\partial}{\partial x_j}\left(\bar{\rho}\tilde{u}_j\tilde{h}\right) = \frac{\partial}{\partial x_j}\left\{\left(\Gamma + \Gamma_t\right)\frac{\partial \tilde{h}}{\partial x_j}\right\} + \frac{\partial \bar{p}}{\partial t} + \tilde{u}_j\frac{\partial \bar{p}}{\partial x_j} + \left(\bar{\mu} + \mu_t\right)\frac{\partial \tilde{u}_i}{\partial x_j}\left(\frac{\partial \tilde{u}_i}{\partial x_j} + \frac{\partial \tilde{u}_j}{\partial x_i} - \frac{2}{3}\frac{\partial \tilde{u}_k}{\partial x_k}\delta_{ij}\right) \tag{33}$$

$$\frac{\partial \bar{\rho}\tilde{H}}{\partial t} + \frac{\partial}{\partial x_j}\left[\bar{\rho}\,\tilde{u}_j\tilde{H}\right] = -\frac{\partial}{\partial x_j}\left\{\left(\Gamma+\Gamma_t\right)\frac{\partial \tilde{H}}{\partial x_j}\right\} + \frac{\partial}{\partial x_j}\left\{\left(\mu - \Gamma + \mu_t - \Gamma_t\right)\frac{\partial}{\partial x_j}\left(\frac{1}{2}\tilde{u}_k\tilde{u}_k\right)\right\} + \frac{\partial \bar{p}}{\partial t}$$
$$+ \frac{\partial}{\partial x_j}\left\{\left(\mu + \mu_t\right)\tilde{u}_i\left(\frac{\partial \tilde{u}_i}{\partial x_j} + \frac{\partial \tilde{u}_j}{\partial x_i} - \frac{2}{3}\frac{\partial \tilde{u}_k}{\partial x_k}\delta_{ij}\right)\right\} \tag{34}$$

Various models differ in the way $\mu_t$ is estimated. The models employed in SCISEAL are discussed in a subsequent section.

### 3.3 Discretization Methods

The fluid flows are governed by several physical conservation laws and these laws can be written as Partial Differential Equations (PDE's) as presented in Section 3.2 A numerical method to solve these PDE's consists of the discretization of the PDE's on a given grid, formation of corresponding linearized algebraic equations, and the solution of the algebraic equations. This way, a final set of discrete numbers on a grid is obtained which represents the numerical solution of the PDE's. In this section, the discretization of the governing equations is presented. The finite-volume approach is adopted due to its attractive capability of preserving the conservation property. In the following, the storage locations of the dependent variables are first discussed. The discretization process then follows in more detail.

### 3.3.1 Staggered Versus Colocated Grid Approach

A detailed description of this method was provided in the First Interim Report[4] and only a short description is given below for brevity. The staggered grid approach was widely used for incompressible flow simulations in the past. With the staggered grid approach, proposed by Harlow and Welch[5], the velocity components are stored at positions between the pressure nodes as illustrated in Figure 6a. Such an approach ensures that the pressure is readily available for momentum equations and velocity components are available for the continuity equation without interpolation. As a result, a proper pressure coupling is guaranteed and the well-known checkerboard instability is prevented. However, the disadvantages of the staggered grid approach are well known and the following are just two examples.

- It is not easy to extend the staggered grid approach to non-orthogonal curvilinear grids. Several proposed extensions are extremely complex to apply and can cause loss of accuracy.
- Many state-of-the-art CFD methodologies are difficult to apply with a staggered grid approach such as multigrid, local grid refinement, and multi-zoning.

The current state-of-the-art approach is based on the Colocated grid (or non-staggered grid) proposed by Rhie and Chow[6] and later by Peric.[7] The grid arrangement of this approach is illustrated in Figure 6b. This Colocated grid approach has many advantages over the staggered grid approach and is used in the seals code. This approach evaluates the cell face velocity using momentum equations and consequently the cell face velocity is directly linked to a third-order pressure derivative term. This linkage ensures that the checkerboard instability is eliminated. With a Colocated grid approach and Cartesian components as dependent velocity variables, many coding complications are avoided and more accurate solutions can be obtained, particularly for viscous flows.

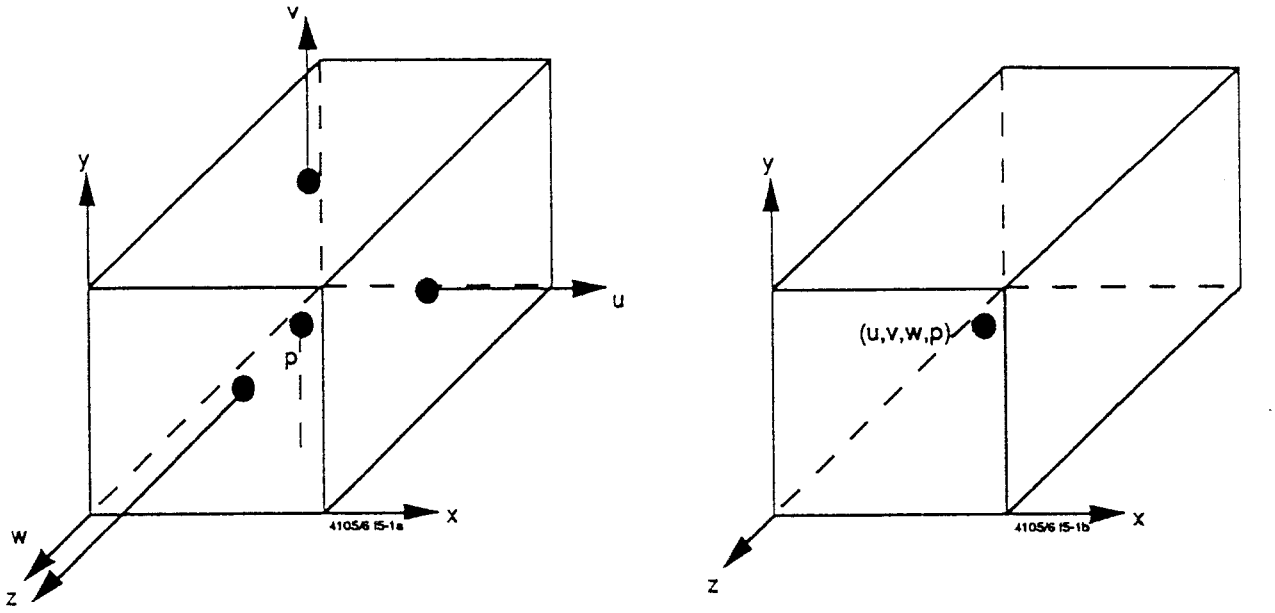


Figure 6. Illustration of Variable Storage Locations for: (a) Staggered; and (b) Colocated Grid

### 3.3.2 A General Convection-Diffusion Equation

It is noted that all governing equations, except continuity equation, can be expressed in a general form as

$$\frac{\partial \rho\phi}{\partial t} + \frac{\partial \rho u\phi}{\partial x} + \frac{\partial \rho v\phi}{\partial y} + \frac{\partial \rho w\phi}{\partial z} = \frac{\partial}{\partial x}\left(\Gamma \frac{\partial \phi}{\partial x}\right) + \frac{\partial}{\partial y}\left(\Gamma \frac{\partial \phi}{\partial y}\right) + \frac{\partial}{\partial z}\left(\Gamma \frac{\partial \phi}{\partial z}\right) + S_\phi \qquad (35)$$

where $\phi$ can stand for Cartesian velocity components, total enthalpy, turbulence kinetic energy, mass concentration, *etc.* $\Gamma$ is the effective diffusivity and $S_\phi$ is the source term. Therefore, the above equation, in convection-diffusion form, will be considered for discretization. The continuity equation has a different form, and will be discussed in a later section.

First of all, Equation (35) needs to be transformed to BFC coordinates using the new independent variable $\xi(x, y, z)$, $\eta(x, y, z)$, and $\zeta(x, y, z)$. Without detailed derivation, it is sufficient to write down the transformed equation in $(\xi, \eta, \zeta)$ coordinates as follows

$$\frac{1}{J}\frac{\partial}{\partial t}(J\rho\phi)+\frac{1}{J}\frac{\partial}{\partial \xi_k}\left\{J\rho\left(\vec{V}\cdot\vec{\varepsilon}^{k}\right)\phi\right\}=\frac{1}{J}\frac{\partial}{\partial \xi_k}\left[\Gamma J g^{jk}\frac{\partial\phi}{\partial \xi_j}\right]+S_\phi \tag{36}$$

with

$$g^{jk}=\vec{\varepsilon}^{j}\cdot\vec{\varepsilon}^{k} \tag{37}$$

The discretization involves an integration of Equation (36) over a control volume as shown in Figure 7. That is:

$$\iiint_{v}\left[\frac{1}{J}\frac{\partial}{\partial t}(J\rho\phi)+\frac{1}{J}\frac{\partial}{\partial \xi_k}\left\{J\rho\left(\vec{V}\cdot\vec{\varepsilon}^{k}\right)\phi\right\}=\frac{1}{J}\frac{\partial}{\partial \xi_k}\left[\Gamma J g^{jk}\frac{\partial\phi}{\partial \xi_j}\right]+S_\phi\right]\cdot J\,d\xi\,d\eta\,d\zeta \tag{38}$$

In the next several sections, individual terms of the above integration will be discussed.

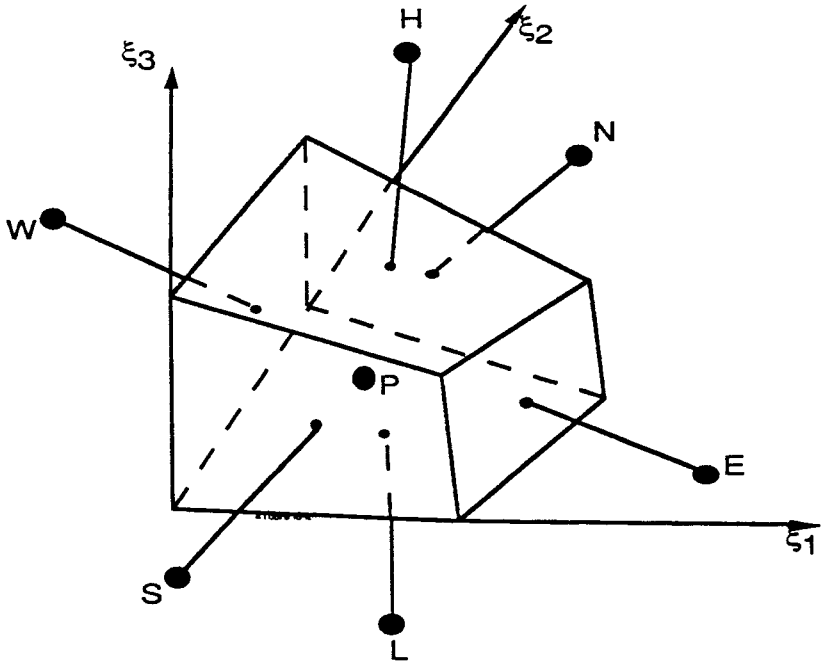


Figure 7. The Labeling Scheme of a Control Volume

### 3.3.3 Transient Term

Consider the discretization of the transient term of Equation (36), *i.e.*,

$$T = \iiint_{\forall} \frac{1}{J} \frac{\partial}{\partial t} (J \rho \phi) \cdot J \, d\xi \, d\eta \, d\zeta = \frac{\partial}{\partial t} \iiint_{\forall} (J \rho \phi) \, d\xi \, d\eta \, d\zeta = \frac{\rho \phi \forall - \rho^o \phi^o \forall^o}{\Delta t} \qquad (39)$$

In the above, superscript "*o*" stands for a value at an old time, variables without "*o*" superscript are at the new time, and $\forall$ stands for the volume. Note that the above discretization holds true for both Euler first-order and Crank-Nicholson second-order schemes.

### 3.3.4 Convection Term and Different Convection Schemes

By defining a physical contravariant velocity component $U^k$ such that $\vec{V} = U^k \vec{e}_k$, the convection term can be rewritten as

$$C = \frac{1}{J} \frac{\partial}{\partial \xi_k} [J \rho (\vec{V} \cdot \vec{\varepsilon}_k) \phi] = \frac{1}{J} \frac{\partial}{\partial \xi} \left[ \frac{J}{h_1} \rho U^1 \phi \right] + \frac{1}{J} \frac{\partial}{\partial \eta} \left[ \frac{J}{h_2} \rho U^2 \phi \right] + \frac{1}{J} \frac{\partial}{\partial \zeta} \left[ \frac{J}{h_3} \rho U^3 \phi \right] \qquad (40)$$

Integration of the above term over a control volume gives

$$C = C_e - C_w + C_n - C_s + C_h - C_l = G_e \phi_e - G_w \phi_w + G_n \phi_n - G_s \phi_s + G_h \phi_h - G_l \phi_l \qquad (41)$$

with $G_e$ defined, for example, as

$$G_e = \left( \frac{J}{h_1} \rho \, U^1 \right)_e \qquad (42)$$

where *G*'s represent the mass flux through a face of the control volume. The upper-case subscripts, W, E, S, N, L and H are used in this report to denote the neighboring cell-centers on the west, east, south, north, low, and high sides of the control volume shown in Figure 8. The lower-case subscripts *w*, *e*, *s*, *n*, *l*, and h, are used to represent the corresponding cell faces of the control volume. The evaluation of the mass fluxes, *G*, will be described in Section 3.4 while the evaluation of $\phi$ at control volume faces is described next.

For ease of illustration, consider the 2D control volume as shown in Figure 8 Because the flow variable $\phi$ is available only at the cell-centers, the cell-face values of $\phi$ need to be interpolated. Various interpolation schemes with varying levels of numerical accuracy and stability are in use today. In SCISEAL the user has a choice of several popular schemes, each of which is illustrated below in the evaluation of $\phi_e$, the value at the east cell face.

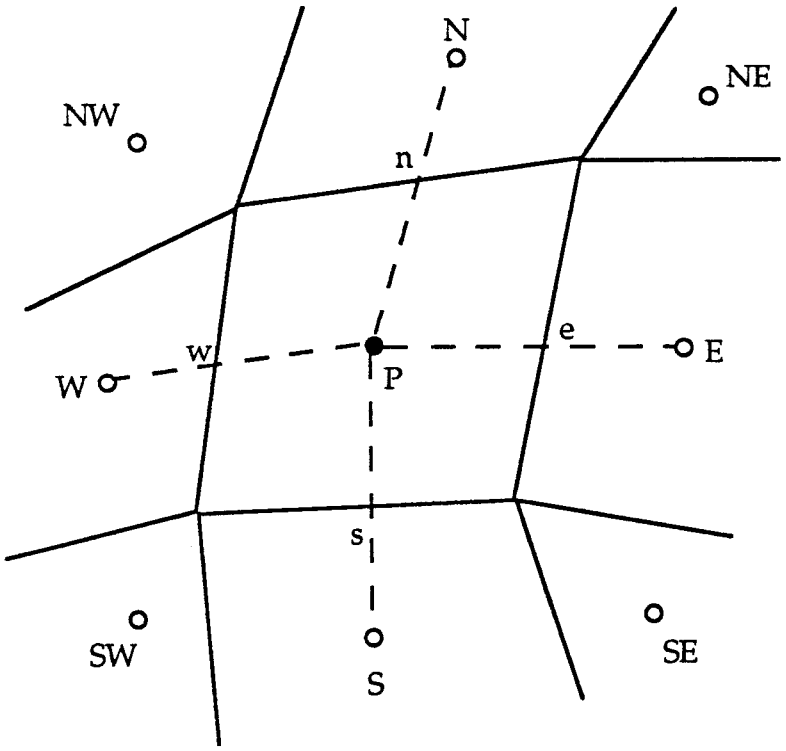


Figure 8. A 2D Stencil for the Discretization of Convection and Diffusion Terms

**3.3.4.1 First Order Upwind Scheme** First order upwind approach will evaluate $\phi_e$ using either $\phi_P$ or $\phi_E$ depending on the flow direction at point $e$. Mathematically it can be expressed as

$$C_e^{UP} = \begin{cases} G_e\phi_p & \text{if } G_e > 0 \\ G_e\phi_E & \text{if } G_e < 0 \end{cases} \tag{43}$$

or in more convenient form as

$$C_e^{UP} = G_e \frac{\phi_E + \phi_p}{2} - |G_e| \frac{\phi_E - \phi_p}{2} \tag{44}$$

This scheme has first-order accuracy and is one of the most stable schemes.

**3.3.4.2 Central Difference Scheme** Pure central difference approach will evaluate $\phi_e$ by averaging the values at point $P$ and $E$. That is

$$C_e^{CN} = G_e \frac{\phi_E + \phi_p}{2} \tag{45}$$

It is widely known that pure central difference scheme may cause unphysical oscillations. For most problems, some damping (or artificial viscosity) is needed for stability. In practice, central difference scheme with damping is constructed as

$$C_e = d_e C_e^{UP} + (1 - d_e) C_e^{CN} \tag{46}$$

with $d_e$, the damping coefficient, representing the fraction of upwind scheme used.

Equation (46) can be re-written as

$$C_e = G_e \frac{\phi_p + \phi_E}{2} - d_e |G_e| \frac{\phi_E - \phi_p}{2} \tag{47}$$

Comparing Equation (47) with Equations (45) and (44), it is clear why the scheme is called central differencing plus damping. $d_e = 0$ yields the pure central scheme, while $d_e = 1.0$ results in the upwind scheme. In this report, central difference scheme often refers to pure central plus the damping term as given above.

**3.3.4.3 Second Order Upwind Scheme** In this scheme, the cell face value is evaluated using two upstream nodes. The cell convective flux is given by

$$C_e = \begin{cases} G_e\left(\frac{3}{2}\phi_P - \frac{1}{2}\phi_W\right) & \text{if } G_e > 0 \\ G_e\left(\frac{3}{2}\phi_E - \frac{1}{2}\phi_{EE}\right) & \text{if } G_e < 0 \end{cases} \tag{48}$$

**3.3.4.4 Smart Scheme with Minmod Limiter** For the central differencing scheme, the damping coefficient is constant for the entire domain. There are many flow situations where damping is needed only in certain limited regions. Therefore, smart scheme is designed to adaptively calculate damping coefficient depending on the local flow property. The minmod limiter can be used to obtain damping coefficient, $d_e$ as:

$$d_e = minimode\left(1, \gamma_e\right) \tag{49}$$

with

$$\gamma_e = \frac{\phi_{E-U} - \phi_{p-U}}{\phi_E - \phi_p} \text{ and } U = sign\left(G_e\right) \tag{50}$$

The MINMOD function is defined as

$$MINMOD\left(\alpha, \beta\right) = sign\left(\alpha\right) max\left[o, min\left(|\alpha|, \beta\right)\right]$$

This scheme will reduce to upwind scheme if there exists local extreme such as across shocks ($\gamma_e < 0$), to central difference scheme when $\gamma_e \geq 1$ , and second order upwind scheme for $0 < \gamma_e < 1$.

**3.3.4.5 Other High-Order Schemes** For compressible flows with shocks, several high-order schemes with limiters are very accurate for shock capturing. Three such schemes are introduced in the following.

Osher-Chakravarthy Scheme: Osher-Chakravarthy scheme evaluates the damping coefficient as

$$d_e = \frac{1-\eta}{2} minmod(\beta, \gamma_e) + \frac{1+\eta}{2} minmod\left(1, \beta\gamma_e\right) \tag{51}$$

with $\eta = \frac{1}{3}$ and $\beta = \frac{3 - \eta}{1 - \eta}$

Roe's Superbee Scheme: Roe's Superbee scheme is used to obtain the damping coefficient as

$$d_e = Max\,[o,\ min\,(2\gamma, 1),\ min\,(\gamma, 2)] \tag{52}$$

van Leer's MUSCL Scheme: van Leer's MUSCL scheme is used to obtain the damping coefficient as

$$d_e = \frac{|\gamma_e| + \gamma_e}{(1 + \gamma_e)} \tag{53}$$

### 3.3.5 Diffusion Terms

The diffusion term in Equation (36) can be split into two parts: main diffusion (j = k); and cross diffusion (j ≠ k). Let's consider main diffusion first, *i.e.*

$$D_M^k = \frac{1}{J}\frac{\partial}{\partial \xi_k}\left[\Gamma J g^{kk}\frac{\partial \phi}{\partial \xi_k}\right], \quad k = 1, 2, or\ 3 \tag{54}$$

Without loss of generality, $k = 1$ term will be used for derivation. Integration of $D_M^1$ term over a control volume, as shown in Figure 7, leads to

$$\iiint D_M^1 J\, d\xi d\eta d\zeta = \left[\Gamma J g^{11}\frac{\partial \phi}{\partial \xi}\right]_e - \left[\Gamma J g^{11}\frac{\partial \phi}{\partial \xi}\right]_w \tag{55}$$

It is easy to show that

$$Jg^{11} = \frac{A^2}{J} = \frac{A}{h_1 \sin\ \alpha_1} \tag{56}$$

where $A$ is the area of the control volume face along the $\xi$ direction and $\alpha_1$ represents the angle between vector $\vec{e}_1$ and the plane formed by $\vec{e}_2$ and $\vec{e}_3$. By defining

$$D^{\xi} = \frac{\Gamma \cdot A^1}{h_1 \sin \alpha_1} \tag{57}$$

we have

$$\iiint D_M^1 J \, d\xi \, d\eta \, d\zeta = D_e^{\xi}(\phi_E - \phi_P) - D_w^{\xi}(\phi_P - \phi_W) = -\left(D_e^{\xi} + D_w^{\xi}\right)\phi_P + D_e^{\xi}\phi_E + D_w^{\xi}\phi_W \tag{58}$$

Therefore, $D\ \xi$, the main diffusion coefficient needs to be evaluated at the faces of each control volume.

The cross diffusion term is written as

$$D_c^{jk} = \frac{1}{J}\frac{\partial}{\partial \xi_k}\left[J \Gamma g^{jk} \frac{\partial \phi}{\partial \xi_j}\right], \quad j \neq k \tag{59}$$

Consider $D_c^{21}$ for illustration purposes

$$\iiint D_c^{21} J \, d\xi d\eta d\zeta = \left(\Gamma J g^{21} \frac{\partial \phi}{\partial \eta}\right)_e - \left(\Gamma J g^{21} \frac{\partial \phi}{\delta \eta}\right)_w \tag{60}$$

By defining $D^{21} = \frac{\Gamma}{4} J g^{21}$ and assuming $\phi_{ne} = \frac{1}{4}(\phi_P + \phi_E + \phi_N + \phi_{NE})$, *etc.*, we have

$$\iiint D_c^{21} J \, d\xi d\eta d\zeta = D_e^{21}(\phi_N + \phi_{NE} - \phi_S - \phi_{SE}) - D_w^{21}(\phi_N + \phi_{NW} - \phi_S - \phi_{SW}) \tag{61}$$

Other cross terms can be similarly discretized.

### 3.3.6 Source Term

If the source term is a function of $\phi$ itself, it is linearized as

$$S_\phi = S^P \phi + S^U \tag{62}$$

such that $S^P$ is negative. In general, both $S^P$ and $S^U$ can be functions of $\phi$. They are evaluated using the latest available value of $\phi$, which is generally taken to be the value of $\phi$ at the end of previous iteration. The linearized source term is integrated over the control volume which results in

$$S = S_P \phi_p + S_U \tag{63}$$

where the coefficients $S_P$ and $S_U$ are given as follows

$$S_p = \forall S^P \tag{64a}$$

$$S_U = \forall S^U \tag{64b}$$

### 3.3.7 Finite Difference Equation

In Sections 3.3.3 to 3.3.5, the general convection-diffusion Equation (36) has been discretized term by term over a control volume. If the numerically integrated transient, convection, diffusion and source terms are assembled together, it results in the following linear equation.

$$\begin{aligned} a_P\phi_P = {} & a_W\phi_W + a_E\phi_E + a_S\phi_S + a_N\phi_N + a_L\phi_L + a_H\phi_H \\ & + a_{SW}\phi_{SW} + a_{SE}\phi_{SE} + a_{NW}\phi_{NW} + a_{NE}\phi_{NE} \\ & + a_{LS}\phi_{LS} + a_{LN}\phi_{LN} + a_{HS}\phi_{HS} + a_{HN}\phi_{HN} \\ & + a_{WL}\phi_{WL} + a_{WH}\phi_{WH} + a_{EL}\phi_{EL} + a_{EH}\phi_{EH} \\ & + S_U \end{aligned} \tag{65}$$

The coefficients $a_P$, $a_W$, *etc.* are known as link coefficients, and the Equation (65) is known as a finite difference equation (FDE). This equation is the discrete equivalent of the continuous flow transport equation we started with. To summarize, the PDE represented by Equation (36), when numerically integrated using the finite-volume methodology, results in the FDE given by Equation (65).

This FDE, in general, is nonlinear because the link coefficients themselves are functions of $\phi_P$, $\phi_W$, *etc.* When an FDE is formulated for each computational cell, it results in a set of coupled nonlinear algebraic equations. No direct matrix inversion method is available to solve a set of nonlinear algebraic equations. Therefore an iterative procedure is employed in SCISEAL at every time step. A linear FDE is formed by evaluating the link coefficients with the values of $\phi$ available at the end of previous iteration.

$$a_P^k \phi_P^{k+1} = \Sigma a_{nb}^k \phi_{nb}^{k+1} + S_U^k \tag{66}$$

Here, the compact notations $a_{nb}$ and $\phi_{nb}$ are used to represent the link coefficients and the values of flow variable corresponding to the neighboring grid points. The subscripts $k$ and $k+1$ denote the previous and current iteration numbers respectively. When the linear set (66) is solved, we have an improved estimate for $\phi$. This improved estimate is used to update the link coefficients $a_P$, $a_{nb}$ and $S_U$ and the linear set is solved again. The iterative procedure is repeated until a converged solution is obtained.

### 3.3.8 Pressure Gradient Term

The pressure and velocity fields are strongly coupled in fluid flows. For this and other reasons that will become obvious to the user in the next chapter, the pressure gradient term appearing in the momentum equations is treated differently from other source terms.

Let us consider the pressure gradient term of the x-momentum equation. In a BFC system, it is represented as

$$\frac{\partial p}{\partial x} = \frac{\partial p}{\partial \xi}\xi_x + \frac{\partial p}{\partial \eta}\eta_x + \frac{\partial p}{\partial \zeta}\zeta_x \tag{67}$$

where $\xi_x$, $\eta_x$ and $\zeta_x$ are given by

$$\begin{aligned} \xi_x &= \varepsilon^1 \cdot i \\ \eta_x &= \varepsilon^2 \cdot i \\ \zeta_x &= \varepsilon^3 \cdot i \end{aligned} \tag{68}$$

Equation (67) may be represented in a compact form as shown below.

$$\frac{\partial p}{\partial x} = \frac{\partial p}{\partial \xi_k}\left(\varepsilon^k \cdot i\right) \tag{69}$$

When $\partial p/\partial x$ is integrated over the control volume shown in Figure 7, it results in the following

$$\iiint_v \frac{\partial p}{\partial x} \cdot J \, d\xi \, d\eta \, d\zeta = \iiint_v \frac{\partial p}{\partial \xi_k}\left(\varepsilon^k \cdot i\right) d\xi \, d\eta \, d\zeta$$

$$= A^{1x} \nabla_\xi p + A^{2x} \nabla_\eta p + A^{3x} \nabla_\zeta p \tag{70}$$

where, $A^{1x}$, $A^{2x}$ and $A^{3x}$ represent projected areas of control volume faces, *e. g.*, $A^{1x}$ is the area of $\eta-\zeta$ face of the control volume projected normal to the $x$-direction. $\nabla_\xi p$, $\nabla_\eta p$ and $\nabla_\zeta p$ represent pressure differences which, when evaluated at the cell center, are given by

$$\begin{aligned} \nabla_\xi p &= p_e - p_w \\ \nabla_\eta p &= p_n - p_s \\ \nabla_\zeta p &= p_h - p_\ell \end{aligned} \tag{71}$$

where $p_e$, $p_s$ *etc.* are cell-face pressures that need to be interpolated from neighboring nodal pressures. Equation (70) may be rewritten in the following compact form

$$\forall \left(\frac{\delta p}{\delta x}\right)_p = A^{kx} \nabla_k \, p \tag{72}$$

Here, $\delta p/\delta x$ is the discrete equivalent of the continuous pressure gradient $\partial p/\partial x$. Similar expressions can be obtained for $\partial p/\partial y$ and $\partial p/\partial z$.

## 3.4 Discretization of Mass Conservation and Mass Flux Evaluation

As mentioned before, mass conservation equation is a special one which can not be written as the general convection-diffusion form (Equation (36)). Moreover, in a pressure-based method mass conservation is used to determine pressure field. For this purpose, the mass conservation equation needs special attention. The general mass conservation equation can be transformed into BFC coordinates as

$$\frac{1}{J}\frac{\partial J\rho}{\partial t}+\frac{1}{J}\frac{\partial}{\partial \xi_k}\left(J\,\rho\,\vec{V}\cdot\vec{\varepsilon}^k\right)=0 \tag{73}$$

Therefore, integration over a control volume yields

$$\frac{\rho\forall-\rho^o\forall^o}{\Delta t}+G_e-G_w+G_n-G_s+G_h-G_l=0 \tag{74}$$

With $G_e=\left(\frac{J}{h_1}\rho\,U^1\right)_e$ for example. Note that $G$'s are the mass flux through a control volume face as mentioned in Section 3.3.4.

The next task is to evaluate mass fluxes $G$'s at control volume faces such that the checkerboard instability is eliminated for a Colocated variable arrangement. This is achieved by averaging momentum equation to the cell faces and relating the cell face velocity directly to the local pressure gradient. A brief description of the procedure is outlined below.

The discretized x-momentum equation can be expressed at a cell center P as (see Figure 7)

$$\left[a_p^u+\left(\frac{\rho\forall}{\Delta t}\right)_p\right]u_p=\sum_{nb}a_{nb}^u\,u_{nb}-\forall_p\left(\frac{\partial p}{\partial x}\right)_p+\left(\frac{\rho\forall}{\Delta t}\right)_p u_p^o+S_u^u \tag{75}$$

where $nb$ refers to all the neighboring cells and the transient term is explicitly expressed to ensure that the momentum equation at cell face includes the effect of a time step. Dividing the above equations by $a_p^u$ yields

$$\left(1 + cd_p^u\right) u_p = \sum_{nb} \frac{a_{nb}^u}{a_p^u} u_{nb} - d_p^u \left(\frac{\partial p}{\partial x}\right)_p + cd_p^u u_p^o + \frac{S_u^u}{a_p^u} \tag{76}$$

where

$$c = \frac{\rho}{\Delta t} \quad , \quad d_p^u = \frac{\forall}{a_p^u} \tag{77}$$

The above momentum equation is at P-cell but in reality it applies to every point. Therefore, at cell face $f$, for example, we have

$$\left(1 + cd_f^u\right) u_f = \left(\sum_{nb} \frac{a_{nb}^u}{a_p^u} u_{nb}\right)_f - d_f^u \left(\frac{\partial p}{\partial x}\right)_f + cd_f^u u_f^o + \left(\frac{S_u^u}{a_p^u}\right)_f \tag{78}$$

Since we do not know how to evaluate $(a_{nb}^u)_f$, for example, the following quantities at $f$ will be obtained by averaging the same quantity from two neighboring cell center points.

$$d_f^u, \quad \left(\sum_{nb} \frac{a_{nb}^u}{a_p^u} u_{nb}\right)_f, \quad \left(\frac{S_u^u}{a_p^u}\right)_f \tag{79}$$

Therefore, by using Equation (76) we have

$$\left[\sum_{nb} \frac{a_{nb}^u}{a_p^u} u_{nb} + \frac{S_u^u}{a_p^u}\right]_f = \overline{\left(\sum_{nb} \frac{a_{nb}^u}{a_p^u} u_{nb} + \frac{S_u^u}{a_p^u}\right)} = \overline{\left(\left(1 + cd_p^u\right) u_p + d_p^u \left(\frac{\partial p}{\partial x}\right)_p - cd_p^u u_p^o\right)} \tag{80}$$

where overbar means average from points $P$ and $E$. A second-order accurate linear interpolation procedure is used in SCISEAL to get the various averaged quantities at cell face $f$. Equation (78) can be written as:

$$\left(1 + cd_f^u\right) u_f = \overline{\left(1 + cd_p^u\right) u_p + d_p^u \left(\frac{\partial p}{\partial x}\right)_p - cd_p^u u_p^o} - \overline{d_p^u} \left(\frac{\partial p}{\partial x}\right)_f + cd_f^u u_f^o \tag{81}$$

and the above equation is further reduced to

$$u_f = \overline{u_p} + d^u \left[ \overline{\left(\frac{\partial p}{\partial x}\right)_p} - \left(\frac{\partial p}{\partial x}\right)_f \right] + cd^u \left(u_f^o - \overline{u_p^o}\right) \tag{82}$$

with

$$d^u = \frac{\overline{d_p^u}}{1 - c\overline{d_p^u}} \tag{83}$$

Now it is clear from the above equations that the cell face velocity is obtained from an average of the two neighboring point velocity plus a second-order pressure correction and a second-order previous time velocity correction. The pressure term serves as the mechanism to avoid the checkerboard problem and the previous time velocity serves as a mechanism to obtain a time-independent steady solution.

The y-component and z-component velocities can be similarly evaluated and the contravariant velocity component at the cell face can be thus evaluated as

$$U_f^1 = u_f \cdot F_{1x} + v_f \cdot F_{1y} + w_f \cdot F_{1z} \tag{84}$$

with

$$F_{1x} = h_1 \vec{\varepsilon^1} \cdot \vec{i} \; ; \; F_{1y} = h_1 \vec{\varepsilon^1} \cdot \vec{j} \; ; \; F_{1z} = h_1 \vec{\varepsilon^1} \cdot \vec{k} \tag{85}$$

and the grid metrics, $F_{1x}$ *etc.* are evaluated at the cell face.

### 3.5 Pressure-Correction Equation

As outlined earlier, each flow variable is governed by a partial differential equation (PDE) which is numerically solved to obtain a discrete solution for that variable. The three momentum equations yield the three cartesian components of velocity. Even though pressure is an important flow variable, no governing PDE for pressure is presented. Pressure-based methods utilize the continuity equation to formulate an equation for pressure. Two methods to achieve the velocity-pressure coupling are available in SCISEAL:

- SIMPLEC
- PISO

The basic framework of each method is briefly described below.

### 3.5.1 SIMPLEC Algorithm

SIMPLEC stands for "Semi-Implicit Method for Pressure-Linked Equations Consistent", and is an enhancement to the well known SIMPLE algorithm[8]. In SIMPLEC, which was originally proposed by Van Doormal and Raithby[9], an equation for pressure-correction is derived from the continuity equation.

The finite-difference form of the $x$-momentum equation can be written as

$$a_P u_P = \left\{\Sigma a_{nb} u_{nb} + S_u\right\}_P - A_P^{kx} \nabla_k p_P \tag{86}$$

where the subscript $P$ refers to cell center $P$. The pressure field should be provided to solve Equation (86) for $u$. However, the pressure field is not known *a priori*. If the preceding equation is solved with a guessed pressure (or the latest available pressure in an iterative procedure) $p^*$, it will yield velocity $u^*$ which satisfies the following equation.

$$a_P u_P^* = \left\{\Sigma a_{nb} u_{nb}^* + S_u\right\}_P - A_P^{kx} \nabla_k p_P^* \tag{87}$$

In general, $u^*$ will not satisfy continuity. The strategy is to find corrections to $u^*$ and $p^*$ so that an improved solution can be obtained. Let $u'$ and $p'$ stand for the corrections.

$$u = u^* + u' \tag{88}$$

$$p = p^* + p' \tag{89}$$

An expression for $u_P'$ can be obtained by subtracting Equation (87) from (86).

$$a_P u_P' = \left\{\Sigma a_{nb} u_{nb}'\right\}_P - A_P^{kx} \nabla_k p_P' \tag{90}$$

Because our aim is to find an incrementally better solution, we will approximate $u'_{nb}$ by $u'_P$ giving us an expression for $u'_P$

$$u'_P = d_P^k \nabla_k p'_P \tag{91}$$

where

$$d_P^k = \frac{A_P^{kx}}{a_P - \Sigma a_{nb}} \tag{92}$$

We can also obtain an expression for $u'_e$, the velocity correction at the east cell face, by averaging from the nodal corrections

$$u'_e = -\left(\overline{d_P^k + d_E^k}\right)\nabla_k p'_e \tag{93}$$

and the gradient of the pressure correction is evaluated at the cell face $e$.

The discretized continuity equation is

$$\frac{\rho_P \forall_P - \rho_P^\circ \forall_P^\circ}{\Delta t} + G_e - G_w + G_n - G_s + G_h - G_\ell = 0 \tag{94}$$

The convective fluxes $G_e$ *etc.* can be represented as

$$G = G^* + G' \tag{95}$$

Where $G^*$ represent the fluxes calculated using $u^*$, $P^*$ *etc.*, and $G'$ is the correction to the fluxes, and is to be evaluated.

Substituting in Equation (94) and rearranging, the discretized continuity equation is

$$\frac{\rho'_P \forall_P}{\Delta t} + G'_e - G'_w + G'_n - G'_s + G'_h - G'_\ell = S_m \tag{96}$$

Where $S_m$ represents the mass correction or mass source in the control volume

$$S_m = -\left[\frac{\rho_P^{\circ} \forall_P^{\circ} - \rho_P^{*} \forall_P}{\Delta t} + G_e^{*} - G_w^{*} + G_n^{*} - G_s^{*} + G_h^{*} - G_\ell^{*}\right] \tag{97}$$

By using Equation (42) in Equation (95) we get an expression for $G_e^{'}$

$$G_e^{'} = \left(\frac{J}{h_1}\rho^{*} U^{1'}\right)_e + \left(\frac{J}{h_1}\rho^{'} U^{1*}\right)_e \tag{98}$$

In the derivation of the preceding equations, products of primes have been neglected.

For incompressible flows $\rho'$ is zero. For compressible flows $\rho'$ is estimated as

$$\rho^{'} = \left(\frac{\partial \rho}{\partial p}\right)^{*} p^{'} \tag{99}$$

An equation of state is used to estimate $\partial\rho/\partial p$. If the fluid is a perfect gas

$$\frac{\partial \rho}{\partial p} = \frac{1}{RT} \tag{100}$$

The density correction at the east cell face $\rho'$, is estimated from $\rho_P^{'}$ and $\rho_E^{'}$ using the same scheme used to estimate $\rho_e$. $U_e^{1'}$ is obtained from the cartesian velocity corrections,

$$U_e^{1'} = u_e^{'} F_{1x} + v_e^{'} F_{1y} + w_e^{'} F_{1z} \tag{101}$$

where $F_{1x}$, *etc.* are the grid metrics at cell face $e$. Equation (93) is used to obtain $u_e^{'}$ and $v_e^{'}$ and $w_e^{'}$ are obtained similarly starting with $y$- and $z$-momentum equations following the procedure outlined in this section.

Expressions for the contravariant velocity corrections and fluid density corrections at all the cell faces are obtained and substituted in Equation (96) yielding an FDE for the pressure correction

$$a_P p_P' = a_W p_W' + a_E p_E' + a_S p_S' + a_N p_N' + a_L p_L' + a_H p_H' + S_m \qquad (102)$$

The SIMPLEC procedure can be summarized as follows:

1. Guess a pressure field $p^*$.

2. Obtain $u^*$, $v^*$, and $w^*$ by solving discretized momentum equations such as Equation (87).

3. Evaluate $G^*$ from $\rho^*$, $u^*$, *etc.* using the procedure outlined in Section 3.4.

4. Evaluate mass source from Equation (97).

5. Obtain $p'$ by solving Equation (102).

6. Use $p'$ to correct the pressure and velocity fields using Equations (88) and (89).

7. Solve the discretized equations for other flow variables including turbulence quantities.

8. Go to step 2 and repeat the procedure until convergence is obtained.

A variation of the procedure outlined above is employed in SCISEAL. After Step 6, instead of executing Step 7, Steps 3, 4, 5, and 6 can be repeated a few times. That is, only the pressure-correction equation is solved a few more times and the pressure, velocity and density fields are updated. These intermediate iterations are called the 'continuity or pressure-correction iterations'. They are found to enhance overall convergence for flow of compressible fluids.

### 3.5.2 PISO Algorithm

PISO stands for Pressure-Implicit with Splitting of Operators. PISO employs a non-iterative time marching method to handle the velocity-pressure coupling. It is essentially a predictor-corrector method in which the velocity, pressure and density

fields from the previous time level are incrementally corrected to obtain the flow field at a new time level. PISO was developed by Issa[10].

In order to explain the framework of PISO, it is convenient to recast the discretized continuity equation in the following form

$$\frac{\rho \forall - \rho^{\circ} \forall^{\circ}}{\Delta t} + \forall \Delta_i (\rho u_i) = 0 \tag{103}$$

where $\Delta_i$ is the finite difference equivalent of the divergence operator and subscript "i" indicates cartesian $x$, $y$, and $z$ directions. Equation (103) can be rewritten as

$$\Delta_i (\rho u_i) = -\frac{\rho - \rho^{\circ}}{\Delta t} - \frac{\rho^{\circ}}{\Delta t}\left(1 - \frac{\forall^{\circ}}{\forall}\right) \tag{104}$$

The discretized momentum equations are represented as

$$\frac{\rho u_i \forall - \rho^{\circ} u_i^{\circ} \forall^{\circ}}{\Delta t} + a_P u_i = \Sigma a_{nb} u_{i,nb} - \forall \Delta_i p + S_U \tag{105}$$

With some rearrangement of terms, the preceding equation can be written as

$$\left(\frac{\forall}{\Delta t} + \frac{a_P}{\rho}\right) \rho u_i = \Sigma a_{nb} u_{i,nb} - \forall \Delta_i p + S_U + \frac{\rho^{\circ} u_i^{\circ} \forall^{\circ}}{\Delta t} \tag{106}$$

Note that both the continuity and momentum equations are numerically integrated over the control volume with $P$ as its center. The subscript $P$ on $\rho$, $p$, $u_i$ and $\forall$ is omitted for convenience.

Let us represent the dependence of $\rho$ on $p$ as

$$\rho = p f(p, T) \tag{107}$$

For an incompressible fluid, $f = 0$. For a perfect gas,

$$f(p, T) = \frac{1}{RT} \tag{108}$$

PISO algorithm with one predictor and two corrector steps is illustrated below. In principle, there is no limit on the number of corrector steps.

(a) Momentum Predictor: Equation (106) is implicitly solved using the density and pressure from the previous time step.

$$\left(\frac{\forall}{\Delta t}+\frac{a_p}{\rho^\circ}\right)\rho^\circ u_i^* = \Sigma a_{nb}u_{i,nb}^* - \forall \Delta_i p^\circ + S_U + \frac{\rho^\circ u_i^\circ \forall^\circ}{\Delta t} \tag{109}$$

The resulting solution, $u_i^*$, in general, will not satisfy continuity.

(b) First Momentum Corrector: The momentum equation is written in an explicit corrector form as follows

$$\left(\frac{\forall}{\Delta t}+\frac{a_p}{\rho^\circ}\right)\rho^* u_i^{**} = \Sigma a_{nb}u_{i,nb}^* - \forall \Delta_i p^* + S_U + \frac{\rho^\circ u_i^\circ \forall^\circ}{\Delta t} \tag{110}$$

The momentum equation can be recast in delta form by subtracting Equation (109) from (110).

$$\rho^* u_i^{**} - \rho^\circ u_i^* = -\left(\frac{\forall}{\Delta t}+\frac{a_p}{\rho^\circ}\right)^{-1} \forall \Delta_i (p^* - p^\circ) \tag{111}$$

However, we cannot solve for $u_i^{**}$ because $p^*$, and consequently $\rho^*$ are unknown. To find $p^*$, we will enforce that $u_i^{**}$ and $\rho^*$ satisfy continuity. That is

$$\Delta_i\left(\rho^* u_i^{**}\right) = -\frac{\rho^* - \rho^\circ}{\Delta t} - \frac{\rho^\circ}{\Delta t}\left(1 - \frac{\forall^\circ}{\forall}\right) \tag{112}$$

Taking a discrete divergence of Equation (111) and utilizing Equation (112), we get

$$\Delta_i\left\{\left(\frac{\forall}{\Delta t}+\frac{a_p}{\rho^\circ}\right)^{-1} \forall \Delta_i\right\}(p^* - p^\circ) = \Delta_i\left(\rho^\circ u_i^*\right) + \frac{\rho^* - \rho^\circ}{\Delta t} + \frac{\rho^\circ}{\Delta t}\left(1 - \frac{\forall^\circ}{\forall}\right) \tag{113}$$

Using the equation of state $\rho^*$ is evaluated as

$$\rho^* = p^* f\left(p^\circ, T^\circ\right) \tag{114}$$

substituting in Equation (113)

$$\left[\Delta_i \left\{\left(\frac{\forall}{\Delta t} + \frac{a_P}{\rho^\circ}\right)^{-1} \forall \Delta_i\right\} - \frac{f\left(p^\circ, T^\circ\right)}{\Delta t}\right]\left(p^* - p^\circ\right) = \Delta_i \left(\rho^\circ u_i^*\right) + \frac{\rho^\circ}{\Delta t}\left(1 - \frac{\forall^\circ}{\forall}\right) \tag{115}$$

Solution to the above yields $p^*$, which when substituted in Equation (111) yields the corrected velocity $u_i^{**}$.

(c) Enthalpy Predictor: The discretized enthalpy equation formulated with $\rho^*$, $p^*$ and $u_i^{**}$ is solved to yield $h^*$ or $H^*$. From the known enthalpy, $T^*$ is obtained from thermodynamic property tables.

(d) Second Momentum Corrector: The momentum equation is again represented in an explicit form

$$\left(\frac{\forall}{\Delta t} + \frac{a_P}{\rho^*}\right)\rho^{**} u_i^{***} = \Sigma a_{nb} u_{i,nb}^{**} - \forall \Delta_i p^{**} + S_U + \frac{\rho^\circ u_i^\circ \forall^\circ}{\Delta t} \tag{116}$$

Recasting it in delta form by subtracting (110) from (116),

$$\rho^{**} u_i^{***} - \rho^* u_i^{**} = \left(\frac{\forall}{\Delta t} + \frac{a_P}{\rho^*}\right)^{-1} \left\{\Sigma a_{nb}\left(u_{i,nb}^{**} - u_{i,nb}^*\right) - \forall \Delta_i \left(p^{**} - p^*\right) - a_P\left(\frac{\rho^* - \rho^\circ}{\rho^\circ}\right) u_i^{**}\right\} \tag{117}$$

Enforcing continuity,

$$\Delta_i \left(\rho^{**} u_i^{***}\right) = -\frac{\rho^{**} - \rho^\circ}{\Delta t} - \frac{\rho^\circ}{\Delta t}\left(1 - \frac{\forall_\circ}{\forall}\right) \tag{118}$$

Taking the discrete divergence of (117) and using (118) and the equation of state

$$\rho^{**} = p^{**} f\left(p^*, T^*\right) \tag{119}$$

we get the following equation for pressure correction

$$\left[\Delta_i\left\{\left(\frac{\forall}{\Delta t}+\frac{a_P}{\rho^*}\right)^{-1}\forall\Delta_i\right\}-\frac{f(p^*,T^*)}{\Delta t}\right](p^{**}-p^*)$$
$$=\Delta_i\left[\left(\frac{\forall}{\Delta t}+\frac{a_P}{\rho^*}\right)^{-1}\left\{\Sigma a_{nb}\left(u^{**}_{i,nb}-u^{*}_{i,nb}\right)-a_P\left(\frac{\rho^*-\rho^\circ}{\rho^\circ}\right)u_i^{**}\right\}\right]+\frac{p^*}{\Delta t}\left\{f(p^*,T^*)-f(p^\circ,T^\circ)\right\} \quad (120)$$

Solving the above yields $p^{**}$ which can be used to evaluate $\rho^{**}$ from (119) and $u^{***}$ from (117).

The quantities $u^{***}$, $p^{**}$, $\rho^{**}$ and $T^*$ are taken to be the flow variables at the new time level. Steps (a) through (d) are repeated to get the flow field for subsequent time steps.

## 3.6 Crank-Nicholson Algorithm

This algorithm is adopted for transient flow analysis and is formally second-order accurate in time. Using an appropriate weighting function, the algorithm can also be modified to give first-order accuracy in time. The second-order accuracy is achieved by evaluating all convective and diffusive fluxes as well as source terms at time level $(n+1/2)$ where $n$ in the old time level. The algorithm consists of the following steps:

a. Evaluate all flux and source terms at last time-step *i.e.* at time level $n$. These are stored till next time step.

b. Intermediate velocity field, $u^*$, $v^*$ are calculated using the momentum equations. The fluxes are calculated using the following expression

$$(f_C+f_D)=\alpha(f_C+f_D)^k+(1-\alpha)(f_C+f_D)^n$$

where the superscript $k$ denotes the iteration level. $\alpha$ is called the Crank-Nicholson parameter, and controls the time-implicitness and accuracy of the scheme. The method is second-order accurate for $\alpha=0.5$.

c. Pressure corrections are evaluated as in the SIMPLEC algorithms, with the mass source term evaluated as

$$m = \alpha m^k + (1-\alpha)m^n$$

The velocities and pressures are updated as in SIMPLEC.

d. Steps b-c are repeated for a time step till a suitable convergence criterion is satisfied. All the flow variables are updated and calculations started for the next time step.

By changing the value of the Crank-Nicholson parameter to 1.0, the method reduces to the Euler backward time-discretization which is 1st order accurate in time.

### 3.7 Moving Grid Algorithm

The moving grid algorithm is used to treat time-dependent flow problems with changing/deforming grids as a result of boundary deformation. the formulation in SCISEAL is based on an extension of the Space Conservation Law (SCL) described by Demirdzic and Peric[11] for 2-D problems. When the computational grid moves in time and space, the grid velocity, $V_g$, enters the flow equations and the relation between the grid velocity and the control volume is given as

$$\frac{d}{dt}\int_v d\forall = \int_s V_g \cdot dS \tag{121}$$

where $\forall$ is the volume of control volume and $S$ is its surface area. The continuity and the generalized transport equations for the problem are written in integral form as

$$\frac{d}{dt}\int_v \rho d\forall + \int_s \rho(V - V_g)\cdot ds = 0 \tag{122}$$

$$\frac{d}{dt}\int_{\forall}\rho\phi d\forall+\int_{s}\rho\,\phi(V-V_g)\cdot ds=\int_{s}q\cdot ds+\int_{\forall}S_\phi d\,\forall \tag{123}$$

where $\forall$ is an arbitrary moving control volume, $s$ is the surface of $\forall$ and $V$ is the absolute fluid velocity vector. In Equation (123), $\phi$ could be the velocity vector or any other scalar quantity. $q$ and $S_\phi$ are the diffusive flux and source term for the corresponding flow quantity. The grid velocity $Vg$ is an unknown, and the SCL is used to evaluate it as follows.

Applying the space conservation law, Equation (121), to a moving control volume and using parametric time discretization, one obtains

$$\frac{\forall-\forall^o}{\Delta t}=\sum_{face}\left[\theta\int_f V_g\cdot ds+(1-\theta)\int_f V_g^o\cdot ds^o\right] \tag{124}$$

where $\forall$ stands for volume of the control volume at a new time step and superscript $o$ stands for values at the old time step. Note that $\theta = 1.0$ is the standard Euler backward differencing and $\theta = 0.5$ is the Crank-Nicolson scheme and the value of $\theta$ should be the same as the one used for other conservation equations for consistency. For numerical purposes, it is convenient to define a volumetric grid flux at a control volume (or cell) face, $f$, as

$$\dot{\forall}_f=\int_f V_g\cdot ds \tag{125}$$

and therefore, the discretized SCL can be rewritten as

$$\frac{\forall-\forall^o}{\Delta t}=\sum_{face}\left\{\theta\dot{\forall}_f+(1-\theta)\,\dot{\forall}_f^o\right\} \tag{126}$$

If $\Delta\forall_f$ stands for the volume swept by the cell face $f$, during one time step, it yields from the basic geometric requirement that

$$\frac{\forall - \forall^o}{\Delta t} = \sum_f \Delta V_f \tag{127}$$

Hence, a natural way for calculating the volumetric grid flux is to let

$$\frac{\Delta \forall_f}{\Delta t} = \theta \dot{\forall}_f + (1 - \theta)\ \dot{\forall}_f^o \tag{128}$$

or

$$\dot{\forall}_f = \frac{\Delta \forall_f}{\theta \Delta t} + \left(1 - \frac{1}{\theta}\right) \dot{\forall}_f^o \tag{129}$$

The apparent mass flux due to grid motion is obtained as

$$G_f^g = \rho_f\ \dot{\forall}_f \tag{130}$$

which when subtracted from the cell face mass flux, $G_f$, results in the effective mass flux that should be used in the evaluation of convective fluxes. The evaluation of $G_f$ has been discussed in Section 3.4.

A close look at $\Delta \forall_f$ reveals that $\Delta \forall_f$ is simply the volume (but it could be positive or negative) and the conventional method of calculating the volume of a control volume is applicable also to $\Delta \forall_f$.

### 3.8 Domain Interface Treatment

The multi-domain approach involves division of the overall flow domain into several suitable subdomains or zones such that all the grid generation in each of the subdomains is easier. Proper exchange of information across the interfaces where the subdomains join is crucial for the success of the solution procedure. The non-linear flow equations require a fully implicit and conservative treatment of the interface data exchange for an efficient and robust solution methodology. At present the SCISEAL code interface treatment allows a one-to-one match between cells as

well as a multi-to-one match, the only restriction being that an integer number of cells on one side of the interface must connect to a single cell on the other side. This is done through a special scheme in which the cell arrangement at an interface can be represented by a standard stencil shown in Figure 9. The bigger cell is identified as the parent (or base) cell while cells (one or many) on the other side of the interface are identified as children (or secondary cells). Such an arrangement allows the treatment of all domain interfaces in a standard form. For ease of illustration, the interface treatment is explained for 2D in the following sections. Extension to 3D is fairly straightforward.

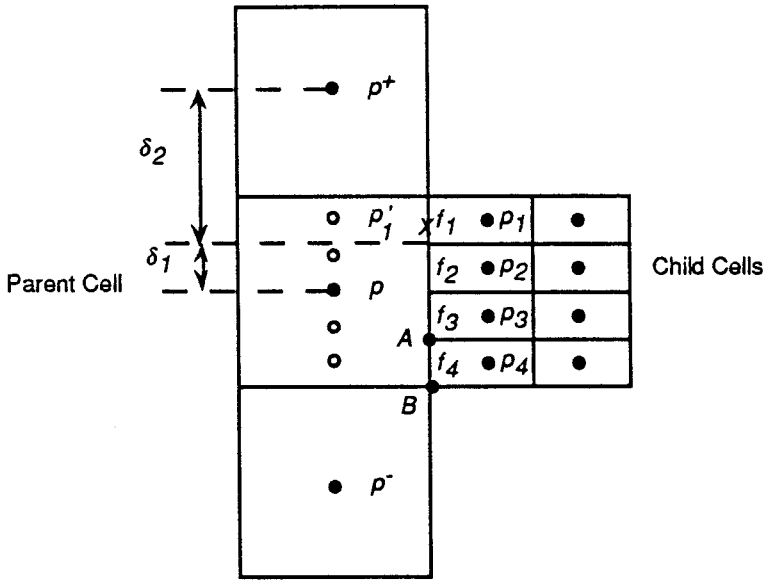


Figure 9. Basic Interface Treatment Stencil

### 3.8.1 Interface Interpolation

In order to discretize the convection terms of the generalized convection-diffusion equation, the flow variable $\phi$ needs to be interpolated at cell faces. Consider the cell face at the domain interface of Figure 9. To evaluate the interface value at point $f_1$ (denoted by x), for example, we need to identify a fictitious point $p_1'$ . If the $\phi$ value at $p_1'$ is obtained, the value at $f_1$ could be easily evaluated by any of the schemes described in Section 3.4. The $p_1'$ value could be obtained in the following three ways:

(a) Upwind Method:

$$\phi_{p_1}' = \phi_p \tag{131}$$

(b) Standard 2nd-Order:

$$\phi_{p_1}' = \frac{\delta_2}{\delta_1 + \delta_2}\phi_P + \frac{\delta_1}{\delta_1 + \delta_2}\phi_{P^*} \tag{132}$$

(c) Flux-Limited Scheme:

$$\begin{aligned} \phi_{p_1}' &= \phi_P + S_P\,\delta_1 + 0\left(\delta_1^2\right) \\ S_P &= S_{P-}\ Minimode\left(1, \frac{S_{P+}}{S_{P-}}\right) \\ S_{P-} &= \frac{\phi_P - \phi_{P-}}{\delta n} \\ S_{P+} &= \frac{\phi_{P+} - \phi_P}{\delta p} \end{aligned} \tag{133}$$

Scheme (b) is the default for all variables except convective fluxes; the scheme for convective fluxes depends on the selection by user.

### 3.8.2 Cross-Diffusion Term Treatment

Cross diffusion terms are important when severely skewed BFC grids are used. They can be the dominant terms in flows with little or no convection as in heat conduction problems. In SCISEAL, the cross diffusion terms at the domain interfaces are treated implicitly to ensure accuracy. This treatment is illustrated for one term below

$$D_c^{21} = \frac{1}{J}\frac{\partial}{\partial \xi}\left(J\Gamma g^{21}\frac{\partial \phi}{\partial \eta}\right) \tag{134}$$

Integration of this term for the child cells $p_1$, $p_2$, $p_3$ and $p_4$ is essentially the same as that for a single-domain grid. The values of $\phi$ at the child cell corners are evaluated from the surrounding nodal values, both physical and fictitious. For instance, $\phi_A$, the value of $\phi$ at the northwest corner of cell $p_4$, is estimated as

$$\phi_A = \frac{1}{4}\left(\phi_{P_3'} + \phi_{P_4'} + \phi_{P_3} + \phi_{P_4}\right) \tag{135}$$

Integration of Equation (134) for the parent cell $P$ requires special attention.

$$\iiint_P D_c^{21} J \; d\xi \, d\eta \, d\zeta = \left(J\Gamma g^{21}\frac{\partial\phi}{\partial\eta}\right)_e - \left(J\Gamma g^{21}\frac{\partial\phi}{\partial\eta}\right)_w \tag{136}$$

The second term on the right hand side of the preceding equation, *i.e.*, the west face term is evaluated as explained in Section 3.3.5. The first term on the right hand side is evaluated at each of the 4 segments that form the east face of cell $P$.

$$\left(J\Gamma g^{21}\frac{\partial\phi}{\partial\eta}\right)_e = \sum_{i=1}^{4}\left(J\Gamma g^{21}\frac{\partial\phi}{\partial\eta}\right)_{f_i} \tag{137}$$

For example, for the segment $f_4$, which is the interface between cell $P$ and cell $P_4$,

$$\left(J\Gamma g^{21}\frac{\partial\phi}{\partial\eta}\right)_{f_4} = \left(J\Gamma g^{21}\right)_{f_4}\left(\phi_A - \phi_B\right) \tag{138}$$

$\phi_A$ and $\phi_B$ are evaluated using relations such as Equation (135).

## 3.9 Conjugate Heat Transfer Analysis

In a number of seal and turbine secondary flow path problems the flow domain will contain internal solid objects, *e.g.* cavity wall, labyrinth seal teeth *etc*. Thermal energy transport can occur across the solid-fluid interfaces and through the solid objects. The energy equation solutions must consider convection-conduction in fluids, conduction in solids and the fluid-solid interface transfer. Such a procedure is called conjugate heat transfer (CHT) analysis.

### 3.9.1 Interface Constraints

For thermal energy conservation, the following criteria have to be met at a solid-fluid interface (see Figure 10):

- Heat flux at the interface must be equal both on solid and fluid sides; and
- Temperature has to be continuous across the interface.

These two conditions can be mathematically represented as

$$K_s(\nabla T)_s \cdot \boldsymbol{n} = K_f(\nabla T)_f \cdot \boldsymbol{n} \tag{139}$$

$$T_i = T_{si} = T_{fi} \tag{140}$$

where the subscripts $s$ and $f$ stand for solid and fluid respectively, and the subscript $i$ indicates the interface. Differences in the solid and fluid properties imply that quantities such as enthalpy will not be continuous across the interface.

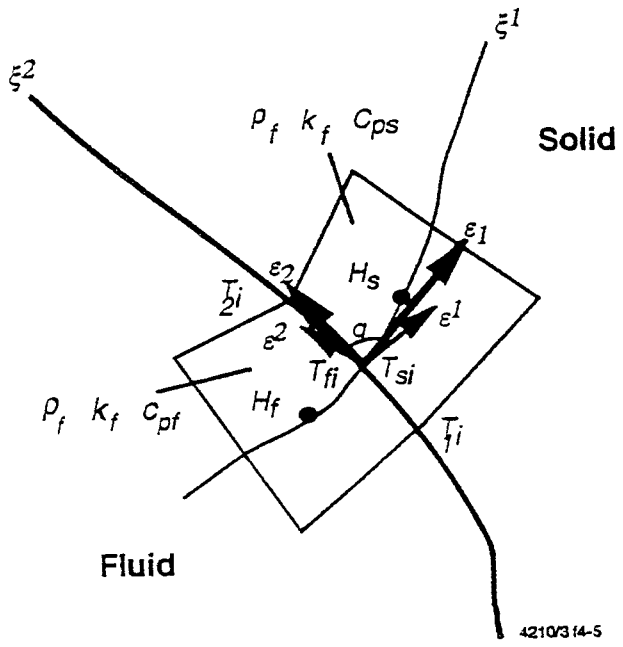


Figure 10. Interfacial Conditions for Conjugate Heat Transfer

### 3.9.2 Equivalent Thermal Conductivity

An equivalent thermal conductivity can be calculated using the interfacial balance equation. Equation (139) can be rewritten as

$$K_s \nabla T_s \cdot n = K_f \nabla T_f \cdot n = K_e \nabla T \cdot n \tag{141}$$

where $k_e$ is the equivalent thermal conductivity. In tensor notation, $\nabla T \cdot n$ is expressed as

$$\nabla T \cdot n = \left( \frac{\partial T}{\partial \xi} \cdot \frac{e^1}{e^1 \cdot e_1} + \frac{\partial T}{\partial \eta} \frac{e^2}{e^2 \cdot e_2} + \frac{\partial T}{\partial \zeta} \frac{e^3}{e^3 \cdot e_3} \right) \cdot n \tag{142}$$

where $e_1$, $e_2$, and $e_3$ are the covariant base vectors in $\xi$, $\eta$, and $\zeta$ directions, while $e^1$, $e^2$, and $e^3$ are the contravariant base vectors.

By assuming

$$\frac{\partial T_s}{\partial \xi} = \frac{T_s - T_i}{\Delta \xi_s}, \frac{\partial T_s}{\partial \eta} = \frac{T_{i1} - T_{i2}}{\Delta \eta_s}, \frac{\partial T_s}{\partial \zeta} = \frac{T_{i3} - T_{i4}}{\Delta \zeta_s}$$

in the solid phase, and

$$\frac{\partial T_f}{\partial \xi} = \frac{T_i - T_f}{\Delta \xi_f}, \frac{\partial T_f}{\partial \eta} = \frac{T_{i1} - T_{i2}}{\Delta \eta_f}, and \frac{\partial T_f}{\partial \zeta} = \frac{T_{i3} - T_{i4}}{\Delta \zeta_f}$$

in the liquid phase, the temperature at the interface $T_i$ can be obtained and expressed as follows

$$T_i = \frac{AT_f + BT_s + (D - C) + (F - E)}{A + B} \tag{143}$$

where

$$A = \frac{K_f}{\Delta\xi_f}\left(\frac{1}{e_1 \cdot n}\right)_f \qquad B = \frac{K_s}{\Delta\xi_s}\left(\frac{1}{e_1 \cdot n}\right)_s$$

$$C = \frac{K_f(T_{i1} - T_{i2})}{\Delta\eta}\left(\frac{e^2 \cdot n}{e^2 \cdot e_2}\right)_f \qquad D = \frac{K_s(T_{i1} - T_{i2})}{\Delta\eta}\left(\frac{e^2 \cdot n}{e^2 \cdot e_2}\right)_s$$

$$E = \frac{K_f(T_{i3} - T_{i4})}{\Delta\eta}\left(\frac{e^3 \cdot n}{e^3 \cdot e_3}\right)_f \qquad F = \frac{K_s(T_{i3} - T_{i4})}{\Delta\zeta}\left(\frac{e^3 \cdot n}{e^3 \cdot e_3}\right)_s$$

Note that $T_{i1}$, $T_{i2}$, $T_{i3}$ and $T_{i4}$ are the interfacial temperatures at the corners. By substituting Equation (142) into Equation (141), the equivalent thermal conductivity $K_e$ is obtained after some manipulation.

$$K_e = \frac{AB(T_s - T_f + A(D+F) + B(C+E))}{(A+B)[G \cdot (T_s - T_f + H + I)]} \tag{144}$$

where

$$G = \frac{1}{\Delta\xi_s + \Delta\xi_f}\left(\frac{1}{e_1 \cdot n}\right), H = \frac{T_{i1} - T_{i2}}{\Delta\eta}\left(\frac{e^2 \cdot n}{e^2 \cdot e_2}\right), \text{and } I = \frac{T_{i3} - T_{i4}}{\Delta\zeta}\left(\frac{e^3 \cdot n}{e^3 \cdot e_3}\right).$$

### 3.9.3 Turbulent Flow Considerations

When turbulent flow with wall functions is being treated, the fluid conductivity $k_f$ needs to be modified to include the effects of turbulence. This is done by considering the expression for wall heat flux in turbulent flows

$$\dot{q}_w = -K_s \nabla T \cdot n_w = \frac{\rho_f C_{pf} u_\tau \cdot (T_f - T_i)}{T^+} \tag{145}$$

Here, $T^+$ is evaluated from the thermal law of the wall, and the friction velocity, $u_\tau$, is

$$u_\tau = \left(\frac{\tau_w}{\rho}\right)^{\frac{1}{2}} \tag{146}$$

An effective fluid conductivity $\tilde{K}_f$ is next defined as

$$\frac{\rho_f C_{pf} u_\tau (T_f - T_i)}{T^+} = \tilde{K}_f \nabla T \cdot \boldsymbol{n}_w \tag{147}$$

to yield the expression for $\tilde{K}_f$

$$\tilde{K}_f \equiv \frac{\rho_f C_{pf} u_\tau \cdot \delta}{T^+} \tag{148}$$

where $\delta$ is the normal distance between the wall and the first cell.

$\tilde{K}_f$ is used in place of $K_f$ in all the equations presented in Section 3.9.

## 3.10 Turbulence Models

A number of turbulence models have been incorporated in the SCISEAL code for the computations of the turbulent flows that exist in the seal flows. The theoretical framework behind turbulence modeling is outlined in this section, followed by a description of the various models that are available. The choice of the particular model that should be used in computations often will depend on factors such as the type of the flow, constraints on grid sizes, and flow details and any particular physical characteristics.

### 3.10.1 Eddy Viscosity

Favre averaging, the basis for all the turbulence models in SCISEAL, has already been described in Section 3.2.4. We have also seen how Favre averaging introduces additional terms known as Reynolds stresses in the Favre-Averaged Navier-Stokes (FANS) equations and how these stresses are modeled using the Boussinesq eddy viscosity concept (see Equations 27 and 28). Following the kinetic theory of gases, the eddy viscosity is generally modeled as the product of a velocity scale $q$ and a length scale $\ell$

$$\mu_t = C \rho q \ell \tag{149}$$

where C is a constant of proportionality. Various models differ in the way $q$ and $\ell$ are estimated and each of the following sections describes a turbulence model. In the description of models, the overbar for $\mu$ and $\rho$, and tilde for $u$, $v$, *etc.* will be dropped for convenience.

### 3.10.2 Baldwin-Lomax Model

This belongs to the class of algebraic turbulence models because the velocity and length scales are obtained from algebraic relations. It is also commonly referred to as a mixing-length model because it employs Prandtl's mixing-length hypothesis in modeling length and velocity scales.

Baldwin and Lomax[12] developed this model primarily for wall-bounded flows. Like the mixing-length model of Cebeci and Smith[9], it employs different expressions for $\mu_t$ in the inner and outer parts of the boundary layer.

$$\mu_t = \begin{cases} \mu_{t\,inner} & for\ y \le y_{crossover} \\ \mu_{t\,outer} & for\ y \ge y_{crossover} \end{cases} \tag{150}$$

In the inner layer, Prandtl's mixing-length model and the Van Driest's damping function are used to estimate the length scale

$$\ell = \kappa y \left[1 - exp\left(-y^+ / A^+\right)\right] \tag{151}$$

where $A^+$ is the Van Driest's damping constant. $y^+$, the distance from the wall in wall units, is defined as

$$y^+ = y u_\tau / \nu, \quad u_\tau = \sqrt{\tau_w / \rho} \tag{152}$$

In the preceding expression $u_\tau$ is commonly known as the friction velocity with $\tau_w$ being the shear stress at the wall.

The velocity scale $q$ is modeled as the product of $\ell$ and the root mean square vorticity

$$|\omega| = \left[\left(\frac{\partial u}{\partial y} - \frac{\partial v}{\partial x}\right)^2 + \left(\frac{\partial v}{\partial z} - \frac{\partial w}{\partial y}\right)^2 + \left(\frac{\partial w}{\partial x} - \frac{\partial u}{\partial z}\right)^2\right]^{1/2} \tag{153}$$

Using the preceding expressions, the eddy viscosity in the inner layer is obtained as

$$\mu_{t\ inner} = \rho\, \ell^2\, |\omega| \tag{154}$$

The outer layer eddy viscosity is determined from the following expression

$$\mu_{t\ outer} = K\, C_{cp}\, \rho\, F_{wake}\, F_{kleb}(y) \tag{155}$$

where $K$ is the Clauser constant, $C_{cp}$ is an additional constant, and

$$F_{wake} = min\left\{y_{max}\, F_{max},\, C_{wk}\, y_{max}\, \frac{U_{dif}^2}{F_{max}}\right\} \tag{156}$$

The quantities $y_{max}$ and $F_{max}$ are determined from the function

$$F(y) = y\,|\omega|\,[1 - exp\,(-y^+/A^+)] \tag{157}$$

The quantity $F_{max}$ is the maximum value of $F(y)$ that occurs within the boundary layer and $y_{max}$ is the value of y at which the maximum occurs.

$F_{kleb}(y)$ is the Klebanoff intermittency factor given by

$$F_{kleb}(y) = \left[1 + 5.5\left(\frac{C_{kleb}y}{y_{max}}\right)^6\right]^{-1} \tag{158}$$

The quantity $U_{dif}$ is the difference between the maximum and minimum total

velocity in the boundary layer (*i.e.*, at a fixed x station)

$$U_{dif} = \sqrt{(u^2 + v^2 + w^2)_{max}} - \sqrt{(u^2 + v^2 + w^2)_{min}} \tag{159}$$

The second term in $U_{dif}$ is zero for stationary walls.

The values used for the constants appearing in the preceding expressions are

$$A^+ = 26 \quad C_{cp} = 1.6 \quad C_{kleb} = 0.3 \quad C_{wk} = 0.25 \quad \kappa = 0.4 \quad K = 0.0168$$

### 3.10.3 Standard k-ε Model

Several versions of k-ε models are in use today, but the model employed in the seals code is based on Launder and Spalding[13]. This model employs two partial differential equations to estimate the velocity and length scales and hence commonly known as the two-equation model. These equations are the k- and ε-equations which govern the transport of the turbulent kinetic energy (TKE) and its dissipation rate respectively. The modeled equations are

$$\frac{\partial}{\partial t}(\rho k) + \frac{\partial}{\partial x_j}(\rho u_j k) = \rho P - \rho \varepsilon + \frac{\partial}{\partial x_j}\left[\frac{\mu + \mu_t}{\sigma_k}\frac{\partial k}{\partial x_j}\right]$$

$$\frac{\partial}{\partial t}(\rho \varepsilon) + \frac{\partial}{\partial x_j}(\rho u_j \varepsilon) = C_{\varepsilon_1}\frac{\rho P \varepsilon}{k} - C_{\varepsilon_2}\frac{\rho \varepsilon^2}{k} + \frac{\partial}{\partial x_j}\left[\frac{\mu + \mu_t}{\sigma_\varepsilon}\frac{\partial \varepsilon}{\partial x_j}\right] \tag{160}$$

with the production $P$ defined as

$$P = \nu_t\left(\frac{\partial u_i}{\partial x_j} + \frac{\partial u_j}{\partial x_i} - \frac{2}{3}\frac{\partial u_m}{\partial x_m}\delta_{ij}\right)\frac{\partial u_i}{\partial x_j} - \frac{2}{3}k\frac{\partial u_m}{\partial x_m} \tag{161}$$

The square root of $k$ is taken to be the velocity scale while the length scale is obtained from

$$\ell = \frac{C_\mu^{3/4} k^{3/2}}{\varepsilon} \tag{162}$$

The expression for eddy viscosity is

$$\nu_t = \frac{C_\mu k^2}{\varepsilon} \tag{163}$$

The five constants used in the model are

$$C_\mu = 0.09\ ;\ C_{\varepsilon_1} = 1.44\ ;\ C_{\varepsilon_2} = 1.92\ ;\ \sigma_k = 1.0\ ;\ \sigma_\varepsilon = 1.3$$

The model uses wall functions to compute the turbulence quantities as well as the turbulent viscosity of the fluid at the computational points next to the walls. The wall functions described by Launder and Spalding[13], are derived from experimental and analytical knowledge of the one-dimensional Couette flow which exists near the wall. A semi-empirical universal function of non-dimensional distance normal to the wall, $y^+$, is

$$y^+ \equiv \frac{\rho\, \delta y \cdot u_\tau}{\mu} \tag{164}$$

In the above definition, $\delta y$ is the distance normal to the wall and $u_\tau$ is the "friction velocity" given by

$$u_\tau = \left(\frac{\tau_w}{\rho}\right)^{1/2} \tag{165}$$

In the internal sublayer $(y^+ > 11.63)$ the velocity variation may be described by a logarithmic relationship *i.e.*

$$u = \frac{u_\tau}{\kappa} \ell n \left(E y^+\right) \tag{166}$$

where $E = 9.70$ and $\kappa = 0.4034$ are experimentally determined constants.

In both the viscous ($y^+ \leq 11.63$) and internal ($y^+ > 11.63$) sublayers, the shear stress is calculated from the product of effective viscosity $\mu_{eff}$ and normal velocity gradient $\partial u/\partial y$, *i.e.*

$$\tau_w = \mu_{eff} \frac{\partial u}{\partial y} \tag{167}$$

where

$$\mu_{eff} = \begin{cases} \mu \text{ for } y^+ \leq 11.63 \\ \mu_{turb} \text{ for } y^+ > 11.63 \end{cases} \tag{168}$$

Near the wall, the transport equation for the turbulent kinetic energy, $k$, reduces to a balance between the local production and dissipation of $k$ to give

$$\mu_t \left( \frac{\partial \bar{u}}{\partial y} \right)^2 = \rho \varepsilon \tag{169}$$

The velocity gradient may be replaced from Equation (168) and the dissipation rate from

$$\mu_t = C_\mu \rho \frac{k^2}{\varepsilon} \tag{170}$$

to give

$$\tau_w = C_\mu^{1/2} \rho k = \rho u_\tau^2 \tag{171}$$

Hence, it follows from Equation (165)

$$\tau_w = \frac{\rho C_\mu^{1/4} k^{1/2} \bar{u}}{\frac{1}{\kappa} \ell n (E y^+)} \tag{172}$$

Evaluation of the heat flux at the wall in the enthalpy equation is also done by assuming a profile for temperature near the wall. For laminar flows, the wall heat flux is obtained from finite differences because linear variation of temperature is a good approximation close to the wall.

$$q_w = K \left.\frac{\partial T}{\partial y}\right|_w = K \frac{T}{y} \tag{173}$$

For turbulent flows, Reynolds analogy is assumed, *i.e.* the velocity and temperature profiles are assumed to be similar when plotted in wall coordinates. The wall heat flux is obtained from the following expression

$$T^+ = \frac{C_p\left(T - T_w\right) + \frac{1}{2}\sigma_{eff}\left(V^2 - V_w^2\right)}{q_w / \rho u_\tau} \tag{174}$$

$V$ and $V_w$ are the total velocities at the first grid-point and the wall respectively. $T^+$ at the first grid-point is obtained from a thermal law of the wall given below.

$$T^+ = \sigma u^+ \quad for\ y^+ \le y_T^+ \tag{175}$$

$$= \sigma_t\left(u^+ P^+\right) \quad for\ y^+ > y_T^+ \tag{176}$$

In the preceding relations, $P^+$ is a parameter which is dependent on the fluid Prandtl numbers while $y_T^+$ is the value of $y^+$ at which both the expressions (175) and (176) yield the same value of T.

$$P^+ = q\left(\frac{\sigma}{\sigma_t} - 1\right)\left(\frac{\sigma_t}{\sigma}\right)^{1/4} \tag{177}$$

If $\sigma = 0.7$ and $\sigma_t = 0.9$ we get $P^+ = -2.13$ and $y_T^+ = 9.585$.

### 3.10.4 Multiple-Scale Model

Most turbulence models, including the standard k-ε model, assume one time scale for both the production and the dissipation rates of turbulence. However, experiments and the Direct Numerical Simulation (DNS) of turbulence have shown that most of the turbulence production occurs at large scales (energy carrying eddies) and is cascaded to smaller scales (dissipative eddies) where most of the dissipation takes place. Several authors (*e.g.*, Hanjalic *et al.*,[14]; Fabris *et al.*,[15]) have suggested partitioning of the energy spectrum into production range $k_p$ and dissipation range $k_t$, the sum of the two quantities being $k$. Kim and Chen[16] have developed a multiple time-scale turbulence model based on variable partitioning of turbulent kinetic energy. The partitioning is determined as a part of the solution and depends on local turbulence intensity, production, energy transfer and dissipation rate. The partition is moved into higher wave numbers when production is high, and to low wave numbers when production vanishes. The model uses a transport equation for each $k_p$, $k_t$, $\varepsilon_p$ and $\varepsilon_t$, however these equations differ from each other only in the source terms.

$$\frac{\partial}{\partial t}(\rho k_p) + \frac{\partial}{\partial x_j}(\rho\, u_j\, k_p) = \rho P - \rho\varepsilon_p + \frac{\partial}{\partial x_j}\left(\frac{\mu+\mu_t}{\sigma_{kp}}\frac{\partial k_p}{\partial x_j}\right)$$

$$\frac{\partial}{\partial t}(\rho k_t) + \frac{\partial}{\partial x_j}(\rho u_j k_t) = \rho\,\varepsilon_p - \rho\,\varepsilon_t + \frac{\partial}{\partial x_j}\left(\frac{\mu+\mu_t}{\sigma_{kt}}\frac{\partial k_t}{\partial x_j}\right)$$

$$\frac{\partial}{\partial t}(\rho\varepsilon_p) + \frac{\partial}{\partial x_j}(\rho u_j \varepsilon_p) = C_{\varepsilon p_1}\frac{\rho P^2}{kp} + C_{\varepsilon p_2}\frac{\rho P\varepsilon_p}{kp} - C_{\varepsilon p_3}\frac{\rho\,\varepsilon_p^2}{kp} + \frac{\partial}{\partial x_j}\left(\frac{\mu+\mu_t}{\sigma\varepsilon_p}\frac{\partial\varepsilon_p}{\partial x_j}\right)$$

$$\frac{\partial}{\partial t}(\rho\varepsilon_t) + \frac{\partial}{\partial x_j}(\rho u_j \varepsilon_t) = C_{\varepsilon t_1}\frac{\rho\varepsilon P^2}{kt} + C_{\varepsilon t_2}\frac{\rho P\varepsilon_p\,\varepsilon_t}{kt} - C_{\varepsilon t_3}\frac{\rho\,\varepsilon_t^2}{kt} + \frac{\partial}{\partial x_j}\left(\frac{\mu+\mu_t}{\sigma\varepsilon_t}\frac{\partial\varepsilon_t}{\partial x_j}\right) \qquad (178)$$

The eddy viscosity is defined as

$$v_t = C_\mu\, k^2/\varepsilon_p \qquad (179)$$

where $k$, the total TKE, is calculated as

$$k = k_p + k_t \tag{180}$$

The model constants are

$C_\mu = 0.09;\ \sigma_{kp} = \sigma_{kt} = 0.75;\ \sigma_{\varepsilon p} = \sigma_{\varepsilon t} = 1.15$

$C_{\varepsilon p1} = 0.21;\ C_{\varepsilon p2} = 1.24;\ C_{\varepsilon p3} = 1.84;\ C_{\varepsilon t1} = 0.29;\ C_{\varepsilon t2} = 1.28;\ C_{\varepsilon t3} = 1.66$

### 3.10.5 Low Reynolds Number Model

All three models described above, viz. the Standard k-ε model, the extended k-ε model, and the multiple time scale model, are of high-Reynolds number form and therefore require the used of wall functions. However, the commonly used wall functions may not be accurate in flows with large separation, suction, blowing, heat transfer, relaminarization, *etc.* This difficulty associated with wall functions can be reduced by the use of low-Reynolds number k-ε models which permit integration of momentum and k-ε equations all the way to the wall. The k-ε equations are modified as shown below to include the effect of molecular viscosity in the near wall regions.

$$\begin{gathered}
\frac{\partial}{\partial t}(\rho k) + \frac{\partial}{\partial x_j}(\rho u_j k) = \frac{\partial}{\partial x_j}\left[\frac{\mu + \mu_t}{\sigma_k}\frac{\partial k}{\partial x_j}\right] + \rho (P - \varepsilon - D) \\
\frac{\partial}{\partial t}(\rho \varepsilon) + \frac{\partial}{\partial x_j}(\rho u_j \varepsilon) = \frac{\partial}{\partial x_j}\left[\frac{\mu + \mu_t}{\sigma_\varepsilon}\frac{\partial \varepsilon}{\partial x_j}\right] + C_{\varepsilon_1} f_1 \frac{\rho P \varepsilon}{k} - C_{\varepsilon_2} f_2 \frac{\rho \varepsilon^2}{k} + E \\
\mu_t = C_\mu f_\mu \frac{\rho k^2}{e}
\end{gathered} \tag{181}$$

Several versions low-Reynolds number k-ε models are available today. After a careful analysis of the comparative studies done by Patel *et al.*[17], Brankovic and Stowers[18], Avva *et al*[19], the low-Re model of Chien[20] was selected for implementation in the seals code. The model parameters appearing in the preceding equations are:

$$\begin{gathered}
C_\mu = 0.09\ ;\ C_{\varepsilon_1} = 1.35\ ;\ C_{\varepsilon_2} = 1.8\ ;\ \sigma_k = 1.0\ ;\ \sigma_\varepsilon = 1.3 \\
f_\mu = 1 - exp(-0.0115\ y^+)\ ,\ f_1 = 1.0\ ;\ f_2 = 1 - 0.22\ exp\left[-(R_t/6)^2\right] \\
D = 2\nu k/y^2\ ;\ E = -2\nu(\varepsilon/y^2)\ exp\ (-0.5\ y^+)
\end{gathered} \tag{182}$$

### 3.10.6 2-Layer Model

The usual choice of turbulence models: the high- and low-Reynolds number models can be applied depending on the flow conditions and the grid sizes available. The model applicability depends on the distance of the first computational node from the wall. For the High-Re model, this distance, expressed in terms of the nondimensional distance $y+$, must be greater than 11.5 for the model to be accurate. On the other hand, the low-Re model required that the near-wall point be in the laminar sub-layer, at $y+$ of below 1. Computationally the high-Re model is robust and is the preferred choice. The low-Re model, under some circumstances becomes extremely stiff, and is harder to use.

In seal flows, the narrow clearances typically can generate very low near-wall distances, even for relatively coarse grids. In such cases, when $y+$ falls below 11.5, the more robust standard k-ε loses accuracy, and tends to overpredict the wall-shear. Use of the low-Re model in these cases will be more appropriate, however, the solutions are grid sensitive, and computationally stiff. In some cases, such as flows in labyrinth and grooved seals, there are regions where the flow is fast (*e.g.* laby seal tip gap), while in some regions it is quite slow (laby cavity). In a flow of this type, even a coarse grid will generate very low $y+$ values in the cavity region, while the tip-gap region has relatively high near-wall $y+$ distances. In such a case, neither of the above models can be applied either due to loss of accuracy (high-Re model), or prohibitively large grid sizes (low-Re models). To treat such type of problems, a 2-layer model of wall treatment has been incorporated. The model provides the accuracy of the low-Re model for very low $y+$, and smoothly blends to a high-Re solution at higher $y+$ values.

In the outer layer, the standard k-ε equations govern the transport or turbulence and the eddy viscosity is computed as

$$\mu_t = C_\mu \frac{k^2}{\varepsilon} \tag{183}$$

In the inner layer where the molecular viscosity is either dominant or comparable to eddy viscosity, Equation (183) is replaced by

$$\mu_t = C_\mu \sqrt{k}\, l_\mu \tag{184}$$

The viscosity length scale $l_\mu$ is determined using a Van Driest type correlation

$$l_\mu = C_l\, y \left[1 - exp\left(-\frac{Re}{a}\right)\right] \tag{185}$$

$Re$ is a local Reynolds number based on TKE

$$Re = \frac{\sqrt{k}\, y}{\nu} \tag{186}$$

For conformity with the log law, $C_l$ is taken as

$$C_l = \frac{\kappa}{C_\mu^{3/4}} \tag{187}$$

where $\kappa$ is the von Karman constant.

In the inner layer, the $\varepsilon$-equation is replaced by an algebraic length scale equation

$$\varepsilon = \frac{k^{3/2}}{l_\varepsilon} \tag{188}$$

where the dissipation length scale $l_\varepsilon$ is modeled as

$$l_\varepsilon = \frac{C_l y}{1 + b/Re} \tag{189}$$

Rodi[21] recommends the following values for constants $a$ and $b$ appearing in Equations (185) and (189):

$$a = 50.5 \qquad b = 5.3$$

To be consistent with the standard wall functions, $\kappa$ in Equation (187) is taken to be 0.433. Note that a value of 0.40334 is used for $\kappa$ appearing the log law $u^+ = 1/\kappa\,(Ey^+)$.

Equation (184) may be recast by using Equation (188)

$$\nu_t = C_\mu \sqrt{k}\, l_\mu = C_\mu\, l_\mu \frac{\sqrt{k}}{\varepsilon} \cdot \varepsilon$$

$$= C_\mu\, l_\mu \frac{\sqrt{k}}{\varepsilon} \frac{k^{3/2}}{l_\varepsilon} = C_\mu \frac{l_\mu}{l_\varepsilon} \frac{k^2}{\varepsilon} = C_\mu\, f_\mu \frac{k^2}{\varepsilon} \tag{190}$$

Equation (190) resembles the typical formulation employed by most low-Re models. $f_\mu$ is the ratio of viscosity length scale to dissipation length scale. Two-layer model is based on the premise that the viscosity length scale is smaller than the dissipation length scale inside the inner layer, but equal in the outer layer.

$$f_\mu = \frac{l_\mu}{l_\varepsilon} = \frac{1 - \left(exp\, \frac{Re}{a}\right)}{\left(\frac{1}{1 + 5.3/Re}\right)} \tag{191}$$

Note that $f_\mu$ is strictly a function of Re only. The location where $f_\mu$ becomes unity is used in the present formulation as a matching criterion.

| Re | Numerator of Eq. (2.116) | Denominator of Eq. (2.116) | $f_\mu$ |
|---|---|---|---|
| 1 | 0.0196 | 0.1587 | 0.12348 |
| 10 | 0.1796 | 0.6536 | 0.275 |
| 100 | 0.862 | 0.9497 | 0.9076 |
| 180 | 0.97168 | 0.9714 | 1.0003 |
| 200 | 0.981 | 0.9742 | 1.007 |
| 1000 | 0.9999997 | 0.99473 | 1.0053 |

## 3.11 Solution Methods

SCISEAL uses a pressure-based, iterative segregated solution procedure. The equations for the flow variables are solved in a sequential manner, and respectedly till a convergent solution is obtained. The overall solution method for SIMPLEC and PISO algorithm is presented in this section.

### 3.11.1 SIMPLEC Algorithm

The overall solution procedure for the SIMPLEC algorithm is shown in Figure 11. Note that all the parameters that dictate how many times a procedure is repeated can be specified by the user. These are the number of iterations (NITER), the number oc continuity iterations (C_ITER) and, in the case of transient simulation, the number of time steps (NTSTEP). The procedure for a steady-state simulation is simply repeated at each time step of a transient simulation. The number of iterations to be performed is dictated by the overall residual reduction obtained. At each iteration the program will calculate a residual for each variable which is the sum of the absolute value of the residual for that variable at teach control cell. The residuals are not normalized, and hence the convergence criterion should be based on the reduction of residuals rather than on the absolute values. A drop of 4-5 orders of magnitude is usually sufficient to consider the solution as converged.

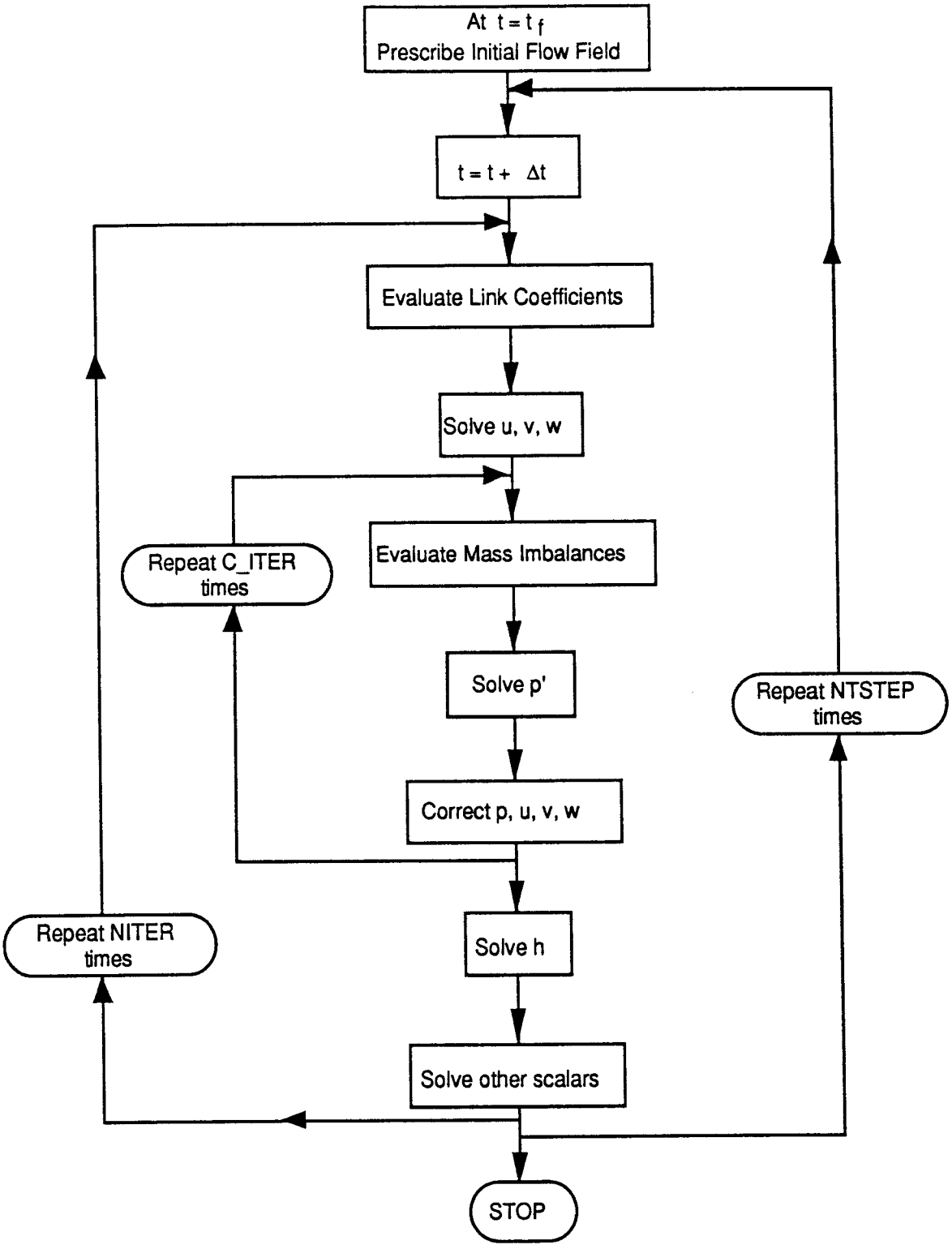


Figure 11. Solution Flowchart for SIMPLEC Algorithm

### 3.11.2 PISO Algorithm

The overall solution procedure for the PISO algorithm is shown in Figure 12. Although PISO is an inherently transient procedure, it can be applied to steady state problems. In this case, the number of iterations (NITER) is comparable to the number of time steps performed in a transient simulation. The time increment through which the solution is allowed to advance at each time step is controlled by the under-relaxation factor applied and the time-asymptotic solution is sought.

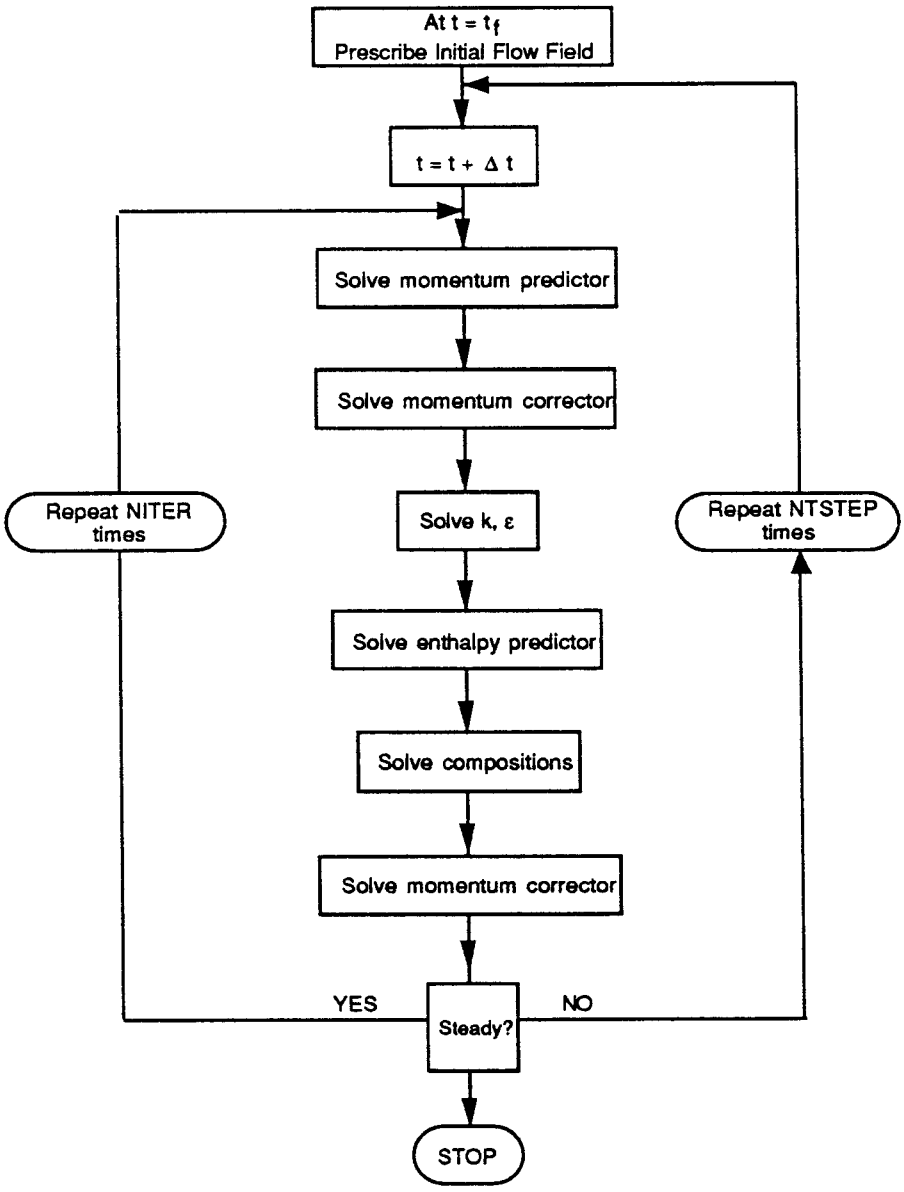


Figure 12. Solution Flowchart for PISO Algorithm

### 3.11.3 Under-Relaxation

Under-relaxation of dependent and auxiliary variables is used to constrain the change in the variable from iteration to iteration in order to prevent divergence of the solution procedure. For all dependent variable except the pressure correction, this is done by modifying Equation (66) in the following way

$$a_P(1+I)\phi_P = \Sigma a_{nb}\phi_{nb} + S_U + a_P I \phi_P^* \tag{192}$$

Where $\phi^*_p$ is the last iteration value. At convergence, $\phi^*_p$ and $\phi_p$ are same and effect of $I$ disapperars. During the iterative procedure, the factor $I$ increases the diagonal term associated with $\phi_p$ and in effect reduces the corrections made in $\phi^*_p$ to get $\phi_p$. A larger value of $I$ thus implies a higher relaxation.

If we express $I$ in the form of a transient term link coefficient

$$I = \frac{\rho \forall}{\Delta t_f a_p} \tag{193}$$

Then $\Delta t_f$ can be viewed as a pseudo time step. In SCISEAL the value of $I$ is specified directly and values between 0.2 and 0.8 are common. Higher relaxation may be needed for difficult problems.

The auxiliary variables $\rho$, $P$, $T$ and $v$ can be under-relaxed by specifying a linear under-relaxation factor, $\alpha$, which is applied in the following way

$$\theta^{new} = \alpha\theta + (1-\alpha)\theta^* \tag{194}$$

where $\theta^{new}$ is the updated value of the auxiliary variable, $\theta$ is the value of that auxiliary variable that would be calculated with no under-relaxation and $\theta^*$ is the current iteration value of the auxiliary variable.

### 3.11.4 Linear Equation Solvers

The discretized flow equation for each grid cell are interlinked with neighboring

cells, and when assembled generate a set of coupled linear equations. These can be written in the matrix form as

$$[A]\,\phi = S$$

Due to the nature of the structured grid, the matrix $A$ is sparse and has a diagonal banded structure. The individual non-zero elements of $A$ are the link coefficients associated with each flow cell. The matrix $A$ has to be inverted to get the solution vector $\phi$. This can be done in SCISEAL using two types of linear equation solvers.

**3.11.4.1 Whole Field Solver** Whole field solvers are based on the strongly implicit procedure (SIP). The method involves modification of the original linear equation set as

$$[A + B]\phi = S + [B]\phi \tag{195}$$

The matrix $B$ is such that $A + B$ is easily factored into upper and lower triangular matrices $L$ and $U$. Further more, L and U matrices together have the same number of non-zero diagonals as the original matrix $A$. The modified equation then becomes.

$$[L]\,[U]\phi = S + [B]\phi \tag{196}$$

This can also be expressed as

$$[L]V = S + [B]\phi \tag{197}$$

where

$$V = [U]\phi \tag{198}$$

An iterative procedure can then defined and used

$$\textit{Evaluate } V^{k+1} \textit{ from } [L]V^{k+1} = S + [B]\phi^{k}$$
$$\textit{Evaluate } \phi^{k+1} \textit{ from } [U]\phi^{k+1} = V^{k+1}$$

The whole-field solvers in SCISEAL use this procedure. The form of L and U is such that points along lines in one of the coordinate direction are linked implicitly through tri-diagonal arrays. There are, therefore, three of the solvers named the WHOLE-X, WHOLE-Y and WHOLE-Z solvers.

**3.11.4.2 Conjugate Gradient Squared Solver** Conjugate gradient type solvers have many advantages over classic iterative methods such as suitability for vectorization and the lack of user-specified parameters. The CGS algorithm has been incorporated into the SCISEAL program. The CGS algorithm applied to the system $A\phi = S$ is expressed as follows

$$\textit{Initialization } (n=0) \quad r_o = S - A\phi_o$$
$$q_o = p_{-1} = 0;\ \rho_{-1} = 1$$

$$\textit{Iteration } (n \geq 0) \quad \rho_n = r_o^{\,T} r_n;\ \beta_n = \frac{\rho_n}{\rho_{n-1}}$$

$$u_n = r_n + \beta_n q_n$$

$$p_n = u_n + \beta_n (q_n + \beta_n p_{n-1})$$

$$v_n = A p_n$$

$$\sigma_n = r_o^{\,T} v_n;\ \alpha_n = \frac{\rho_n}{\sigma_n}$$

$$q_{n+1} = u_n - \alpha_n v_n$$

$$r_{n+1} = r_n - \alpha_n A (u_n + q_{n+1})$$

$$\phi_{n+1} = \phi_n + \alpha_n (u_n + q_{n+1})$$

The convergence rate of conjugate gradient algorithms depends on the spectral radius of the coefficient matrix and can be effectively accelerated by preconditioning

the system. This preconditioning is accomplished by transforming the system $\tilde{A}\,\phi = p^{-1} A\,\phi = p^{-1} S$. Incomplete Cholesky decomposition is used as a preconditioner in SCISEAL.

### 3.12 Rotordynamic Coefficient Calculations

As a rotor rotates in a fluid seal, the fluid forces developed in the seal play an important part in the overall stability of the rotating machinery. The forces developed in a seal can be large enough to destabilize a rotor, or stabilize an otherwise unstable system. The seal force characteristics also play an important part in determining the critical frequencies of a rotating system.

The seal flow forces generated when a rotor moves in the seal are related to the rotor center displacement, velocity and accelerations (Figure 13) through the following relation

$$-\begin{bmatrix} F_y \\ F_z \end{bmatrix} = \begin{bmatrix} K_{yy} & K_{yz} \\ -K_{zy} & K_{zz} \end{bmatrix} \begin{bmatrix} y \\ z \end{bmatrix} + \begin{bmatrix} C_{yy} & C_{yz} \\ -C_{zy} & C_{zz} \end{bmatrix} \begin{bmatrix} \dot{y} \\ \dot{z} \end{bmatrix} + \begin{bmatrix} M_{yy} & M_{yz} \\ -M_{zy} & M_{zz} \end{bmatrix} \begin{bmatrix} \ddot{y} \\ \ddot{z} \end{bmatrix} \tag{199}$$

where $F_y$ and $F_z$ are the fluid reaction forces as a result of rotor center motion, $K_{yy}$,$K_{zz}$ the direct stiffness coefficients, $K_{yz}$,$K_{zy}$ the cross-coupled stiffness coefficients, $C_{yy}$,$C_{zz}$ the direct damping coefficients, $C_{yz}$,$C_{zy}$ the cross-coupled damping coefficients, $M_{yy}$,$M_{zz}$ the direct inertia (mass) coefficients, and $M_{yz}$,$M_{zy}$ the cross-coupled inertia coefficients. These coefficients relate the reaction forces to the rotor center displacents, velocities and accelerations $y, z, \dot{y}\,\dot{z}, \ddot{y}, \ddot{z}$. The values and signs of these coefficients determine the effect of the fluid flow in the seal on the dynamic characteristics of the supported rotor system.

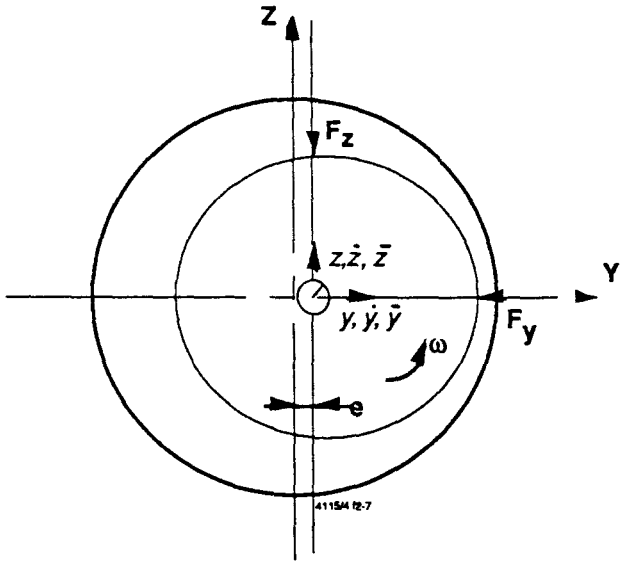


Figure 13. Rotor Displacement, Velocity and Acceleration and Fluid Reaction Forces in a Generic Seal Configuration

At present there are two different methods available in the SCISEAL code to evaluate these coefficients. These are:

a. whirling rotor method; and
b. small-perturbation method.

The whirling rotor method is based on computations that involve the full CFD solution of the seal flow. The perturbation method is based on computations of the perturbed fluid flow under a prescribed, small rotor motion. A description of these methods follow.

### 3.12.1 Whirling Rotor Method

In this method, the seal rotor is assumed to undergo a whirl such that the rotor center describes a circle about the stator center (Figure 14). Such a problem is time-dependent, but the circular rotor whirl orbit allows a coordinate-frame transformation that renders the problem quasi-steady. This is done by using a reference frame that has the origin at the stator center and is rotating with the rotor at its whirl speed. In this frame, rotor appears stationary, and a steady-state analysis is possible with the inclusion of appropriate body forces in the momentum

equations. A description of this transformation is given after the treatment for the perturbation method, as well as in Reference 45.

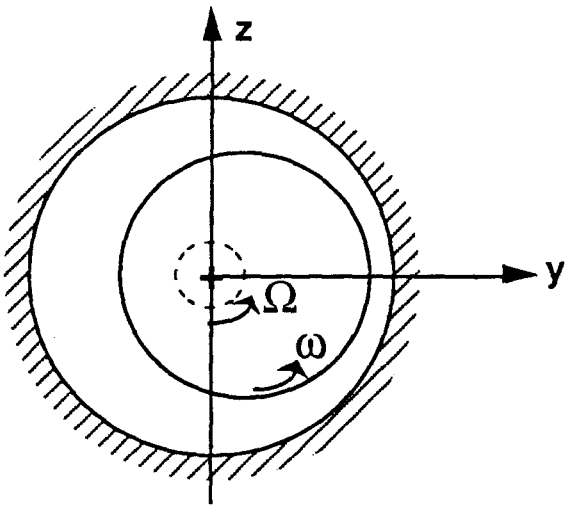


Figure 14. Seal Configuration for the Circular Whirl Orbit Method for Rotordynamics

Since the rotor whirls around the stator center, the system can generate only a skew-symmetric set of rotordynamic coefficients described as

$$-\begin{bmatrix} F_y \\ F_z \end{bmatrix} = \begin{bmatrix} K & k \\ -k & K \end{bmatrix} \begin{bmatrix} y \\ z \end{bmatrix} + \begin{bmatrix} C & c \\ -c & C \end{bmatrix} \begin{bmatrix} \dot{y} \\ \dot{z} \end{bmatrix} + \begin{bmatrix} M & m \\ -m & M \end{bmatrix} \begin{bmatrix} \ddot{y} \\ \ddot{z} \end{bmatrix} \tag{200}$$

where $K,k$ now are the direct and cross-coupled stiffness coefficients, $C,c$ are the direct and cross-coupled damping coefficients, and $M,m$ are the direct and cross-coupled inertia coefficients. These are assumed to be independent of the whirl frequency $\Omega$ . Next, we use the definitions of the displacement of the rotor center

$$\begin{aligned} y &= r_o cos\,(\Omega t) \\ z &= r_o sin\,(\Omega t) \end{aligned} \tag{201}$$

to calculate the rotor center velocities and accelerations, with $r_0$ as the radius of the whirl orbit. These are then used in Equation (200) to yield relations between reaction forces and various rotordynamic coefficients

$$-\frac{F_y}{r_o} = K + c\Omega - M\Omega^2$$
$$-\frac{F_z}{r_o} = -k + C\Omega + m\Omega^2 \qquad (202)$$

The calculation procedure then involves computations of the CFD solutions in the seal with whirling rotor at several different whirl frequencies (at least 3). The pressure fields on the rotor surface are integrated at each whirl frequency to provide $F_y$ and $F_z$ as functions of the whirl frequency. An appropriate curve-fit is used on the force vs. whirl frequency curves to yield the rotordynamic coefficients.

As mentioned earlier, this method is applicable to the centered rotor position. When the rotor whirls about a non-centered position, even the use of a rotating frame of reference cannot make the problem quasi-steady. For this reason, the skew-symmetric dynamic coefficient set can be calculated using this method.

### 3.12.2 Small Perturbation Method

This method is based on the solutions of perturbations in the seal flow field under a prescribed small motion of the rotor center about a given nominal position (similar to the method described by Nordmann and Dietzen[22]). The perturbation variables can be solved using a quasi-steady solution method to yield the fluid reaction forces. The method is sufficiently general to include statically eccentric and/or misaligned seals.

In this method, the rotor of the seal is assumed to undergo a circular whirl around a given nominal position, with a very small orbit radius $r_o$, given by

$$r_o = eC_o \qquad (203)$$

where $C_o$ is a reference length, *e.g.* the nominal seal clearance, and $e$ is a small number. In the nominal position, the rotor can be centered, eccentric and/or misaligned. A time-dependent flow field exists in the seal as a result of the rotor motion, and the flow variables are assumed to have the form, *e.g.*,

$$u = u_o + eu_1$$
$$v = v + ev_1 \tag{204}$$

where $u_o$, $v_o$ correspond to the steady-state seal flow solutions with the rotor in the nominal position (0th order), and $u_1$, $i$ are the time-dependent perturbation solutions (1st order). Using these definitions in the Navier-Stokes equations, ignoring terms with $e^2$ and higher terms, and separating out the 0th and 1st order terms, the governing equations for the two sets of variables are generated. Since the rotor center motion is a combination of sine and cosine functions of time, the 1st order flow variables are also assumed to have the form, *e.g.*,

$$u_1 = u_{1c} \cos(\Omega t) + u_{1s} \sin(\Omega t)$$
$$v_1 = v_{1c} \cos(\Omega t) + v_{1s} \sin(\Omega t) \tag{205}$$

where $u_{1c}$, $u_{1s}$ *etc.* are functions of space only. Similar definitions for all flow variables are assumed and substituted in the 1st order flow equations. By separating out the terms containing $sin(\Omega t)$ and $cos(\Omega t)$ in each of the equations, two equations for each of the 1st order flow quantity can be obtained (*i.e.* one equation each for quantities like $u_{1c}$, $u_{1s}$ and so on).

The next step involves regrouping and redefining new 1st order variables such as:

$$\hat{u}_1 = u_{1c} + i\, u_{1s}$$
$$\hat{v}_1 = u_{1c} + i\, v_{1s} \tag{206}$$

where $i = \sqrt{-1}$ . The equations for these complex quantities are generated in a similar fashion:

$$(Equation\ for\ \hat{u}_1) = (Equation\ for\ u_{1c}) + i\,(Equation\ for\ u_{1s}) \tag{207}$$

The resulting equations have a form very similar to the 0th order equations. Thus, the momentum equation for $\hat{u}_1$ has the form:

$$-i\Omega\left(\rho_o \hat{u}_1 + \hat{\rho}_1 u_o\right) J + \frac{\partial}{\partial \xi^k}\left(J\rho_o u_o \vec{V}_g \cdot \varepsilon^k\right) + \frac{\partial}{\partial \xi^k}\left(J\rho_o \hat{u}_1 \vec{V}_o \cdot \varepsilon^k\right)$$
$$+ \frac{\partial}{\partial \xi^k}\left(J\hat{\rho}_1 u_o \vec{V}_o \cdot \varepsilon^k\right) + \frac{1}{J}\frac{\partial}{\partial \xi^k}\left(J\rho_o u_o \hat{\vec{V}}_1 \cdot \varepsilon^k\right) = \frac{\partial}{\partial \xi^k}\left(J\Gamma g^{jk}\frac{\partial \hat{u}_1}{\partial \xi^j}\right) + S_{u1} \tag{208}$$

where $S_{u1}$ contains the complex source terms that arise due to the complex convective and diffusive fluxes as well as the grid transformations. The continuity and energy equations are transformed in a similar fashion, and both contain additional complex source terms. Several points to note here are: a) The momentum equations are linear, since the convective terms contain the 0th order fluxes which are constant; 2) the equations are similar in form to the base 0th order equations, so that a similar solution procedure can be used and 3) the 1st order variables are complex quantities, so that complex algebra is required for their solutions.

The perturbations are assumed to be small enough so that the turbulence quantities: k, ε and the turbulent viscosities are assumed unchanged in the 1st order equations. This reduces the 1st order set to only the momentum, continuity and energy equations (for compressible flows) only.

The overall solution procedure is:

a. calculation of the steady-state, 0th order solutions of the Navier-Stokes equations for the seal flow with the rotor in the nominal position;
b. solution of the 1st order equations using the 0th order convective fluxes and turbulent quantities; and
c. use the resulting pressure field to calculate the rotordynamic coefficients.

Once the 1st order pressure field is known, it is integrated over the surface of the rotor and the resulting time dependent forces are decomposed into Y and Z components to yield $F_{yr}$, $F_{yi}$, $F_{zr}$, and $F_{zi}$ as given below:

$$F_{yr} = \frac{1}{C_o}\int_\theta \int_x p_{1c} \cdot \hat{n}_y (r d\theta dx) \tag{209a}$$

$$F_{yi} = \frac{1}{C_o}\int_\theta \int_x p_{1s} \cdot \hat{n}_y (rd\theta dx) \tag{209b}$$

$$F_{zx} = \frac{1}{C_o}\int_\theta \int_x p_{1s} \cdot \hat{n}_z (rd\theta dx) \tag{209c}$$

$$F_{zr} = \frac{1}{C_o}\int_\theta \int_x p_{1c} \cdot \hat{n}_z (rd\theta dx) \tag{209d}$$

where $\hat{n}_y$ and $\hat{n}_z$ are the components of the local surface normals in the y and z Cartesian directions. Using the definition of the displacement of the rotor center

$$\begin{aligned} y &= r_o \cos(\Omega t) \\ z &= r_o \sin(\Omega t) \end{aligned} \tag{210}$$

the rotor center velocity and accelerations are calculated. These are then substituted together with the definitions in Equations (209) in the basic force-displacement relation, Equation (199). Collecting terms with $cos(\Omega t)$ and $sin(\Omega t)$, four equations linking the integrated reaction forces and the whirl speed $\Omega$ are generated, as given below:

$$\begin{aligned} -F_{yr} &= K_{yy} - C_{yz}\Omega - M_{yy}\Omega^2 \\ -F_{yi} &= K_{yz} - C_{yy}\Omega - M_{yz}\Omega^2 \\ -F_{zr} &= -K_{zy} + C_{zz}\Omega - M_{zy}\Omega^2 \\ -F_{zi} &= K_{zz} + C_{zy}\Omega - M_{zz}\Omega^2 \end{aligned} \tag{211}$$

As in the whirling rotor method, the solutions of the 1st order quantities are generated at several different whirl frequencies $\Omega$, and appropriate curves are fitted to the $F_{yr}$, $F_{yi}$ *etc.* vs. frequency curves to yield all the rotordynamic coefficient.

As stated earlier, this method generated the full, non-symmetric set of coefficients, and can be extended to generate the coefficients due to angular displacements. The

overall solution procedure requires the solutions of several quasi-steady problems, and hence is computationally fast.

### 3.12.3 Grid Transformation for Concentric Whirling Rotor

When a rotor whirls inside a seal, the moving surface of the rotor generates a deforming grid which produces a time-dependent flow. This flow can be solved using the moving grid method described earlier. This problem is time-dependent and hence computationally expensive. In a special case of rotor whirl, however, it is possible to change the frame of reference and render the problem quasi-steady. This special case refers to the rotor whirl which has a circular orbit and stator center as the orbit center. This transformation is the basis of the whirling rotor method and following is a brief description of the transformation and the resulting flow problem.

The whirling rotor is shown in Figure 15. The spin speed is $\omega_x$ rad/s and the whirl speed is $\Omega_x$ rad/s. The figure shows the rotor when its center is in orbit at one time instant. The orbit radius is $\varepsilon$ and $r_r$ is the radius vector of a typical point on the rotor surface with respect to the rotor center.

To render this problem quasi-steady, one must switch the reference frame such that in the transformed frame, the flow domain appears non-deforming even when it deforms in the absolute reference frame. When a rotor is whirling in a circular orbit, this transformed frame corresponds to a frame that is rotating at rotor whirl speed, has the stator center as the origin, and stator axis as the axis of rotation.

To understand this transformation, refer to Figure 16. In this figure the positions of the rotor center at two different time instances are shown. Also shown are two local reference frames such that the local Y′ axis always joins the stator center and the minimum clearance point. In the local Y′ – Z′ frame the flow domain now appears unchanged, and hence Y′ – Z′ is the reference frame we need. Since the minimum clearance point moves at whirl speed $\Omega_x$, so does the Y′ – Z′ plane.

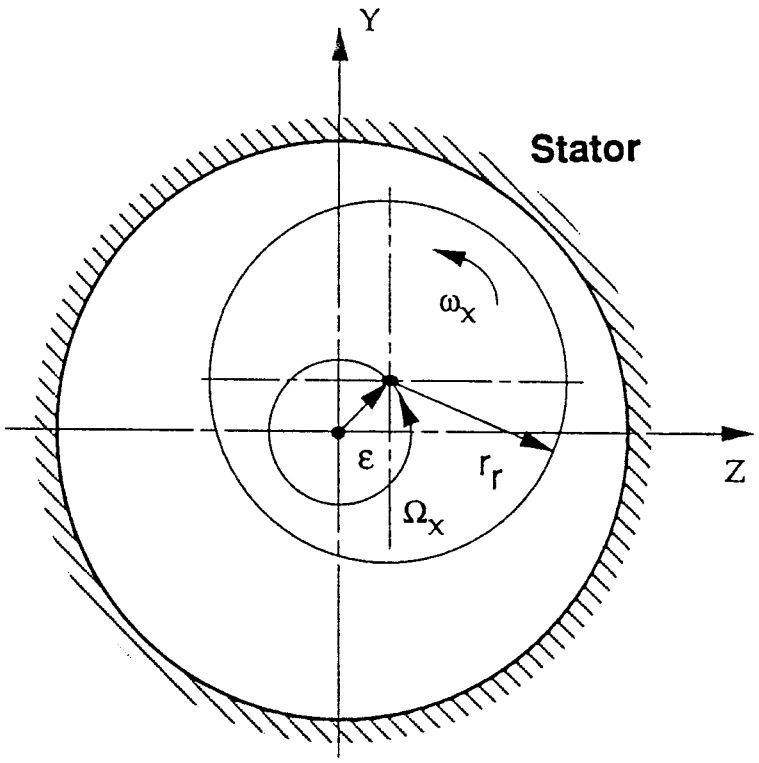


Figure 15. Schematic of a Spinning Rotor Whirling in a Circular Orbit about the Stator Center

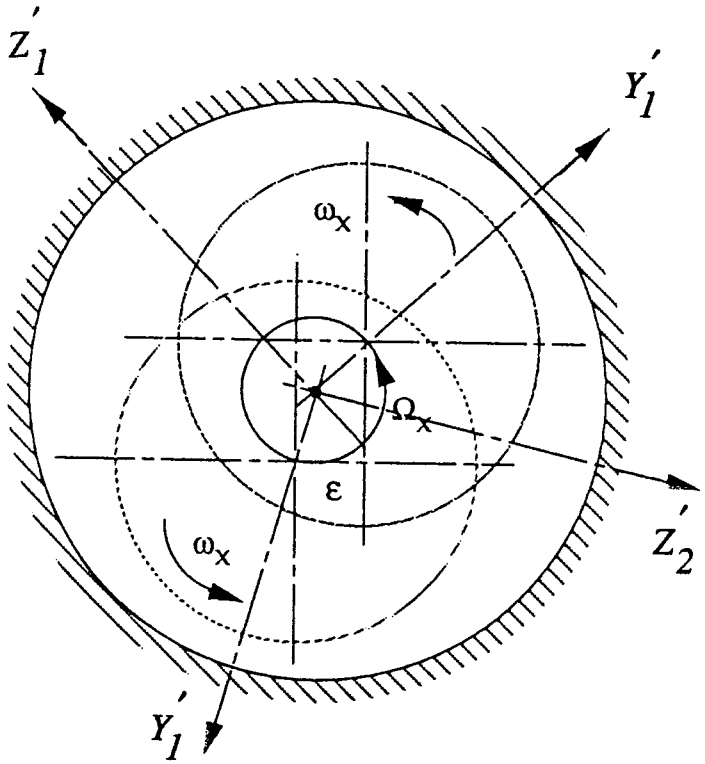


Figure 16. Positions of the Whirling Rotor at Two Time Instants. Also Shown are the 'Local' Reference Frames y' - z' at these Two Instances.

The changes in the flow equations as a result of this rotating frame transformation involve addition of the centrifugal and Coriolis accelerations to the momentum equations. The wall boundary conditions also need to be transformed. This needs care and the procedure is outlined below. Referring to Figure 17, the absolute wall velocities are:

stator $$\vec{V}_{s,a} = 0 \tag{212}$$

and

rotor $$\vec{V}_{r,a} = \vec{\omega}_x \times \vec{r}_r + \vec{\Omega}_x \times \vec{\varepsilon} \tag{213}$$

where $\vec{r}_r$, $\vec{\varepsilon}$ *etc.* refer to the position vectors of surface points. For the rotor surface the total velocity is a combination of the rotor spin and whirl speeds. Transformation to the rotating frame involves subtraction of a velocity of the type

$$V_\theta = \vec{\Omega}_x \times \vec{R} \tag{214}$$

from all wall velocities, where $\vec{R}$ refers to the radius vector with respect to the stator center as shown in Figure 17. With this transformation the surface velocities relative to the transformed frame become:

Stator: $$\vec{V}_{r,r} = \vec{V}_{s,a} - \vec{\Omega}_x \times \vec{R}_s = -\vec{\Omega}_x \times \vec{R}_s \tag{215}$$

Rotor: $$\vec{V}_{r,r} = \vec{V}_{r,a} - \vec{\Omega}_x \times \vec{R}_r = \vec{\omega}_x \times \vec{r}_r + \vec{\Omega}_x \times \vec{\varepsilon} - \vec{\Omega}_x \times \vec{R}_r \tag{216}$$

Noting that $$\vec{R}_r = \vec{r}_r + \vec{\varepsilon} \tag{217}$$

we get the rotor velocity as $$\vec{V}_{r,r} = \left(\vec{\omega}_x - \vec{\Omega}_x\right) \times \vec{r}_r \tag{218}$$

Note that in the transformed frame, the stator wall appears to move backwards. The rotor wall, which describes a whirl in the absolute frame, has been reduced to a spinning wall such that the modified spin speed is the difference between the rotor

spin and whirl speeds. This corroborates our assertion that in the rotating frame the grid deformations are removed and the problems can be treated as quasi-steady.

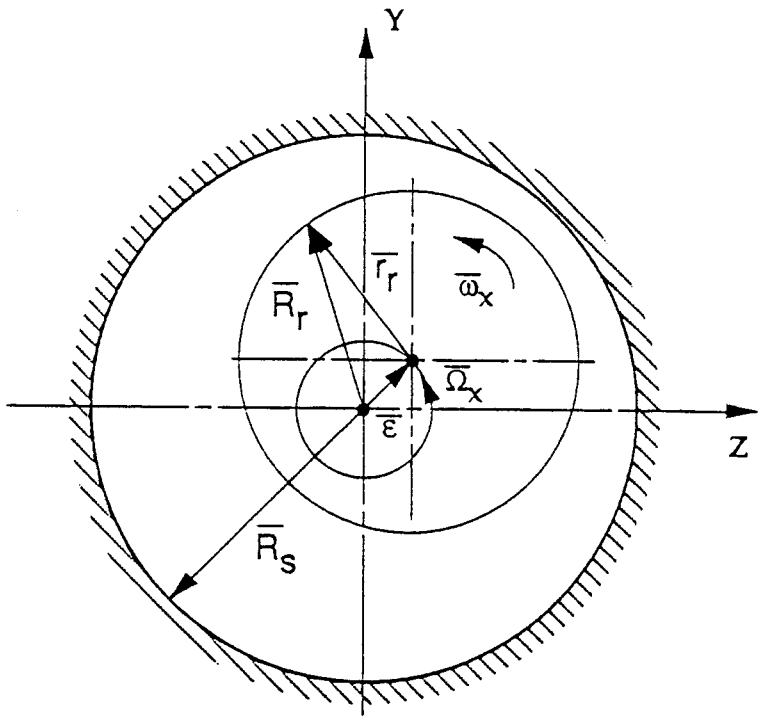


Figure 17. Definitions of the Rotor Spin and Whirl Velocities as well as Radius Vectors for Wall Velocity Transformation. Note that all Definitions are in the absolute Reference Frame.

Interpretation of the results obtained using this frame must be done with care. With the transformation the eccentric rotor looks similar to a bearing, and there is a tendency to explain the flow in terms of the rotor and stator wall absolute velocities. This procedure will lead to unphysical interpretations. The proper way to analyze this flow is either to treat it as a time-dependent flow (absolute reference frame) or use the transformed plane, with proper transformations to the wall velocities, where the stator wall has a motion.

## 4.0 SAMPLE AND VALIDATION PROBLEMS

A large number of flow problems have been simulated with SCISEAL and the results compared with benchmark analytical/experimental/numerical date to assess and validate the accuracy of the numerical and physical models incorporated in the code. A partial list of the problems is given below. Following the list, descriptions of several relevant problems and selected results are given. The first several problems in the list are checkout type 2D problems and hence details are omitted. All seal-related and other relevant problems are described.

### 4.1 Problem Titles

1. Fully-developed flow in a pipe and channel.
2. Developing laminar flow in a narrow annulus between two cylinders. Slug flow at inlet, fully-developed flow at outlet.
3. Laminar flow between rotating cylinders. Below critical Taylor number, tangential flow only.
4. Flow between two cylinders, rotating inner cylinder. Taylor vortex flow, Laminar and turbulent[23].
5. 2-D driven cavity flow, Reynolds number up to 10,000. Comparisons with numerical results by Ghia *et.al.*[24].
6. Couette flow under different pressure gradients. With and without heat transfer.
7. Planar wedge flow in a slider bearing.
8. Laminar flow over a back step. Reattachment length comparison with experiments by Armaly and Durst[25].
9. Shock reflection over a flat plate.
10. Turbulent flow in a plane channel. Fully-developed solution at exit compared with experiments by Laufer[26].
11. Turbulent flow induced by rotating disk in a cavity. Comparison with experiments by Daily and Nece[27].
12. Centripetal flow in a stator-rotor configuration. Comparison with experiments by Dibelius *et.al.*[28].
13. Flow between stator and whirling rotor of a seal. 2-D results for 0, 0.5, and

synchronous whirl frequencies.

14. Flow over a bank of tubes.
15. Turbulent flow in an annular seal. Comparison with experiments by Morrison *et.al.*[29].
16. Turbulent flow in a 7-cavity labyrinth seal. Comparison with experiments by Morrison *et.al.*[30].
17. Turbulent compressible flow and heat transfer in turbine disk cavities[31].
18. Laminar flow in a square duct with a 90° bend. Comparison with experimental data by Taylor *et.al.*[32].
19. 3-D driven cavity flow with lid clearance and axial pressure gradient. Control of flow through vortex imposition[33].
20. Flow in cavities on a rotor for an electrical motor. Interaction of Taylor vortices with driven cavity flow.
21. Flow in infinite and finite length bearings (without cavitation) Comparison of calculated attitude angles with theory[34,35].
22. Flow and rotordynamic coefficient calculation for straight, incompressible seals. Comparison with results from other numerical and analytical solutions[36].
23. Flow and rotordynamic coefficients in tapered compressible flow seals. Comparison with bulk-flow theory results[37].
24. Rotordynamic Coefficients in a long annular incompressible flow seal. Comparison with experimental data[38].
25. Calculation of entrance loss coefficients in the entrance region of a generic seal. Effect of flow and geometry on the loss coefficient values[39].
26. Flow coefficient and pressures in a 5 cavity, straight knife, look-through labyrinth seal. Comparison with experimental data[40].
27. Flow coefficients and pressures in a 2 cavity, tapered knife, look-through labyrinth seal. Comparison with experimental data[41,42].
28. Flow coefficients and pressures in a 2 cavity, straight-knife, stepped labyrinth seal. Comparison with experimental data[41,42].
29. Computations of the rotordynamic coefficients for an eccentric annular seal with incompressible flow[43].
30. Flow solutions in a whirling annular seal[44] and comparison with experiments.[45-47]

31. Numerical solutions of flow and cooling effectiveness in rim seals and disc cavities[48] and comparison with experiments.[49]
32. Interaction of mainpath-secondary flow in multiply connected turbine[50] disc cavities and comparison with experimental data.[51]
33. Flow and conjugate heat transfer simulations in turbine disc cavities.[52]

## 4.2 Problem Description and Sample Results

Following are the descriptions and SCISEAL results and comparisons with other date/results where applicable. The number associated with each of the problems refers to it's position in the list given above.

### 11. Turbulent Flow Induced by Rotating Disk in a Cavity

Problem specification

- Calculation of the flow induced by a rotating disk in an enclosed cavity.

Benchmark data

- Experimental measurements from Daily and Nece[27].

Grid

- 40 cells in the axial direction, 60 cells in the radial direction with clustering near the walls.

Boundary conditions

- Specified angular velocity for the rotor walls.
- Wall conditions for all other boundaries.

Numerics and physical models

- Central differencing with 0.05 damping.
- Standard k-ε model with wall functions.

Results

- Flow geometry as shown in Figure 18a.
- Normalized radial and tangential velocities at a given radius are shown in Figures 18b and 18c. Also shown in the figures are the experimental data from Daily and Nece[27].

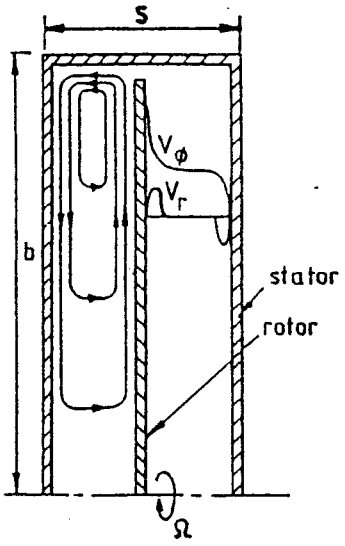


(a) Flow Geometry

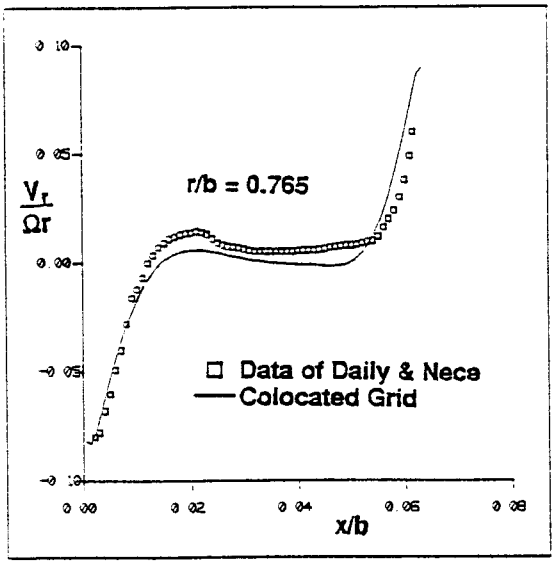


(b) Radial Velocity

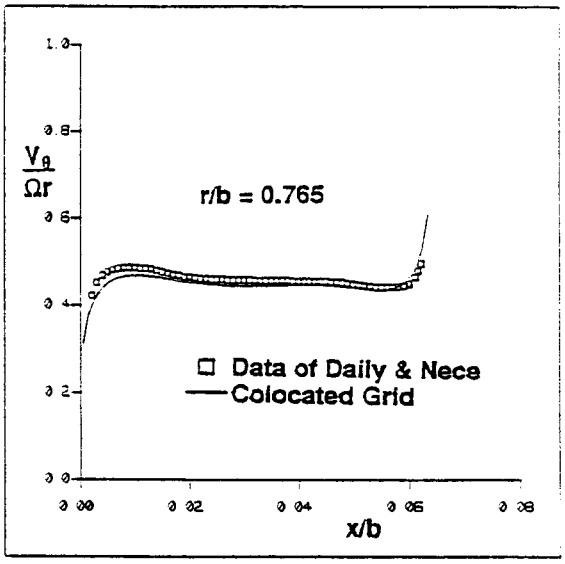


(c) Tangential Velocity

Figure 18. Turbulent Flow Due to a Rotor in an Enclosed Cavity. Experimental Data from Daily and Nece[27]

## 15. Annular Seal Flow

Problem specification

- Calculation of turbulent flow in an annular seal.

Experimental data

- Experimental data by Morrison, *et al.*[29].

Grid

- 25 cells in the radial direction, 58 cells in the axial direction; cells in radial direction clustered near the walls.

Boundary conditions

- Experimental profiles of the velocities and turbulence quantities at inlet boundary.
- Specified pressure at the outflow boundary.
- Wall condition with specified angular speed at rotor wall.
- Stationary wall conditions at stator wall.

Numerics and physical models

- Central differencing with 0.01 damping.
- Standard two equation k-ε model for turbulence.

Results

- Geometry of the rotor is shown in Figure 19a, and the experimental setup is shown in Figure 19b.
- Computed and experimental contours of the axial, azimuthal and radial velocities are shown in Figures 20, 21 and 22, respectively.
- Figure 23 shows the computed turbulent kinetic energy profiles.

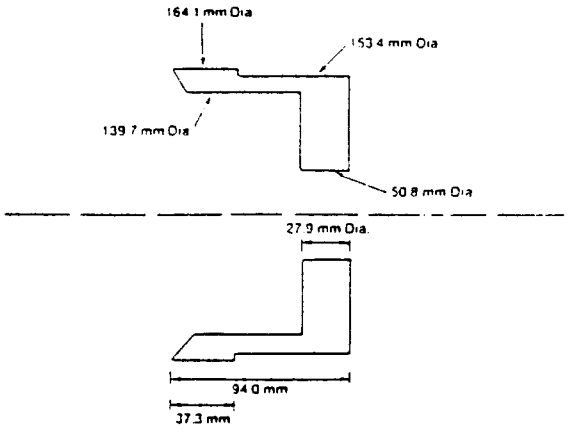


(a) Geometry of Annular Rotor

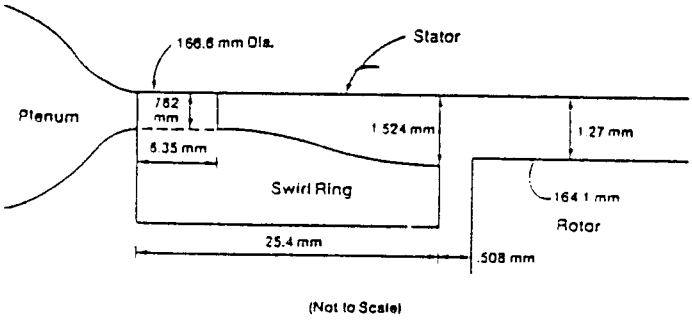


(b) Annular Seal Inlet Geometry

Figure 19. Flow Details for the Annular Seal. Reynolds number based on the gap = 27000, Taylor number = 6600, shaft speed = 3600 rpm

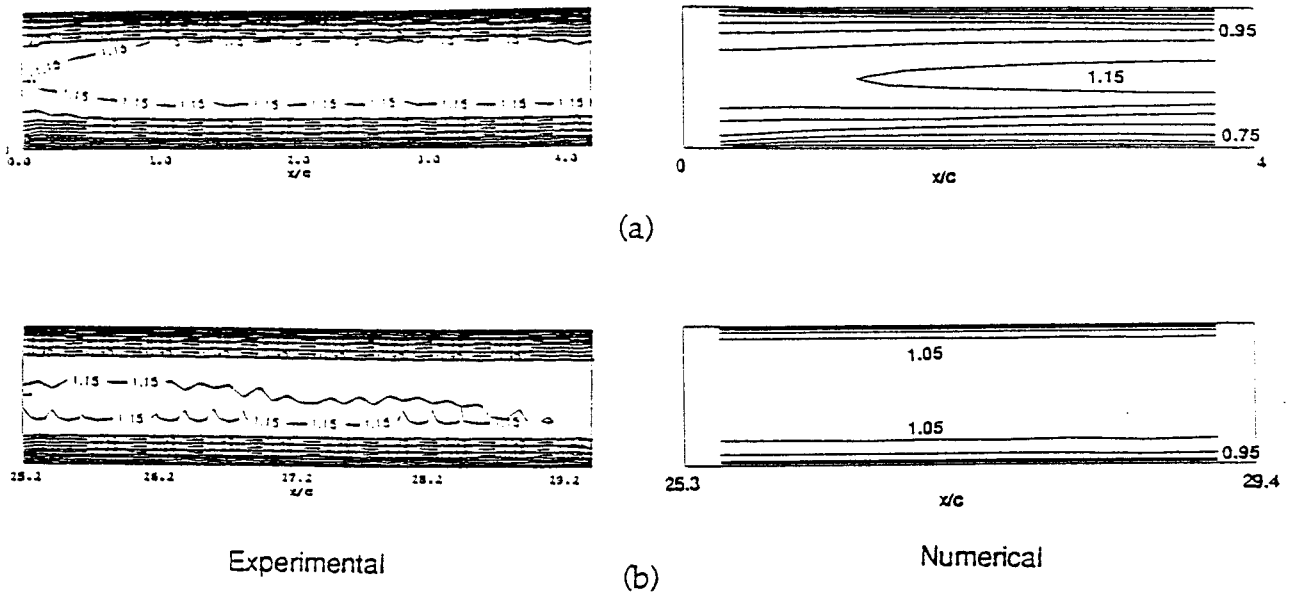


Figure 20. Annular Seal Flow. Contours of the scaled axial velocity $u_x/u$. (a) near inlet ($0 < x/c < 4$), (b) near outlet ($25 < x/c < 29.4$)

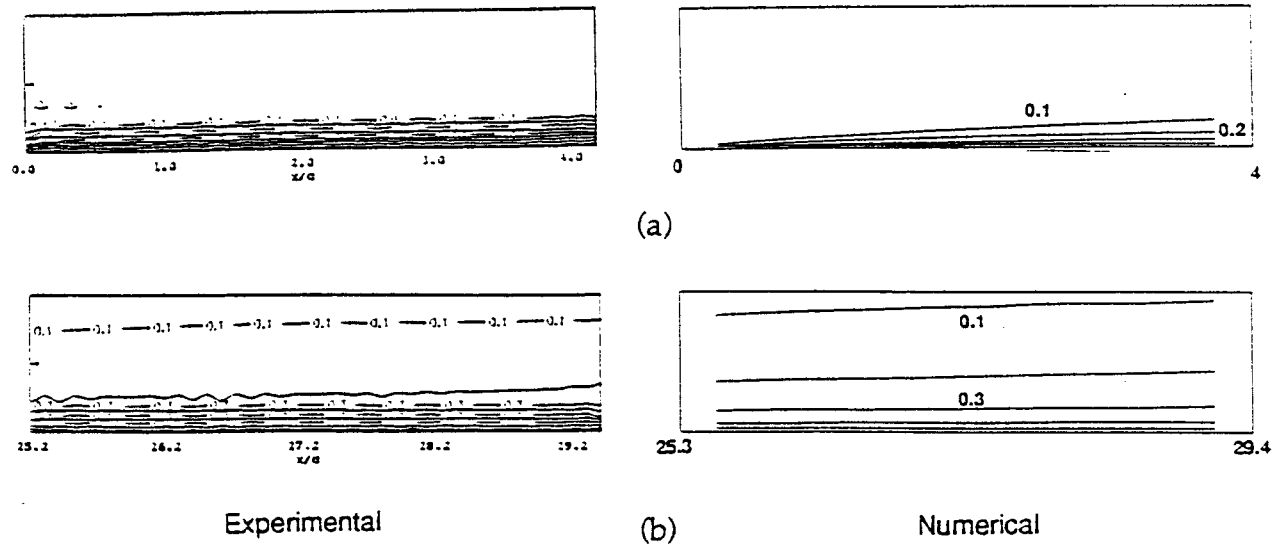


Figure 21. Annular Seal Flow. Contours of the scaled azimuthal velocity, $u_\theta/w_{shaft}$ (a) near inlet ($0 < x/c < 4$), (b) near outlet ($25 < x/c < 29.4$)

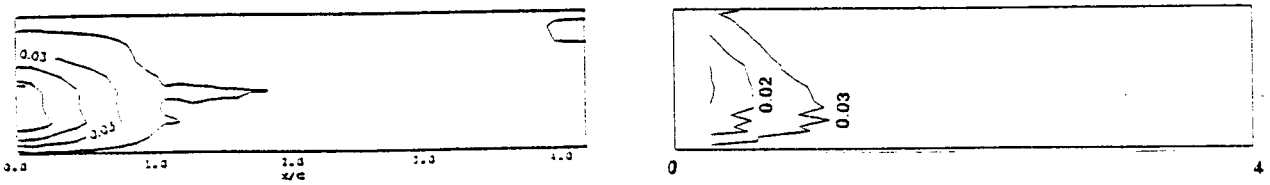


Experimental Numerical

Figure 22. Annular Seal Flow. Contours of the scaled radial velocity $u_r/u$. Near inlet details ($0 < x/c < 4$)

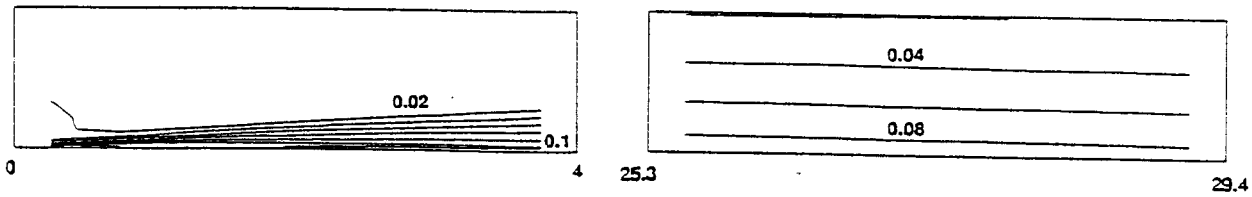


(a) (b)

Figure 23. Annular Seal Flow. Contours of the scaled turbulent kinetic energy, $\frac{1}{2}\left(u_r'^2 + u_\theta'^2 + u_x'^2\right)/U^2$. Numerical results, (a) near inlet ($0 < x/c < 4$), (b) near outlet ($25 < x/c < 29.4$).

## 16. Seven Cavity Labyrinth Seal

Problem specification

- Calculation of turbulent flow in a seven-cavity labyrinth seal.

Experimental data

- Experimental data by Morrison, *et al.*[30].

Grid

- 30 cells in the axial and radial directions per cavity.
- 10 cells in the radial clearance between the rotor tooth and the stator.
- Stretching used to cluster the grid near the rotor and stator walls.

Boundary conditions

- Experimental profiles for velocities and turbulence quantities at inlet boundary.
- Specified pressure at outflow boundary.
- Wall condition with specified angular velocity at rotor walls.
- Wall conditions at stator wall.

Numerics and physical models

- Central differencing with 0.01 damping.
- Standard two equation k-ε model for turbulence.

Results

- Details of the rotor are shown in Figure 24a, and the experimental setup is shown in Figure 24b.
- Computed and numerical velocity vector plots are shown in Figure 25.
- Computed and experimental contours of the axial, radial and tangential velocities are shown in Figures 26, 27 and 28, respectively.
- Figure 29 shows computed contours of the turbulent kinetic energy.

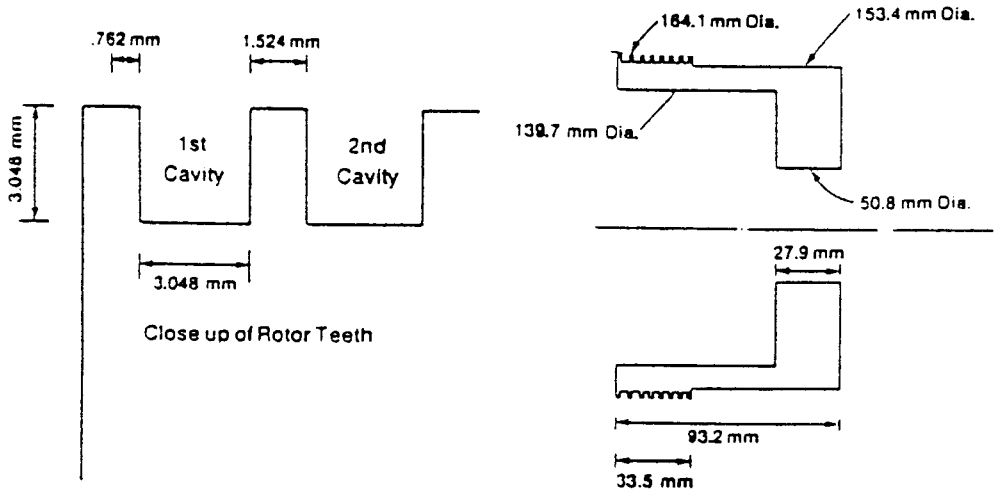


(a) Details of the Labyrinth Rotor

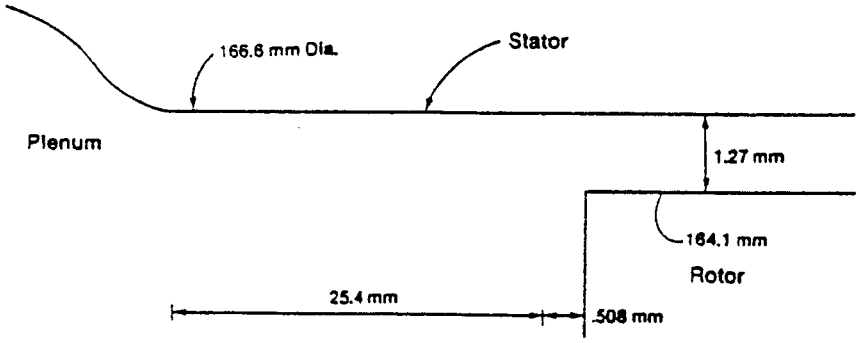


(b) Seal Inlet Geometry

Figure 24. Seven Cavity Labyrinth Seal Flow. Reynolds number based on the clearance = 28000, taylor number = 7000, shaft speed = 3600 rpm.

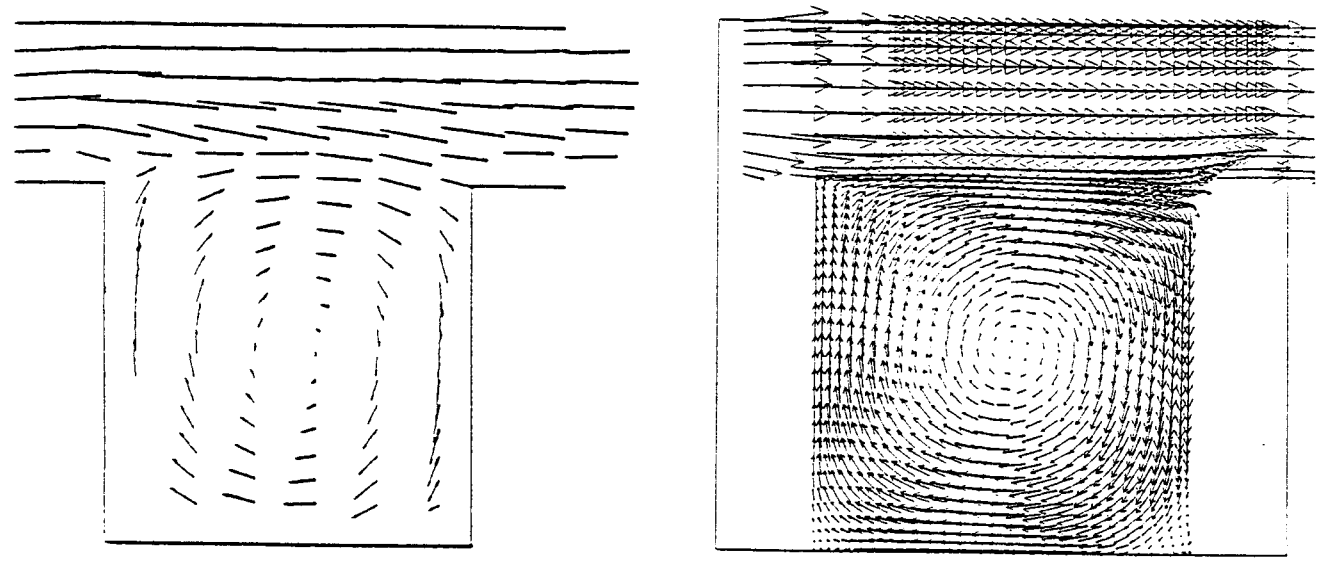

First Cavity

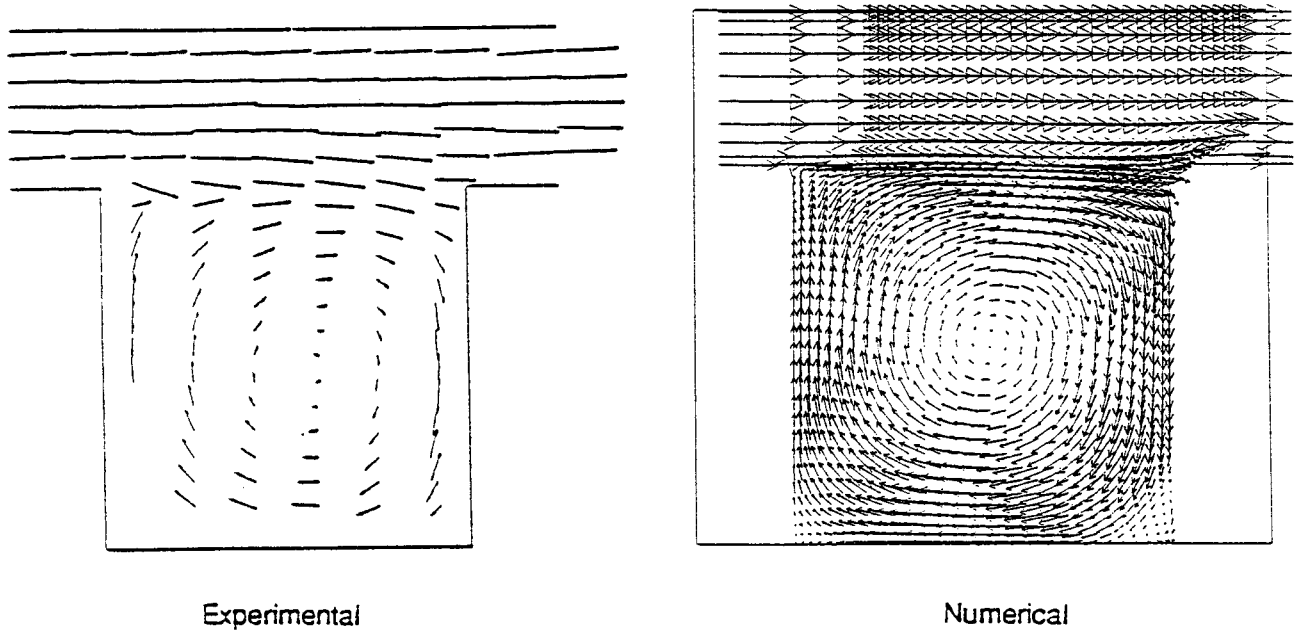


Third Cavity

Figure 25. Seven Cavity Labyrinth Seal. Velocity vector plot.

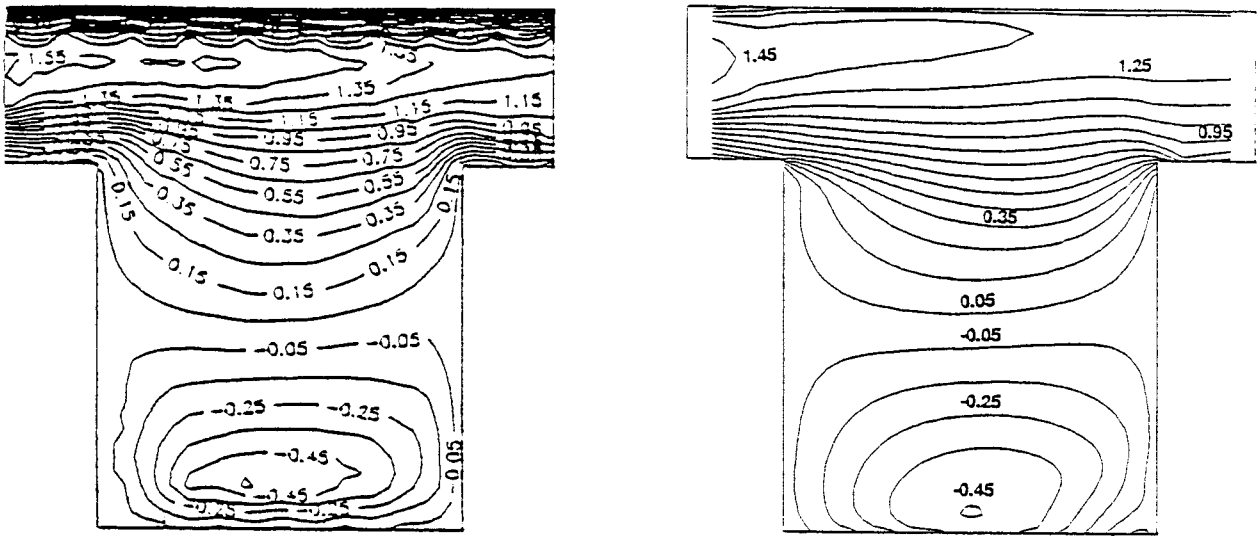


First Cavity

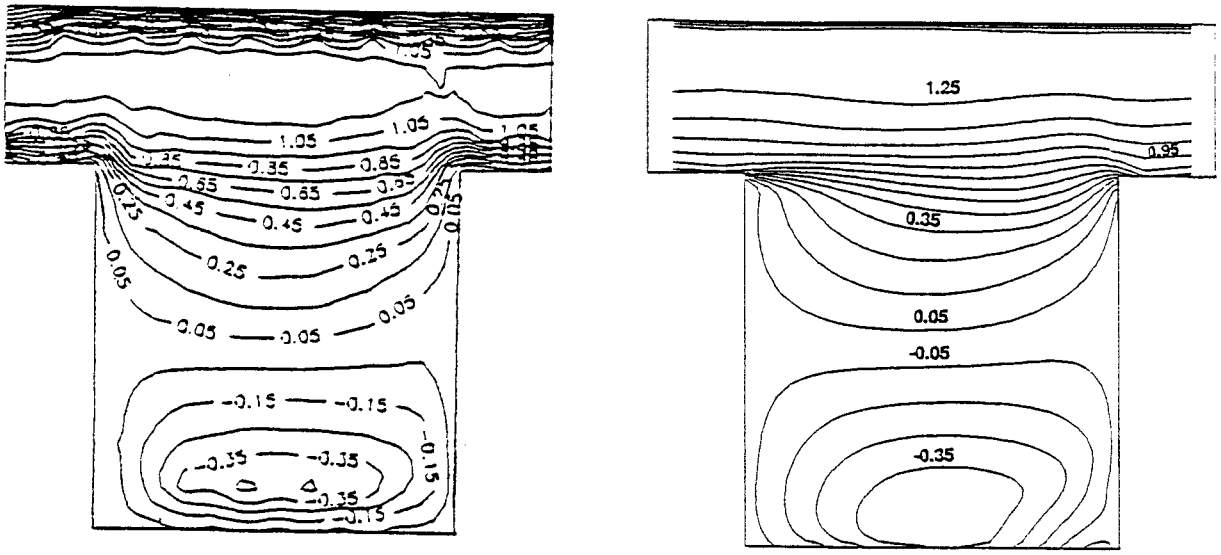


Experimental

Numerical

Third Cavity

Figure 26. Seven Cavity Labyrinth Seal. Contours of scaled axial velocity, $u_x/U$.

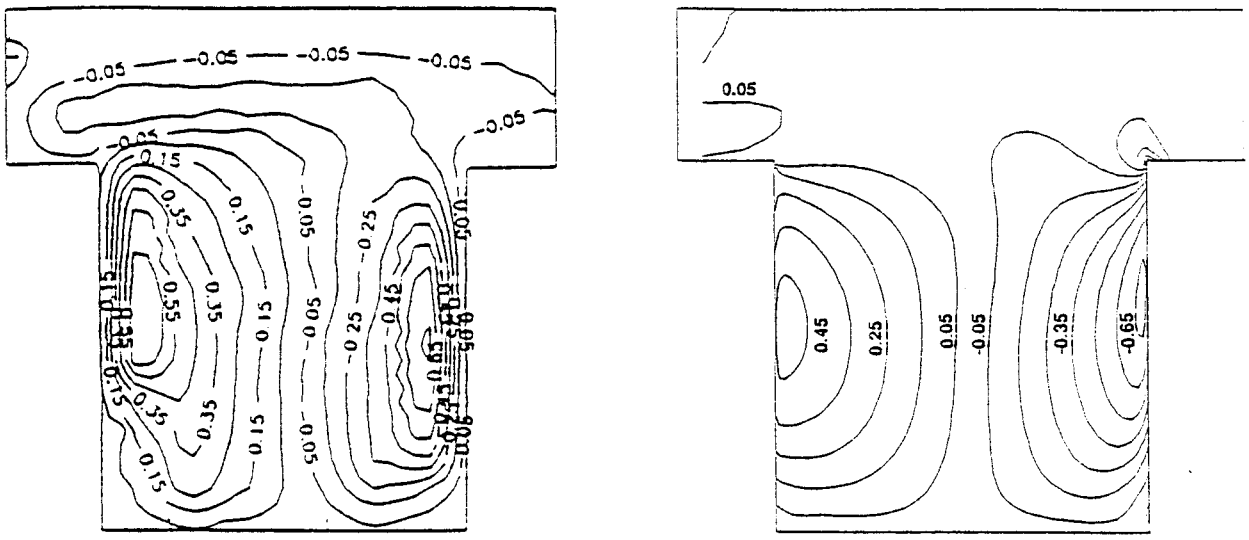


First Cavity

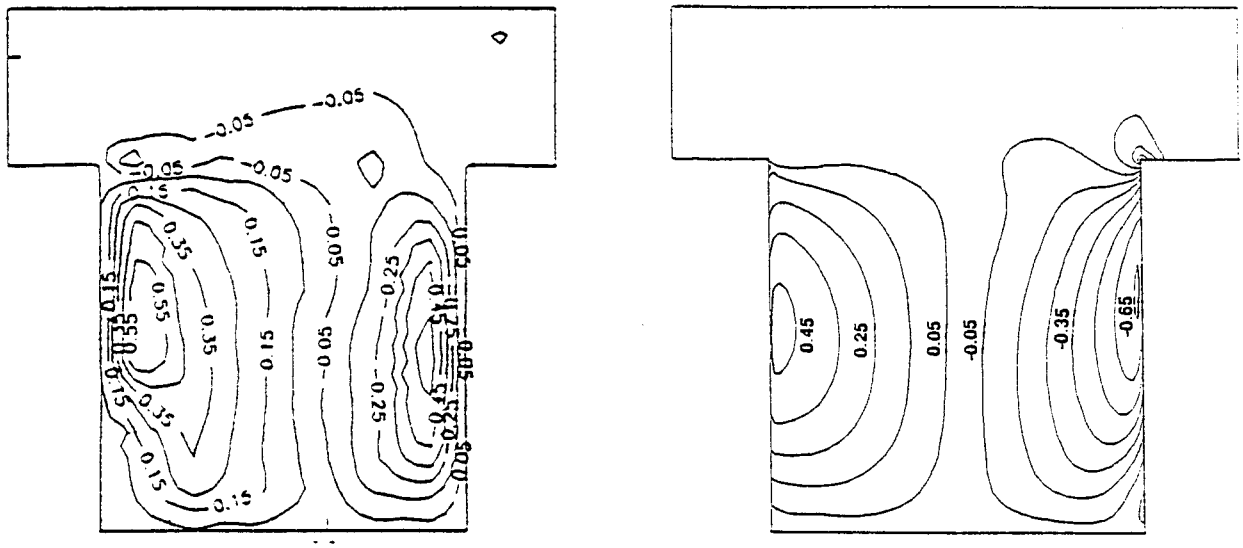


Experimental

Numerical

Third Cavity

Figure 27. Seven Cavity Labyrinth Seal. Contours of scaled radial velocity, $u_r/u$.

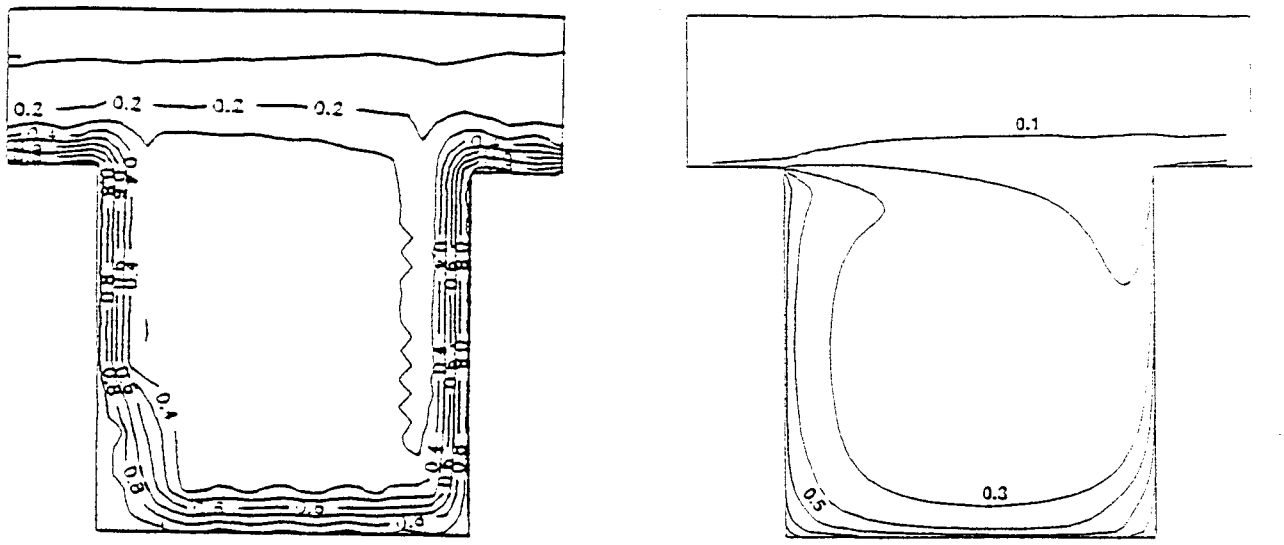


First Cavity

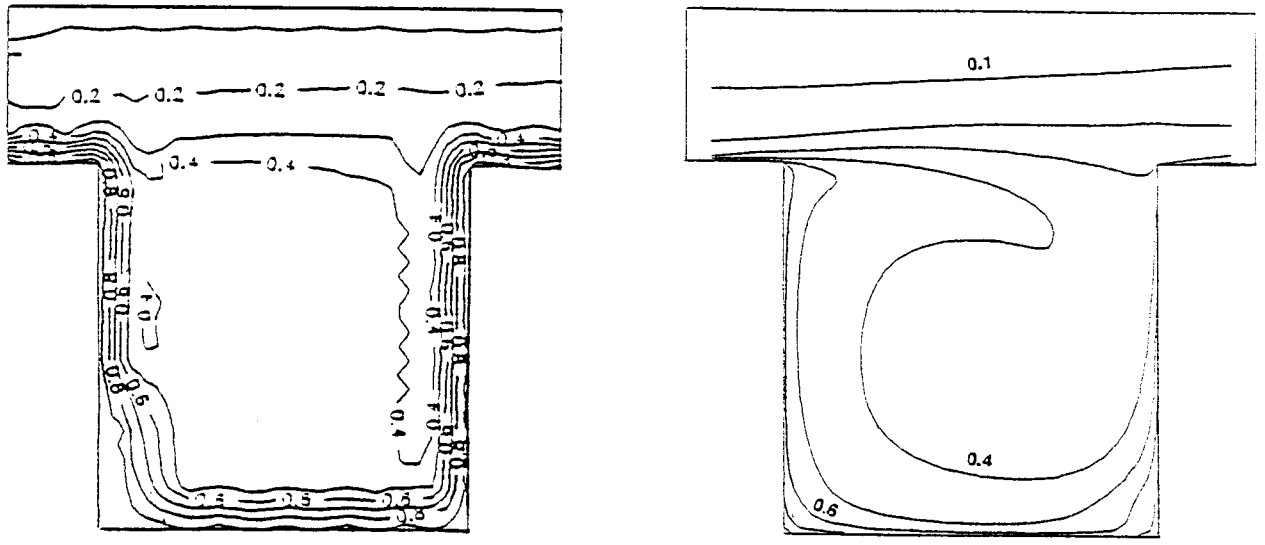


Experimental

Numerical

Third Cavity

Figure 28. Seven Cavity Labyrinth Seal. Contours of scaled azimuthal velocities, $u_\theta / w_{shaft}$.

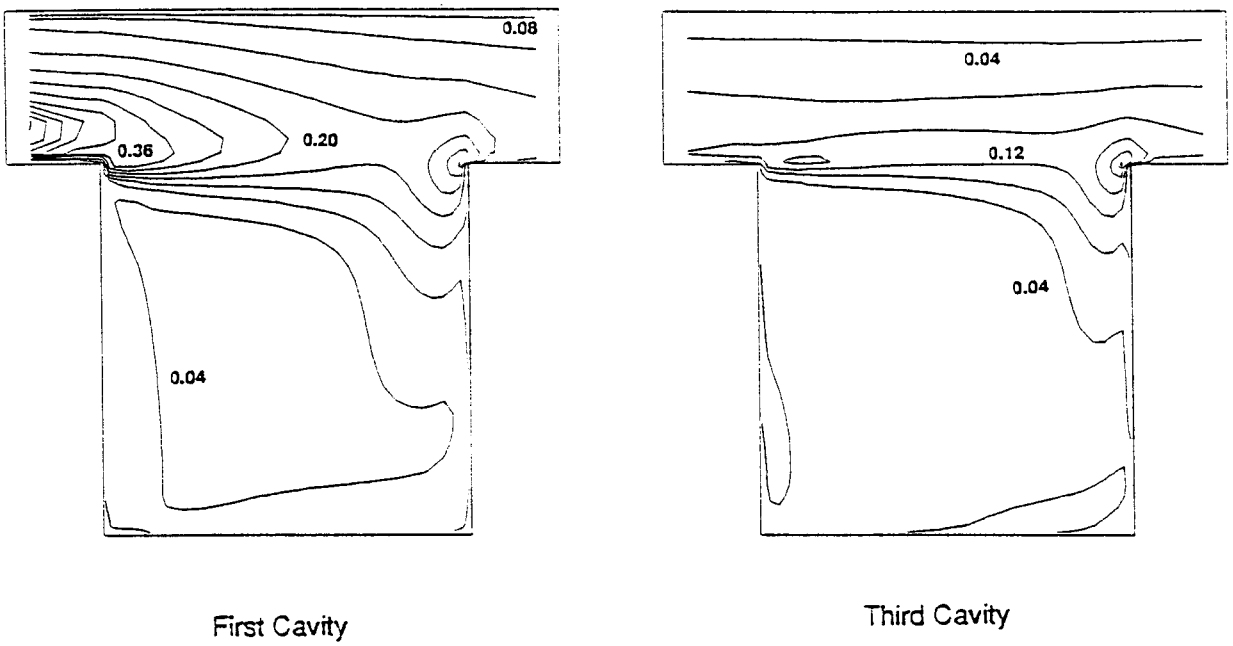


Figure 29. Seven Cavity Labyrinth Seal Flow. Contours of normalized turbulent kinetic energy $\frac{1}{2}\left(u_r'^2 + u_\theta'^2 + u_x'^2\right)/U^2$. Numerical results.

## 17. Turbulent Compressible Flow in Turbine Disk Cavities

Problem Specification

Computation of the turbulent compressible flow is representative turbine disk cavities, under the effect of secondary cooling flows. The effect of varying cooling flow rates and geometry changes are assessed.

Geometry, Grid, Physical Models and Results

Please refer to Reference 31 for detailed description of the problem and results.

## 19. 3-D Driven Cavity Flow with Lid Clearance and Axial Pressure Gradient

### Problem Specification

To compute the interaction of the tip vortex and the core flow in a turbine blade passage. The problem is simulated using a driven cavity flow with lid clearance and axial pressure gradient. Effects of a vortex imposed upstream of the flow are assessed for vortex strength, sense and location.

### Grid, Geometry, Physical Models and Results

Please refer to Reference 31 for a detailed description of the problem and results.

## 20. Flow in Cavities on a Rotor in an Electrical Motor

Problem Specification

Computation of the flow in the channels present in an electrical motor, to assess the flow structure, generation of Taylor vortices and their interaction with the flow in the channels.

Grid, Geometry, Physical Models and Results

Please refer to Reference 33 for a detailed description of the problem and results.

## 21. Flow in Infinite and Finite Length Journal Bearings

Problem Specification

Computation of flow in A) an infinite length bearing, and B) finite length bearing without cavitation.

Benchmark Data

Analytical results for the bearing attitude angle as given in Fuller[34], (infinite length) and Cameron[35] (finite length).

Grid

A. Infinite length case
   - Rotor radius = 36 mm, nominal clearance = 0.036 mm.
   - 40 cells along the circumference, 10 cells in the radial direction, 3 cells in the axial direction.

B. Finite length case
   - Rotor radius = 36 mm, nominal clearance = 0.036 mm, axial length = 36 mm (L/D = 0.5).
   - 10 cells in the axial direction, 40 along the circumference, 10 cells in the radial direction.

Boundary Conditions

Case A.
- Symmetry conditions on boundaries in axial direction,
- Rotating wall on rotor, (speed = 5,000 rpm), stationery wall on stator.

Case B.
- Specified ambient pressure on both boundaries in axial direction,
- Rotating wall on rotor, (speed = 5,000 rpm), stationery wall on stator.

Physical models

- Laminar, incompressible flow.
- Central differencing with 0.1 damping.

Results

- Results for bearing eccentricities from 0.1 to 0.95 obtained for both cases A and B.
- Half Sommerfeld conditions used to calculate rotor pressure forces and the resulting attitude angles. Attitude angles compared with analytical results.
- Figure 30 shows attitude angles for Case A, together with analytical results from Fuller.[34] Figure 31 shows results for Case B, with analytical results from Cameron[35], very good/excellent agreement seen in both cases.

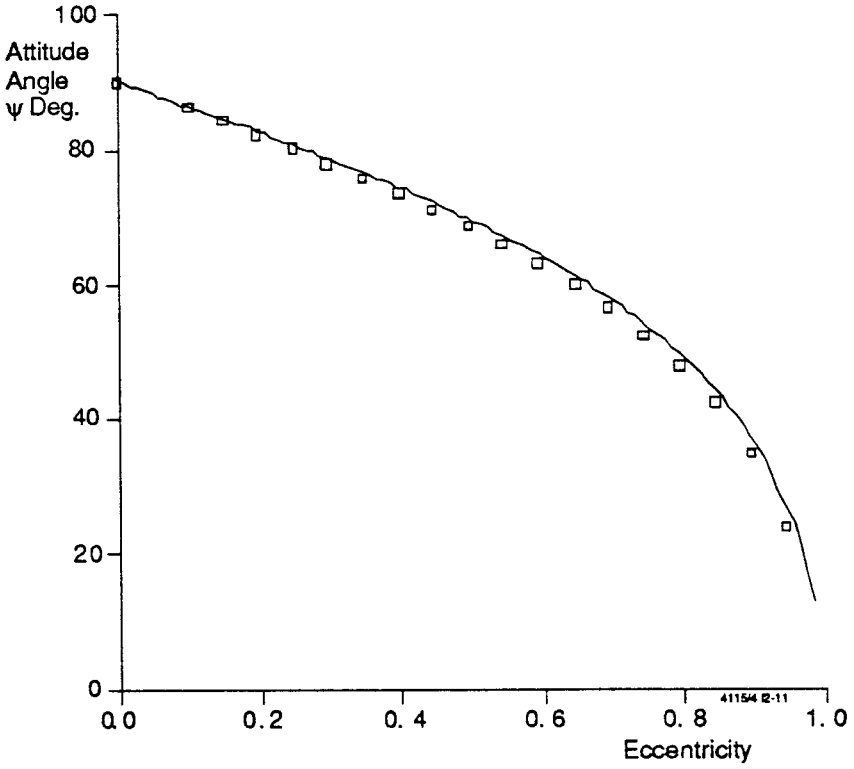


Figure 30. Attitude Angles for Case A, Long Bearing

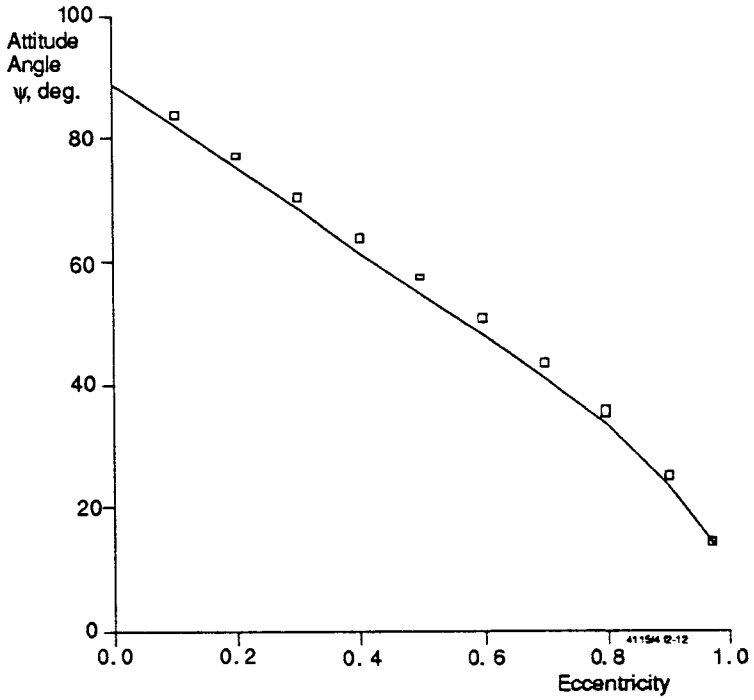


Figure 31. Results for Case B, Short Bearing

## 22. Rotordynamic Coefficients for Incompressible Annular Seal

Problem Specification

Computation of the rotordynamic coefficients for a short annular grid with incompressible flow.

Experimental Data

Experimental and numerical data from Dietzen and Nordmann.[36]

Grid

- Seal radius = 23.5 mm, seal clearance = 0.2 mm, seal length = 25 mm.
- 10 cells in axial direction, 30 in circumference direction and 5 or 12 in seal gap depending on the turbulence model used.

Boundary Conditions

- Specified upstream/downstream pressure differential with entrance loss coefficient = 0.5.
- Stationary wall on stator, rotating wall on rotor, rotor speed varied from 1000-5000 rpm.

Physical Models

- Central-differencing with 0.1 damping.
- Data obtained with standard k-ε model with wall functions and the 2-layer model for turbulence.
- Whirling rotor, numerical shaker and perturbation model tried for rotordynamic coefficients.

Results

- Rotordynamic coefficients calculated at several rotor speeds.
- Numerical results for whirling rotor method shown here. These results match very well with results from the numerical shaker method and perturbation method.
- Figures 32 and 33 show the direct and cross-coupled stiffness coefficients. Figures 34 and 35 show the direct and cross-coupled damping coefficients and Figure 36 shows the direct inertia coefficient. Also shown are results from experiments, finite difference methods and bulk-flow theory. Very good agreement is observed in the present results and other published results.

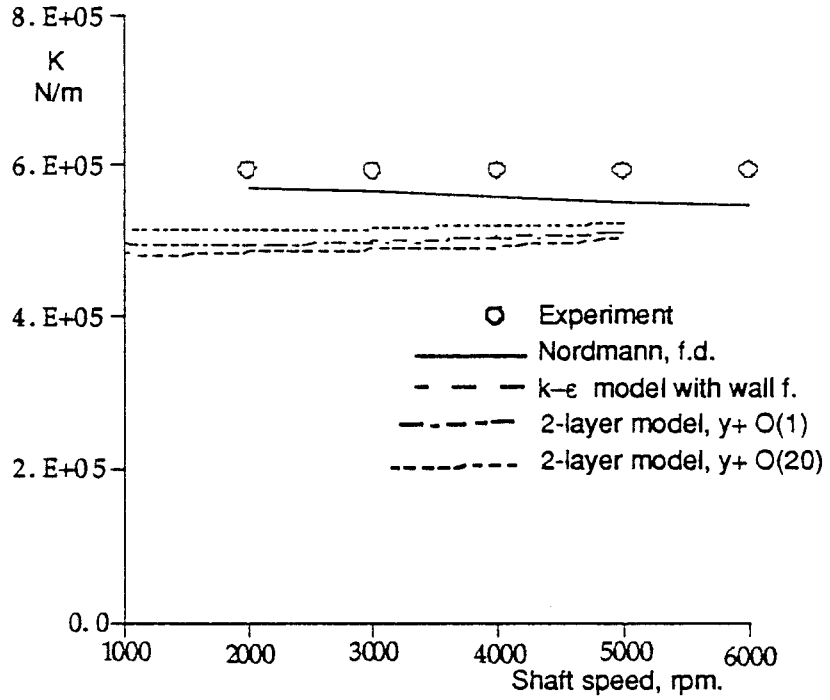


Figure 32. Direct Stiffness Coefficient, Annular Seal

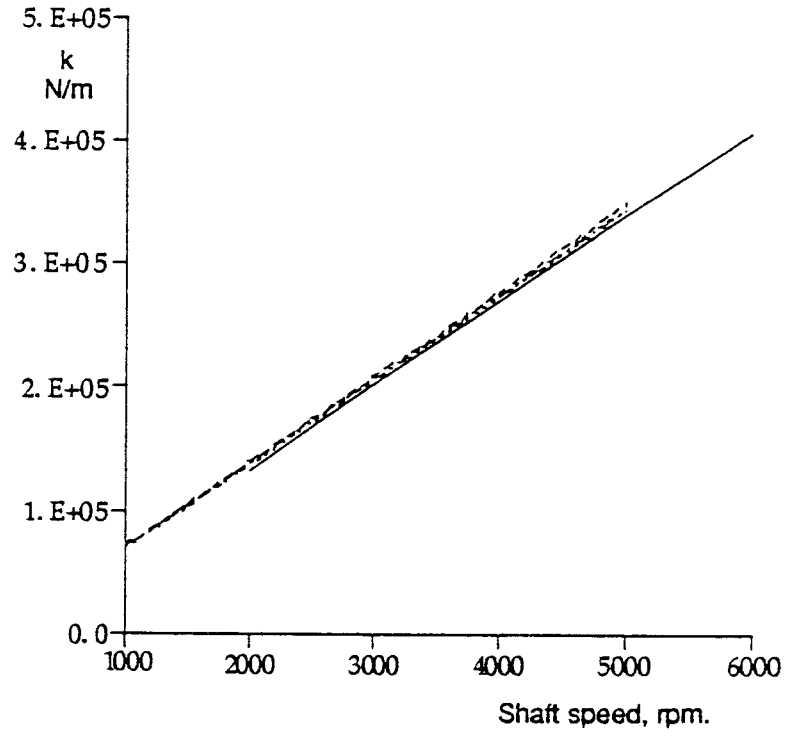


Figure 33. Cross Coupled Stiffing Coefficient, Annular Seal

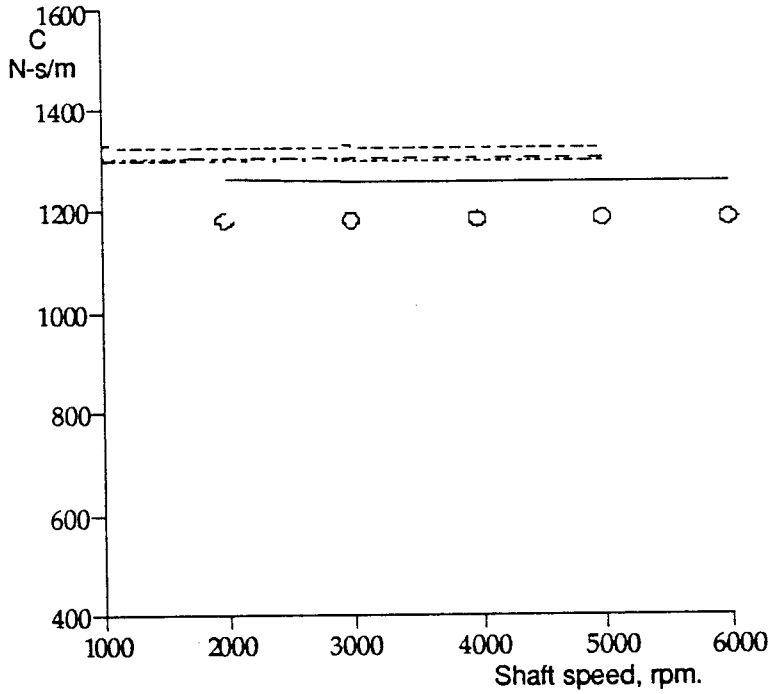


Figure 34. Direct Damping Coefficient, Annular Seal

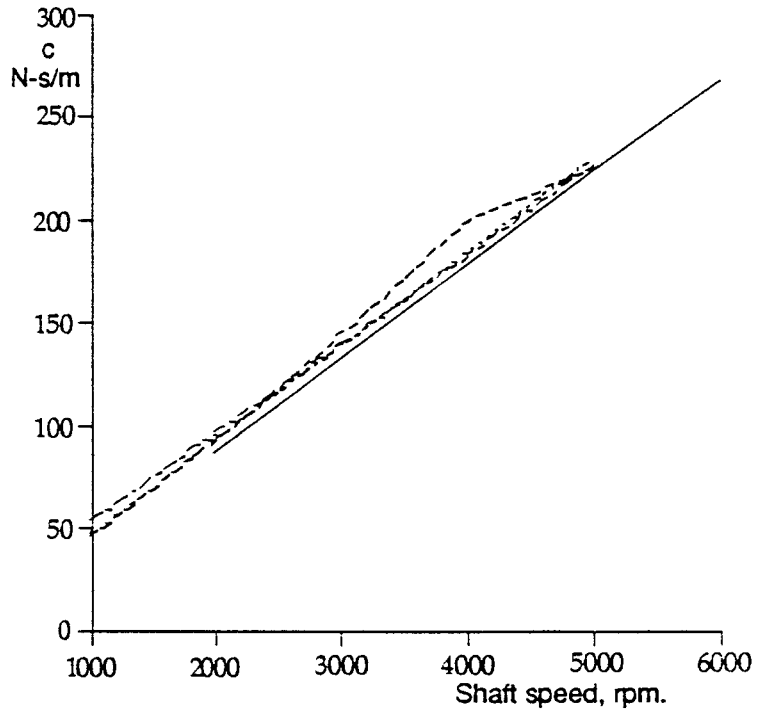


Figure 35. Cross Coupled Damping Coefficient, Annular Seal

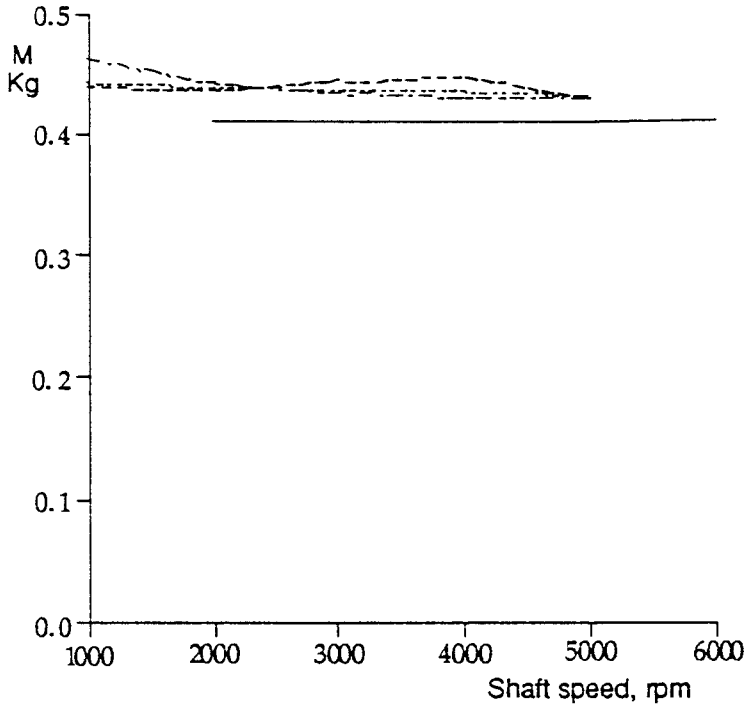


Figure 36. Direct Mass Coefficient, Annular Seal

## 23. Rotordynamic Coefficients for Tapered Seal with Compressible Flow

Problem Description

Computation of compressible flow and the rotordynamic coefficients for a tapered annular seal.

Data

Bulk flow theory results by Nelson.[37]

Grid

- Seal radius = 32.5 mm, inlet and exit clearance = 0.172 and 0.086 mm L/D ratio varied from 0.1 to 0.4.
- 12 cells in axial, 6 cells in radial and 30 cells in circumferential direction.

Boundary Conditions

- Upstream pressure = 1.52 MPa, exit pressure = 0.65 MPa, $\gamma = 1.4$.
- Upstream Temperature = 650k and entrant loss factor $\xi$ as given in Reference 37.
- Rotating wall on rotor stationery wall on stator, shaft speed = 30,400 rpm.

Physical Models

- Central differencing with 0.1 damping.
- Standard k-ε model with wall functions.
- "Numerical Shaker" method for rotordynamic coefficient calculations.

Results

- Results obtained at L/D = 0.1, 0.2 and 0.4.
- Results shown in Table 2.1 together with bulk flow theory results from Nelson[37] and good agreement between the two sets is seen.

Table 2. Tapered Gas Seal Rotordynamic Coefficients

| L/D | K N/m | k N/m | C N-s/m | c N-s/m | Exit Mach Number |
|---|---|---|---|---|---|
| 0.1 | 948000 | 19700 | 11.5 | 0.016 | 1.00 |
| | 1150000 | 15429 | 9.94 | 0.043 | 1.00 |
| 0.2 | 1700000 | 75700 | 43.9 | 0.073 | 0.96 |
| | 2125500 | 60886 | 38.62 | 0.09 | 0.97 |
| 0.4 | 2880000 | 267000 | 152.0 | 0.27 | 0.83 |
| | 3553200 | 233820 | 145.9 | 0.57 | 0.83 |

Nelson, 1985[37]  Present Results

## 24. Rotordynamic Coefficients of a Long Annular Seal

Problem Specification

Computation of rotordynamic coefficients for a long annular seal with incompressible flow.

Experimental Data

- Experimental results reported by Kanemori and Iwatsubo.[38]

Grid

- Seal radius = 39.656 mm, clearance = 0.394 mm, length = 240 mm.
- 18 cells in axial direction, 30 in circumferential direction, 16 or 18 cells in seal gap depending on the axial pressure differentials.

Boundary Conditions

- Specified upstream/downstream pressure differential ranging from 20 to 900 KPa with entrance loss factor $\xi = 0.5$.
- Rotating wall at rotor surface, stationary wall on stator; shaft speed = 600, 1080, 1980 and 3,000 rpm.

Physical Models

- Central differencing scheme with 0.1 damping.
- 2 turbulence models used (1) low-Re k-ε (ii) 2 layer.
- Problem tried with (i) whirling rotor method and (ii) small perturbation method for rotordynamics.

Results

- Similar results with both turbulence models and rotordynamics calculation methods.
- Results from low Re k-ε model and whirling rotor method reported here.
- Figures 37 and 38 show the direct and cross-coupled stiffness coefficients. Figures 39 and 40 the direct and cross-coupled damping and Figure 41 the direct inertia (mass) coefficient.
- Experimental data also plotted for comparison, very good agreement between computational and experimental[38] results.

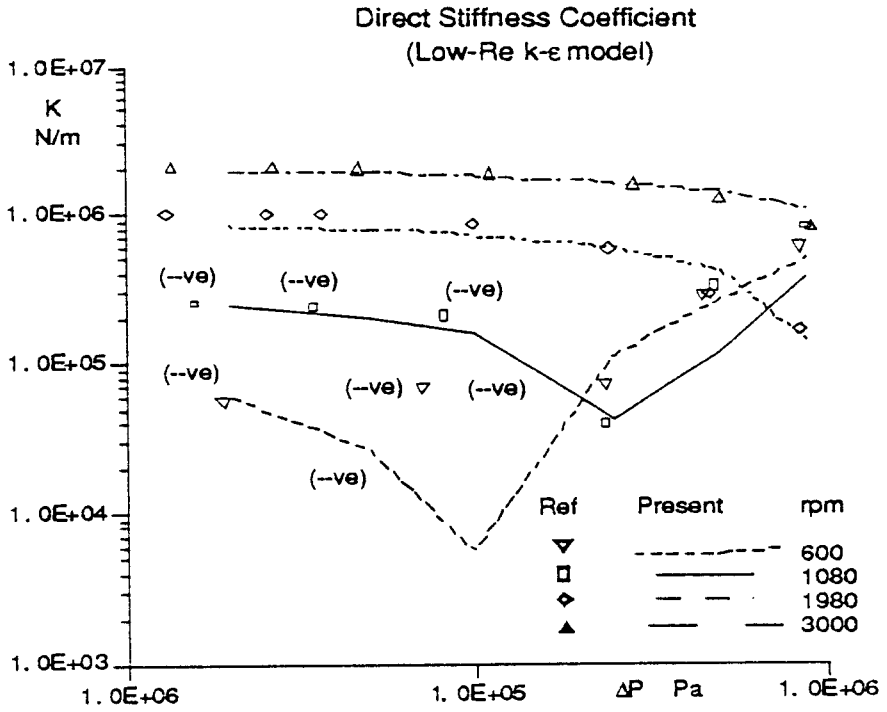


Figure 37. Direct Stiffness Coefficients, Long Annular Seal

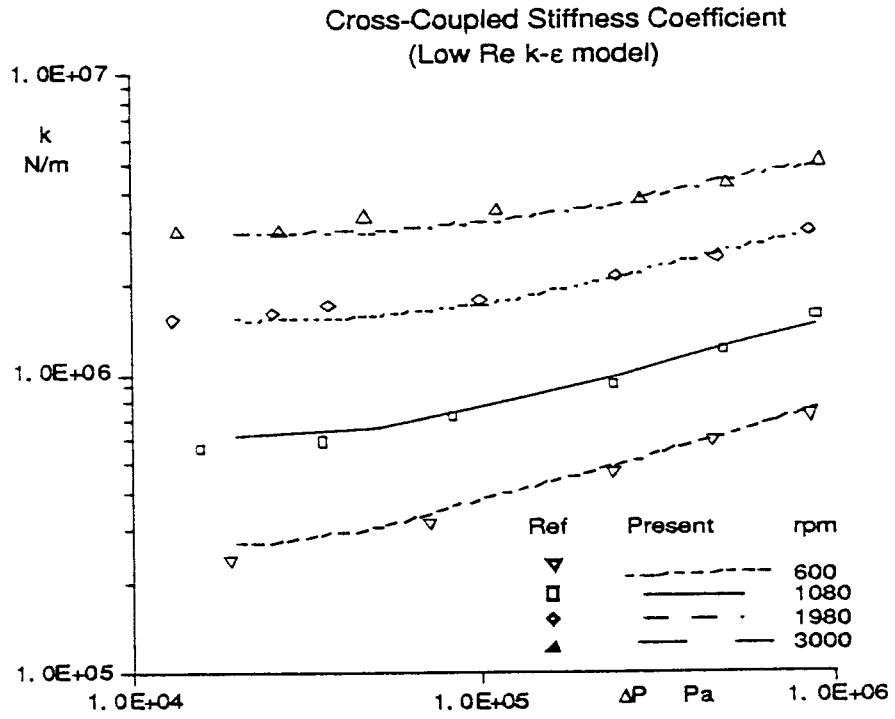


Figure 38. Cross Coupled Stiffness Coefficients, Long Annular Seal

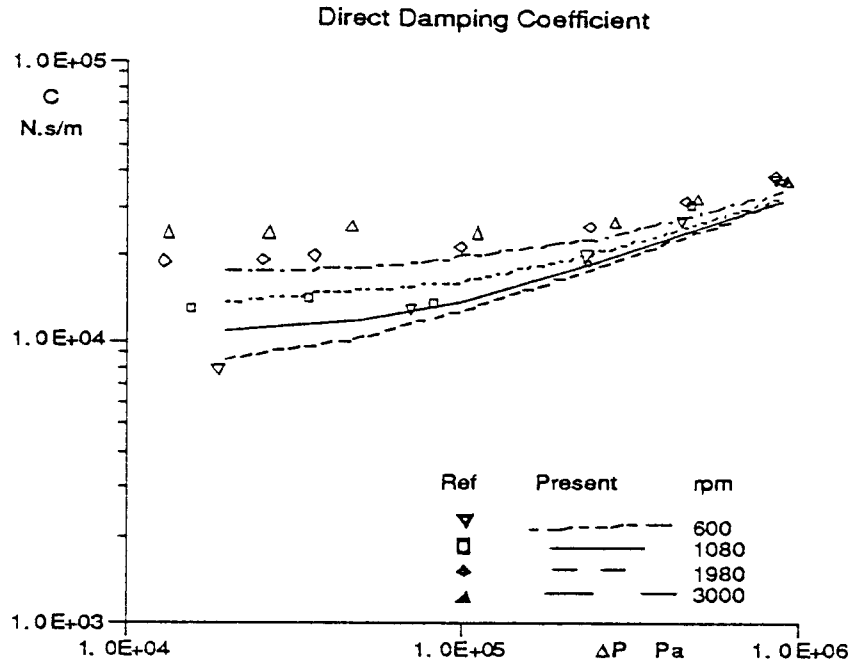


Figure 39. Direct Damping Coefficient, Long Annular Seal

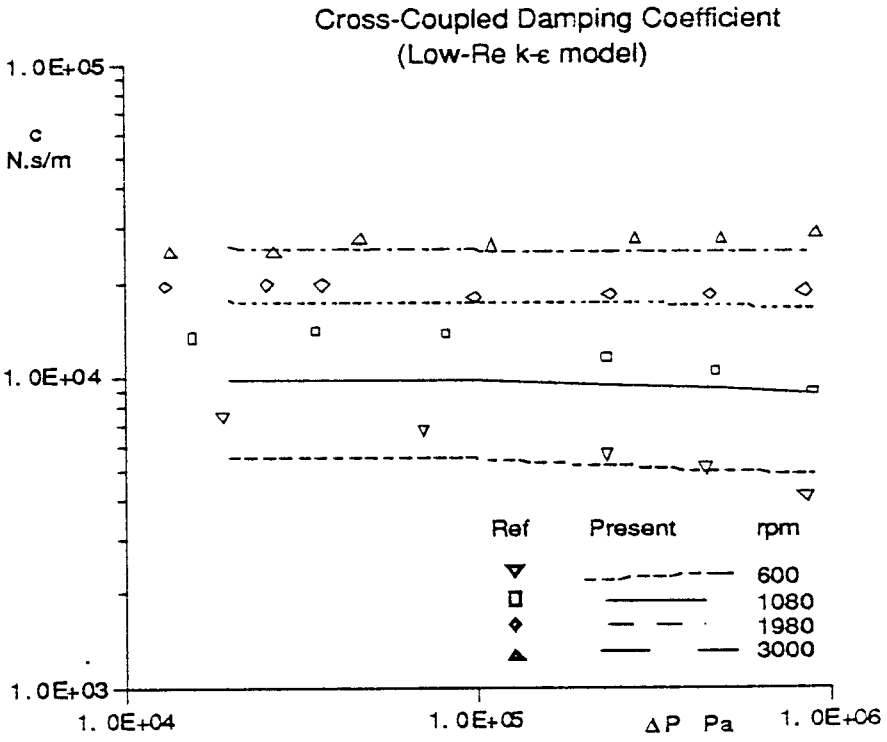


Figure 40. Cross Coupled Damping Coefficient, Long Annular Seal

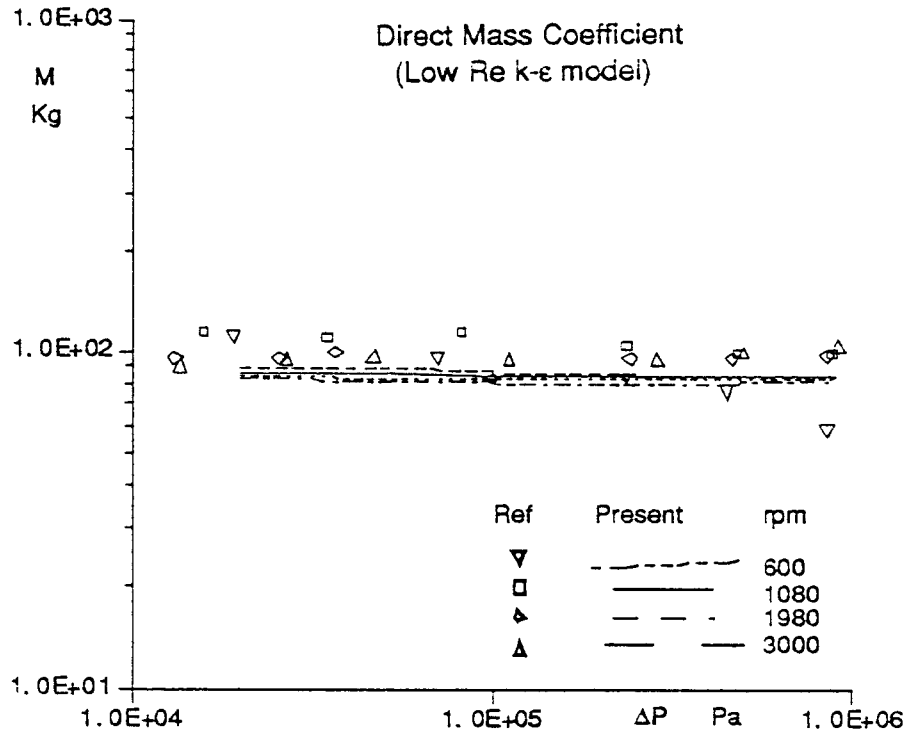


Figure 41. Direct Mass Coefficient, Long Annular Seal

## 25. Calculation of Entrance Loss Coefficients

Entrance loss factor is an empirical factor used in seal calculations to account for the flow losses as the fluid enters the narrow seal clearance from a relatively large gap in the entrance region. A generic seal entrance region is considered and several geometry and flow parameters are varied to assess their effect on the loss factor.

Problem Specification

Compute the entire loss factors for a generic seal-entrance region and assess effects of 1) rotor radius-to-clearance ratio, 2) Entrance region radial width-to-clearance ratio and 3) Flow rate on the entrance loss factor.

Grid

- Seal radius 25 mm, seal length = 25 mm, inlet region length 1.5 times the seal radius.
- 30 cells in entrance region, 20 cells in the seal in axial direction. 5 cells in the seal clearance radially, and 30 or 50 cells radially in entrance region, depending on entrance-gap-to-clearance ratio.

Boundary Conditions

- Fixed downstream pressure, fully-developed turbulent axial velocity profile at inlet of entrance region for specified mean axial velocity.
- Rotating wall on the rotor surface, stationary wall on stator.
- Inlet k & ε fully-developed profiles.

Physical Models

- Incompressible flow.
- Central-differencing with 0.1 damping.
- Standard k-ε model with wall functions.

Results

- Typical grid shown in Figure 42.
- Rotor speed at 3,000 rpm, rotational Re = 2,500 - 7,500.
- Entrance loss coefficients at different clearance-to-radius ratios, Reynolds meters and Entrance-gap-to-clearance ratios shown in

Table 3.

- Numerical results show:
  - Radius-to-clearance ratio has the highest effect ratio$\uparrow \Rightarrow \xi \uparrow$
  - Gap-to-clearance ratio $\uparrow \Rightarrow \xi \uparrow$ with lower sensitivity
  - for a fixed geometry, axial Re $\uparrow \Rightarrow \xi \downarrow$, with high sensitivity
  - $\xi$ range from 0.406 to 0.68.

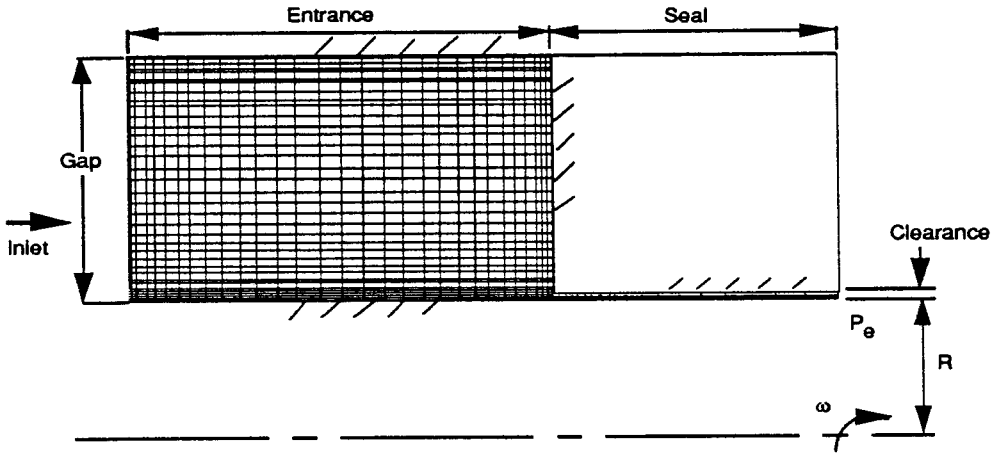


Figure 42. Flow Domain and One of the Grids Used for the Entrance Loss Coefficient Calculations

Table 3. Entrance Loss Coefficients, Radius/Clearance = 50

| Entrance Gap/Clearance = 50 | | | Entrance Gap/Clearance = 100 | | |
|---|---|---|---|---|---|
| $u_{ax}$ m/s | $Re_{ax}$ | $\xi$ | $u_{ax}$ m/s | $Re_{ax}$ | $\xi$ |
| 10.814 | 10377 | 0.471 | 10.82 | 10384 | 0.490 |
| 16.232 | 15484 | 0.431 | 10.24 | 15584 | 0.488 |
| 21.619 | 20746 | 0.414 | 21.66 | 20785 | 0.482 |
| 26.942 | 25854 | 0.406 | 27.06 | 25970 | 0.48 |

PA-92-24 t2

| Entrance Gap/Clearance = 50 | | | Entrance Gap/Clearance = 100 | | |
|---|---|---|---|---|---|
| $u_{ax}$ m/s | $Re_{ax}$ | $\xi$ | $u_{ax}$ m/s | $Re_{ax}$ | $\xi$ |
| 10.80 | 5181 | 0.562 | 10.797 | 5167 | 0.567 |
| 16.56 | 7945 | 0.54 | 16.176 | 7761 | 0.558 |
| 21.595 | 10361 | 0.526 | 21.55 | 10339 | 0.55 |
| 26.67 | 12796 | 0.51 | 26.934 | 12664 | 0.54 |
| 32.27 | 15484 | 0.493 | 32.24 | 15469 | 0.537 |
| 43.062 | 20667 | 0.478 | 42.533 | 20408 | 0.524 |

PA-92-24 t3

| Entrance Gap/Clearance = 50 | | | Entrance Gap/Clearance = 100 | | |
|---|---|---|---|---|---|
| $u_{ax}$ m/s | $Re_{ax}$ | $\xi$ | $u_{ax}$ m/s | $Re_{ax}$ | $\xi$ |
| 10.82 | 3461 | 0.66 | 10.75 | 3438 | 0.68 |
| 16.19 | 5178 | 0.65 | 16.09 | 5146 | 0.66 |
| 21.49 | 6874 | 0.647 | 21.47 | 6874 | 0.65 |
| 26.74 | 8553 | 0.637 | 26.81 | 8553 | 0.648 |
| 32.25 | 10315 | 0.628 | 32.176 | 10292 | 0.64 |
| 48.33 | 15461 | 0.606 | 47.87 | 15315 | 0.63 |
| 64.487 | 20630 | 0.595 | 64.165 | 20630 | 0.624 |

PA-92-24 t4

## 26. Five Cavity Straight-Through Labyrinth Seal with Straight Knives

Experimental data on mass flow coefficients at different seal clearances and seal pressure ratios are reported in Reference 40. Also reported are detailed pressure profiles along the seal length at one pressure ratio and different seal clearances. Computations were performed at three different pressure ratios and three clearance values for the flow coefficients comparison. Comparison of pressure profiles was done at four different clearance values. The computed results were compared with experimental data and excellent agreement was obtained. Flow geometry details and results of the calculations are discussed below.

Problem Specification

Computation of steady-state turbulent air flow in a 5 cavity, look-through, planar labyrinth seal at different pressure ratios and tip gaps.

Experimental Data

Experimental results by Willig *et al.*[40]

Grid

30 x 30 cells in each cavity, 8 to 12 cells in the tip gap, 30 cells in axial direction in the upstream and downstream, portions. Appropriate clustering of cells near walls.

Boundary Conditions

- Downstream pressure kept fixed, upstream pressure varied to match specified pressure ratio across the seal.
- Stationary walls on stator and rotor.
- Inlet k and $\varepsilon$ values specified using estimated inlet velocities.

Physical Models

- Compressible flow.
- Central differencing scheme with 0.1 damping.
- k-$\varepsilon$ model of turbulence with wall functions.

Results

- Flow geometry and parameters are shown in Figure 43.
- Flow solutions obtained at several pressure ratios across the seal, and at different tip gap values.
- Figure 44 shows the pressure profiles in the seal for a pressure ratio $p_u/p_d$ of 1.38 for four tip gaps. Computational and experimental values plotted for comparison.
- Figure 45 shows the non-dimensional mass flow coefficient ($\phi$) (see Reference 40 for definition) as a function of the seal pressure ratio at different tip gaps.

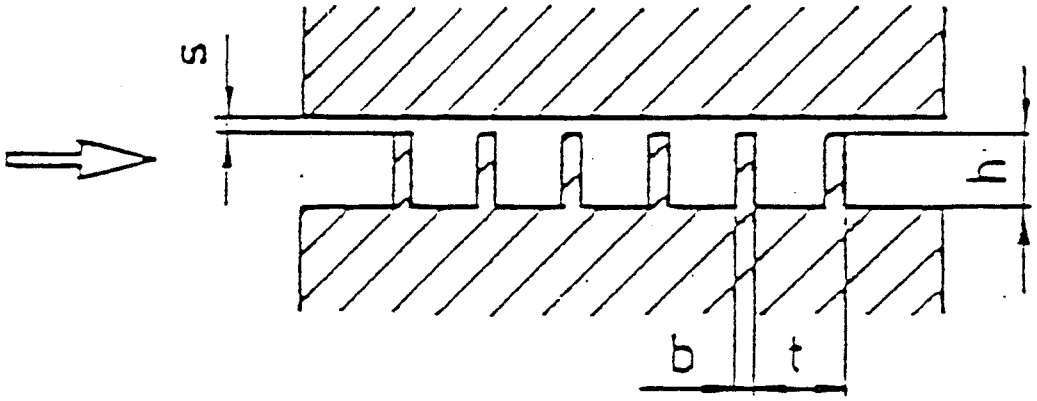


Figure 43. Details of the Flow Geometry for Five Cavity Look-Through Labyrinth Seal. b = 2.5, h = 10.5, t = 12, s = 0.5 - 2.52 (all dimensions in mm)

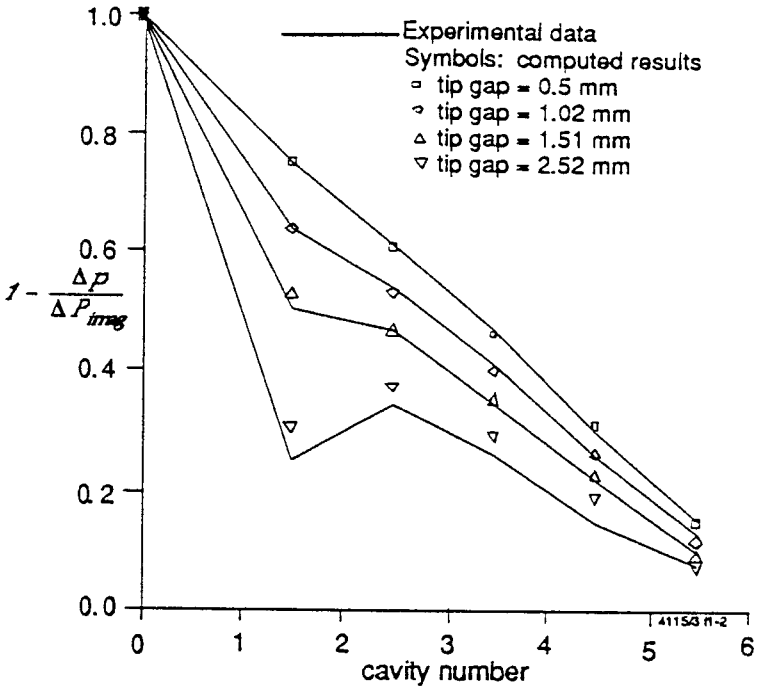


Figure 44. Non-Dimensionalized Pressure Drop at the Centers of the Cavities for a Pressure Ratio of 1.38

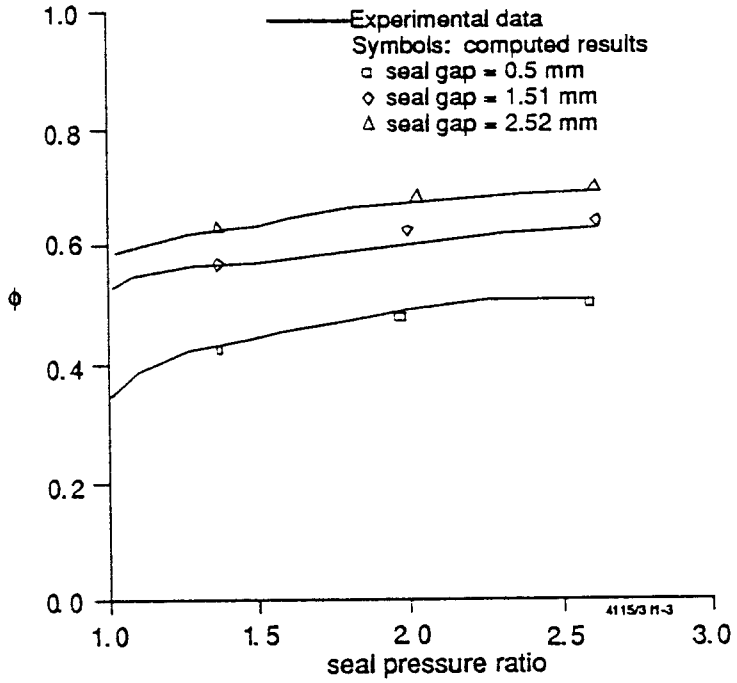


Figure 45. Mass Flow Coefficient ($\phi$) as a Function of Pressure Ratio Across the Seal

## 27. Two Cavity, Straight-Through Labyrinth Seal with Tapered Knives

Experimental[41] and computational[42] results for this case are available. Experimental data includes mass flow coefficients at different pressure ratios across the seal, and detailed pressure measurements in the seal for a fixed pressure ratio. Computations were performed at three different pressure ratios for comparison of flow coefficients as well as pressure profiles. Very good agreement was obtained between the computed and experimental pressure profiles, while the flow coefficient results show a good comparison, with some under prediction in computed results. Computational details and the results are given below.

Problem Specification

Computation of steady-state turbulent air flow in a two cavity, look-through, planar labyrinth seal with tapered knives.

Experimental Data

Experimental data by Tipton, *et al.*[41]

Grid

- 26 cells in the axial and 50 cells in the radial direction per cavity and 210 cells in the gap.
- 51 and 75 cells in the axial direction in the upstream and downstream directions, respectively.
- Grid is clustered near the rotor and stator walls.

Boundary Conditions:

- Exit pressure fixed, upstream pressure varied to match specified pressure ratio across the seal.
- Inlet k and $\varepsilon$ values specified using estimated inlet velocities.
- Wall conditions are specified along the stator and rotor walls.

Numerical and Physical Models:

- Central differencing with 0.1 damping.
- k-$\varepsilon$ model of turbulence with standard wall functions.

Results:

- Details of the flow domain are shown in Figure 46.
- Figures 47 and 48 show the pressure drops along the direction of flow (as a function of inlet pressure) measured near the stator and rotor surfaces, respectively. The inlet/exit pressure ratio is 2.0.
- The leakage mass flow rates through the seals for different inlet/exit pressure ratios are plotted in the form of a flow parameter, $\phi$ (see Reference 41 for definition) in Figure 49.

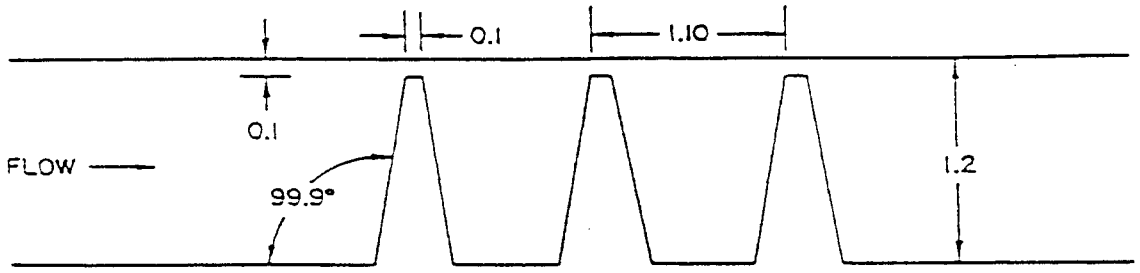


Figure 46. Flow Domain for the 3-Knife Labyrinth Seal. All dimensions are in inches. Upstream and downstream region lengths are 3 and 5 inches, respectively.

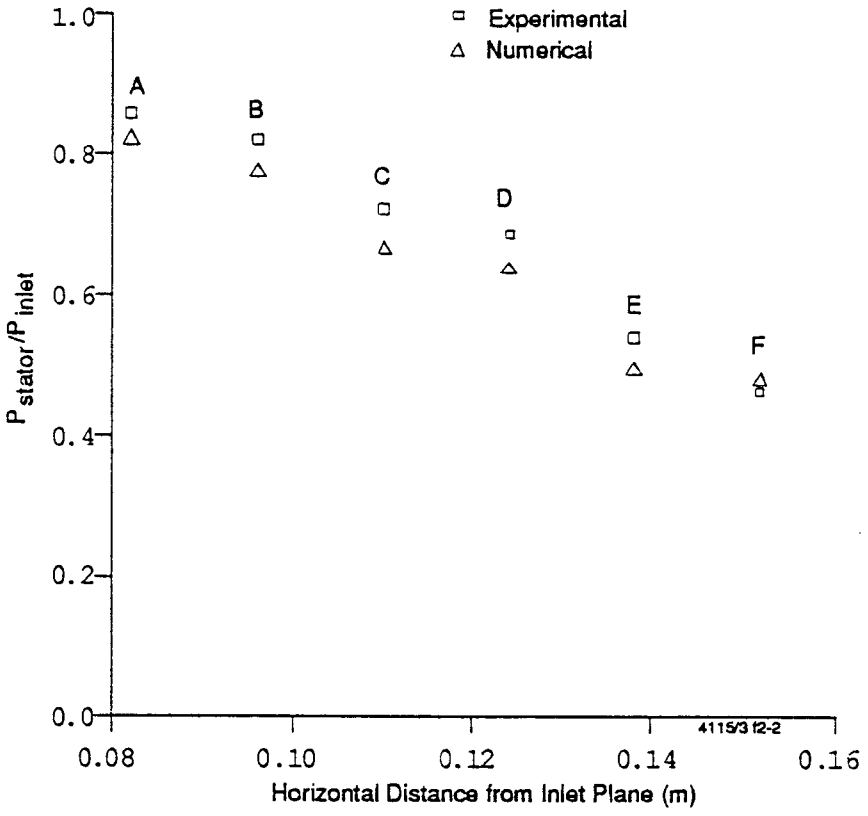


Figure 47. Pressure Drop Along the Stator Surface Plotted as a Function of Inlet Pressure Along the Seal Length. A: mid-point of 1st knife; B: mid-point of 1st cavity; C: mid-point of 2nd knife; D: mid-point of 2nd cavity; E: mid-point of 3rd knife; F: half of the cavity width downstream of 3rd knife. Inlet/Exit pressure ration = 2.0

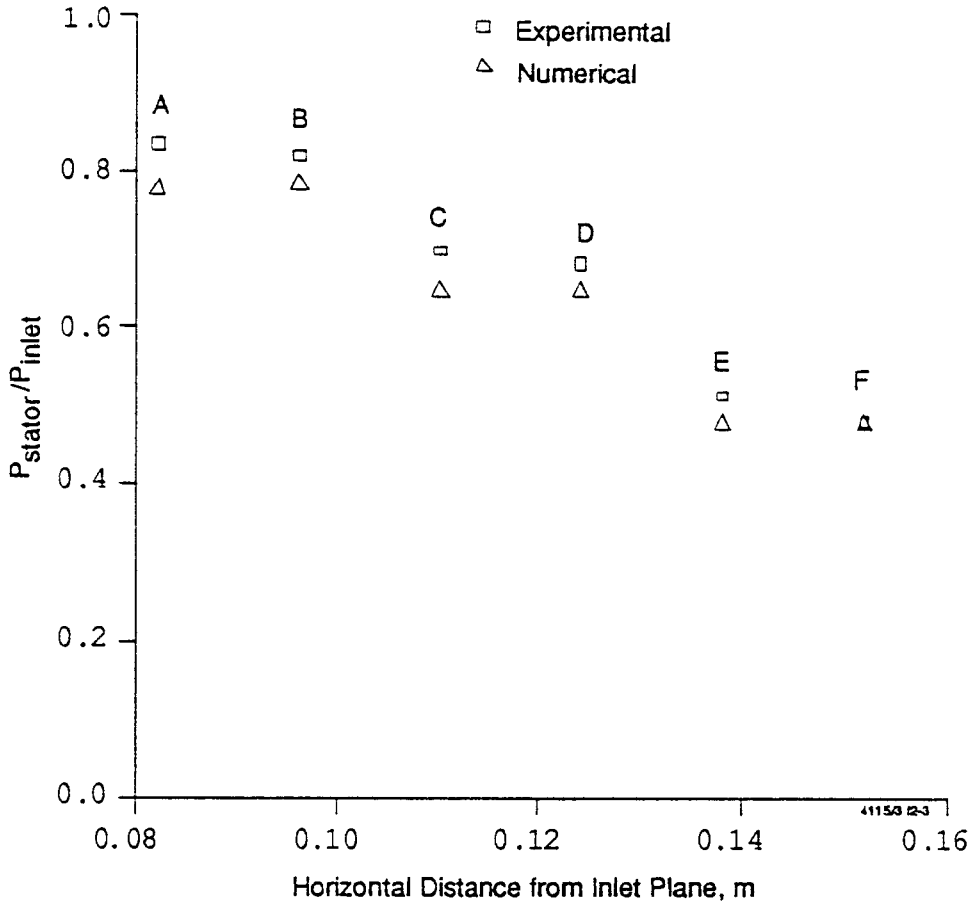


Figure 48. Pressure Drop Along the Rotor Surface Plotted as a Function of Inlet Pressure Along the Seal Length. A: mid-point of 1st knife; B: mid-point of 1st cavity; C: mid-point of 2nd knife; D: mid-point of 2nd cavity; E: mid-point of 3rd knife; F: half of the cavity width downstream of 3rd knife. Inlet/Exit pressure ration = 2.0

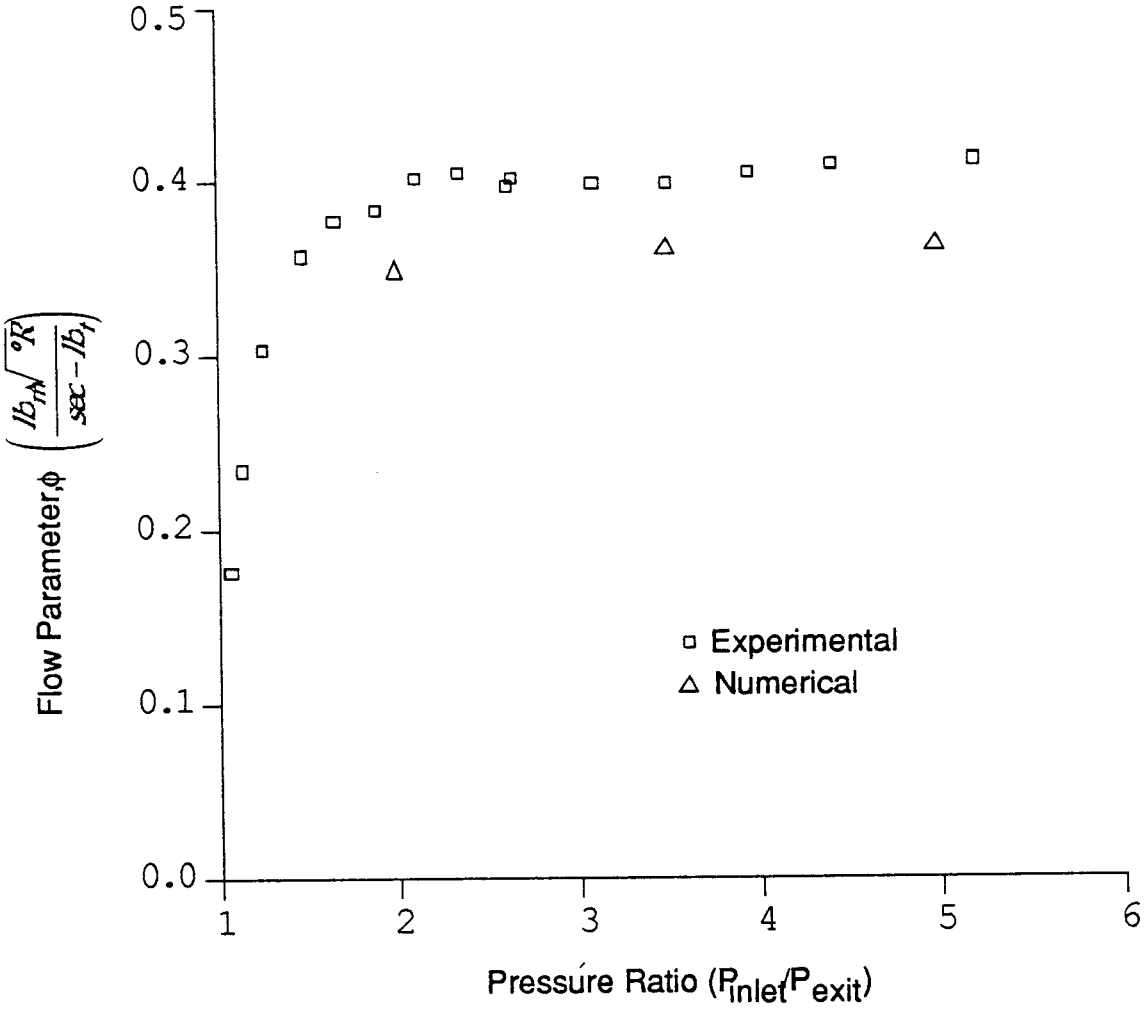


Figure 49. Leakage Mass Flow Rates

## 28. Two Cavity, Stepped Labyrinth Seal with Rectangular Knives

As in test case 26, experimental and computational data is available on flow coefficients and pressure profile in the seal for the stepped seal. Computations were done at three different pressure ratios for flow coefficients as well as pressure values in the seal. The comparison of flow coefficients is good, with somewhat higher flow coefficients predicted by the CFD code. This could partly be due to the upstream and downstream boundary condition definitions. The comparison of the pressures in the seal is very good. Details of the computations are shown below.

Problem Specification

Computational of steady-state turbulent air flow in a two cavity, stepped labyrinth seal with rectangular knives.

Experimental Data

Experimental data by Tipton, *et al.*[41]

Grid

- 26 cells in the axial direction in each cavity, 24 radial cells before the step and 53 radial cells after the step in the first cavity; 43 radial cells before the step and 62 radial cells after the step in the second cavity.
- 10 cells in the radial clearance and 5 cells in the axial direction between each knife tip and the stator wall.
- A 40 x 44 grid in the upstream region and a 60 x 52 grid in the downstream region.
- Grid is clustered near the rotor and stator walls.

Boundary Conditions

- Exit pressure fixed, upstream pressure varied to match specified ratio across the seal.
- Inlet values of k and $\varepsilon$ are calculated using estimated inlet velocities.
- Wall conditions are specified along the stator and rotor walls.

Numerical and Physical Models

- Central differencing with 0.1 damping.

- k-ε model for turbulence with standard wall functions.

Results

- Details of the flow domain are shown in Figure 50
- Figures 51 and 52 show the static pressures along the direction of flow (as a function on inlet pressure) measured near the stator and rotor surfaces, respectively. The inlet/exit pressure ratio is 2.0.
- The variation in flow parameter, $\phi$ (see Reference 41 for definition), with the inlet/exit pressure ratio is plotted in Figure 53.

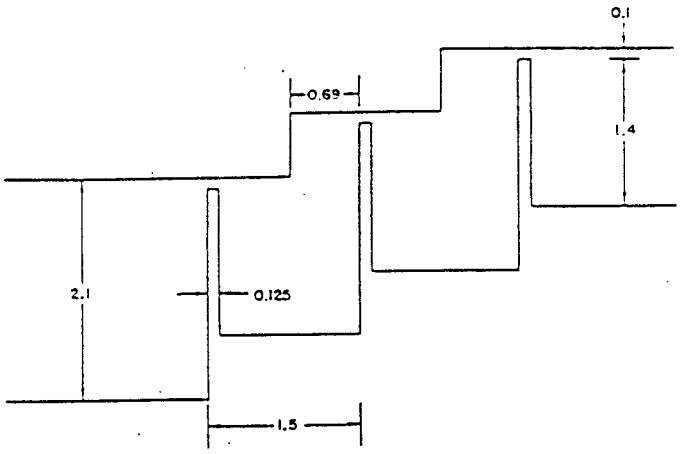


Figure 50. Details of the Flow Geometry of the Stepped Labyrinth Seal. All dimensions are in inches. Inlet and exit region lengths are 3 and 5 inches, respectively.

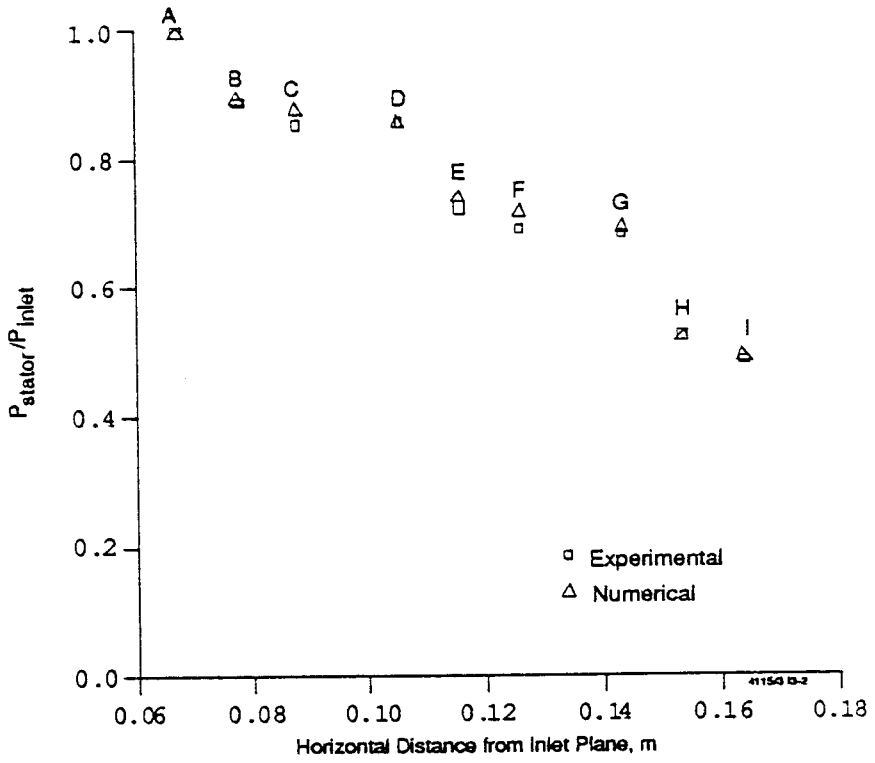


Figure 51. Pressure Drop Along the Stator Surface Plotted as a Function of Inlet Pressure Along the Seal Length. A: location upstream of 1st knife equidistant to location C from location B; B: mid-point of 1st knife; C: mid-point of region in 1st cavity before step; D: mid-point of region in 1st cavity after step; F: mid-pionot of region in 2nd cavity before step; G: mid-point region in 2nd cavity after step; H: mid-point of 3rd knife; I: location downstream of 3rd knife equidistant to location G from location H. Inlet/exit pressure ration = 2.0

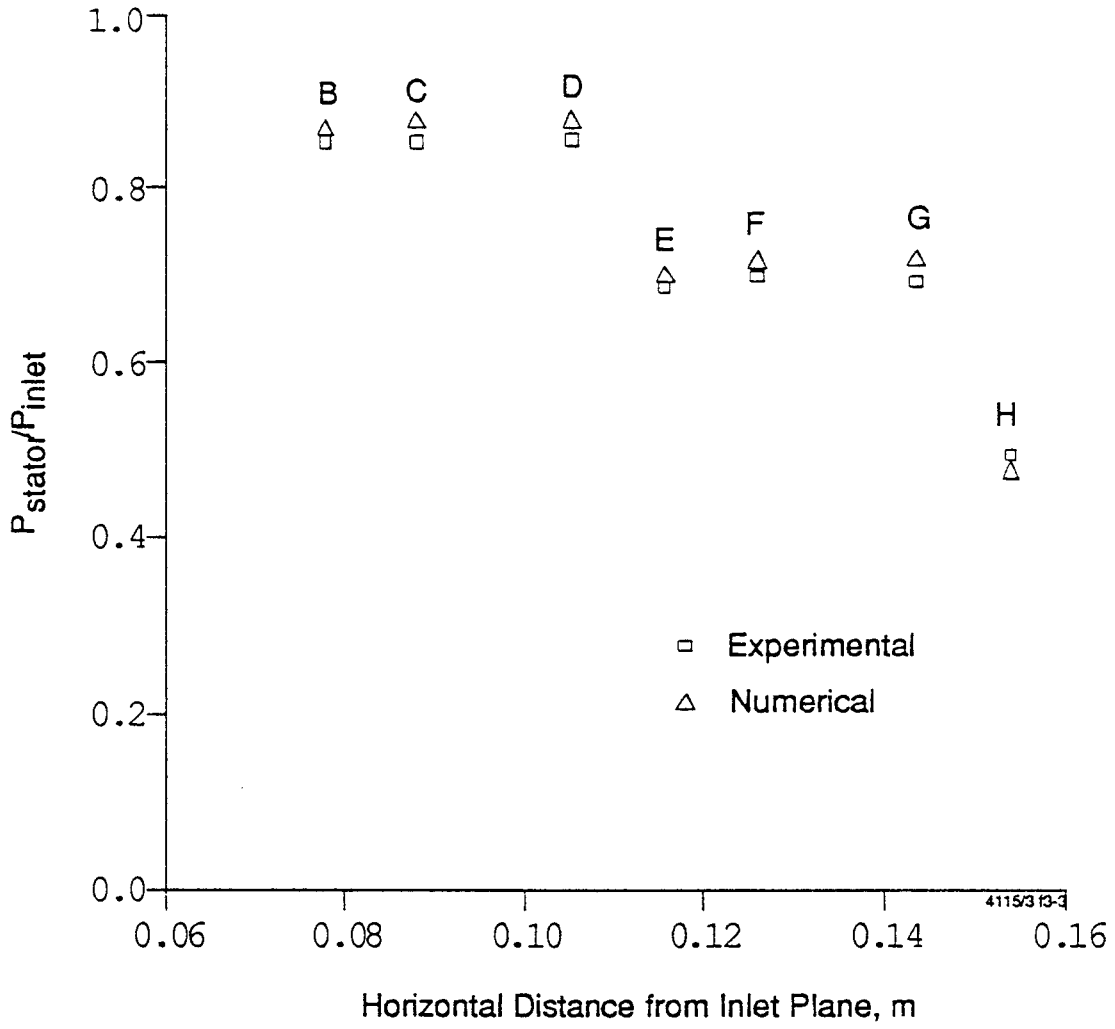


Figure 52. Pressure Drop Along the Rotor Surface Plotted as a Function of Inlet Pressure Along the Seal Length. B: mid-point of 1st knife; C: mid-point region in 1st cavity before step; D: mid-point of region in 1st cavity after step; E: mid-point of 2nd knife; F: mid-point of region in 2nd cavity before step; G: mid-point of region in 2nd cavity after step; H: mid-point of 3rd knife. Inlet/exit pressure ratio = 2.0

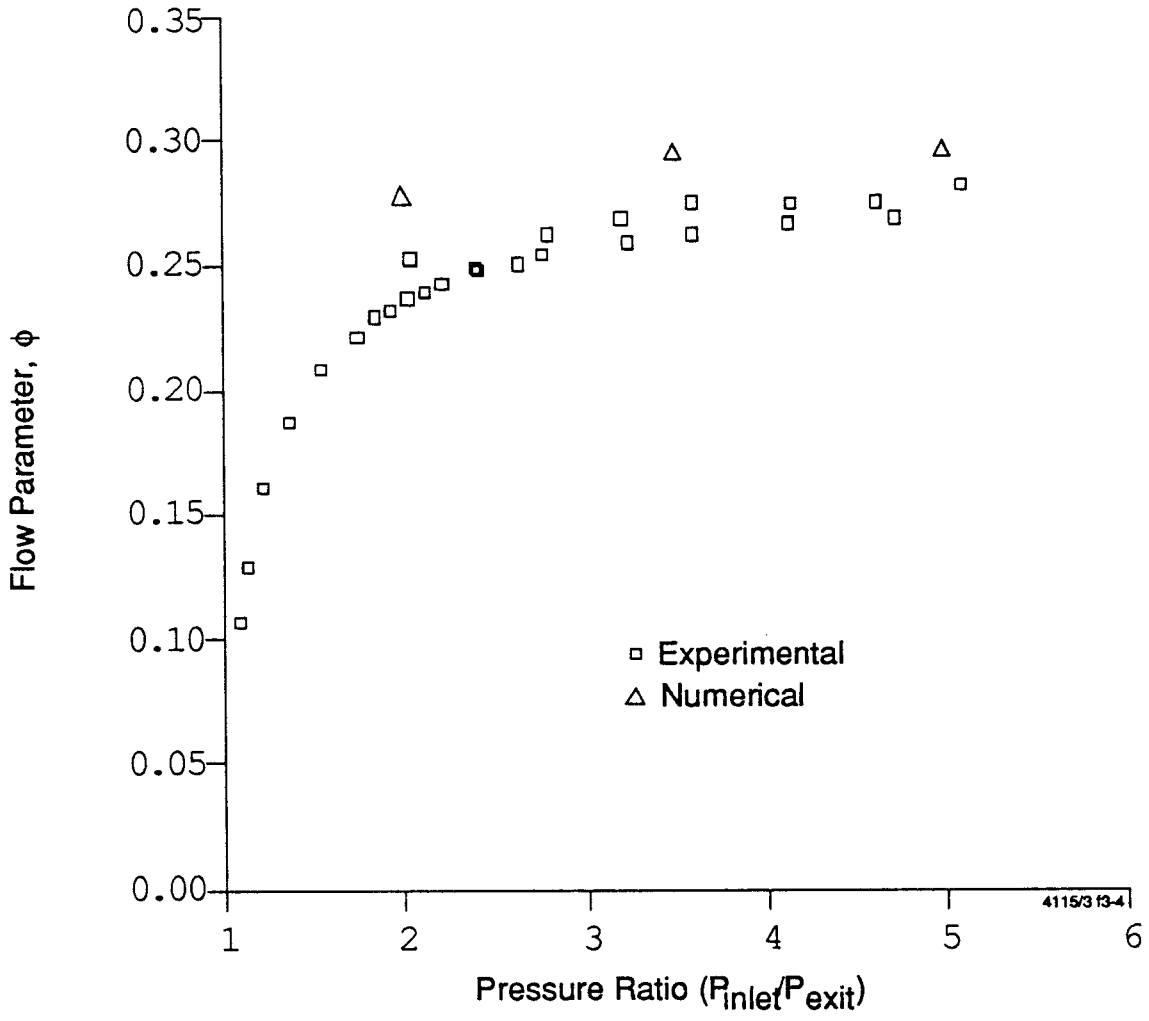


Figure 53. Flow Parameter as a Function of Inlet/Exit Pressure Ratio

## 29. Rotordynamic Coefficients for an Eccentric Annular Seal

Problem Specification

Computations of rotordynamics coefficients for an annular seal and incompressible flow at different static eccentricities.

Experimental Data

Experimental and numerical results as reported by Simon and Frene.[43]

Grid

- Seal radius = 80 mm, seal clearance = 0.36 mm, seal length = 40 mm.
- 10 cells in axial direction, 5 in radial gap and 30 in circumferential direction.

Boundary Conditions

- Specified upstream and downstream pressure values with an extreme loss factor $\xi = 0.5$.
- Stationery wall on stator, rotating wall on rotor with shaft speed = 4,000 rpm.

Physical Models

- Central differencing with 0.1 damping.
- Standard k-$\varepsilon$ model with wall functions.
- Perturbation method for rotordynamic coefficients.

Results

- Rotordynamics coefficients computer at static eccentricities ranging from 0 to 0.7.
- Direct stiffness $K_{yy}$ and $K_{zz}$ as well as $K_{yz}$ and $K_{zy}$ shown in Figures 54 through 57. Also shown are experimental results and other numerical results for comparison. Very good agreement between present results and experimental results is seen.

- Damping coefficients $C_{yy}$, $C_{zz}$, $C_{yz}$ and $C_{zy}$ shown in Figures 58 through 61. Comparison with other numerical results also shown, very good agreement is seen between the data sets.
- Inertia (mass) coefficient $M_{yy}$ and $M_{zz}$ shown in Figures 62 and 63.

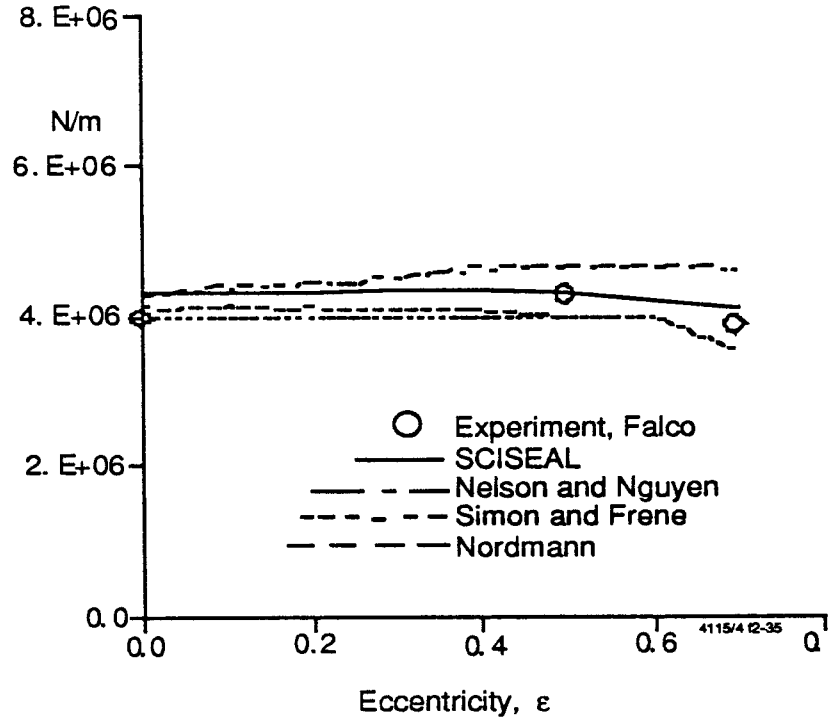


Figure 54. Direct Stiffness, $K_{yy}$, Annular Eccentric Seal

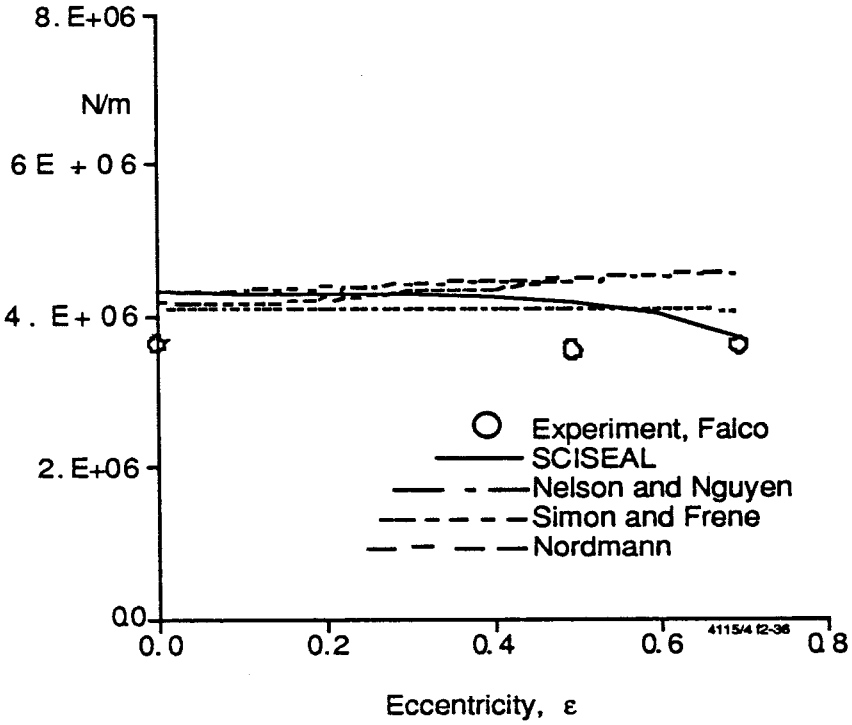


Figure 55. Direct Stiffness, $K_{zz}$, Annular Eccentric Seal

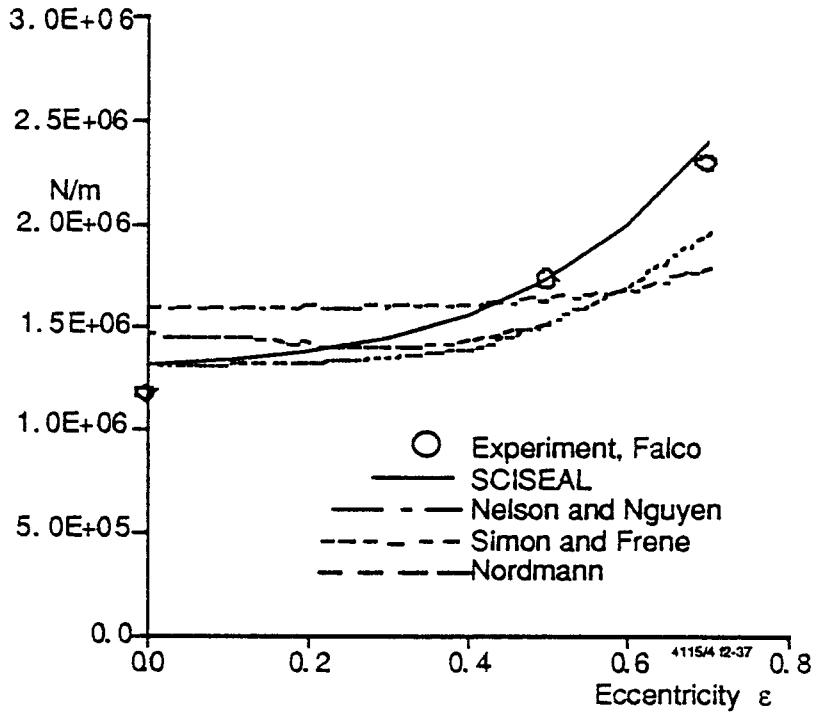


Figure 56. Cross Coupled Stiffness, $K_{yz}$, Annular Eccentric Seal

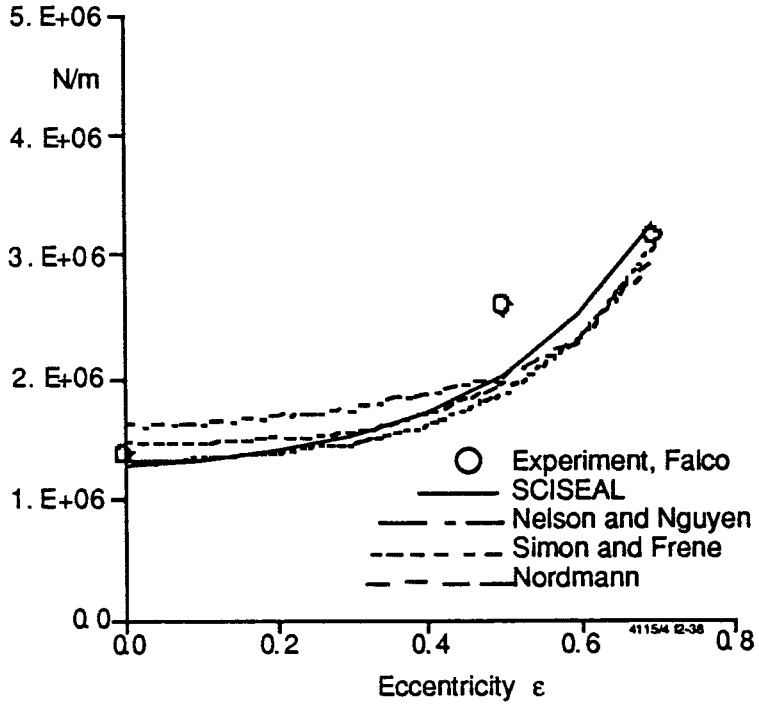


Figure 57. Cross Coupled Stiffness, $K_{zy}$, Annular Eccentric Seal

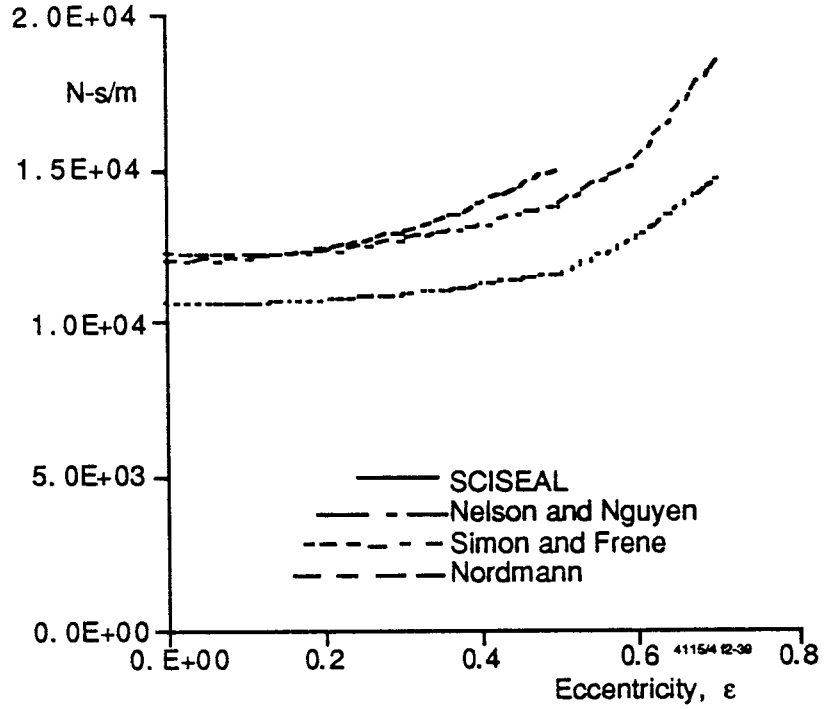


Figure 58. Direct Damping, $C_{yy}$, Annular Eccentric Seal

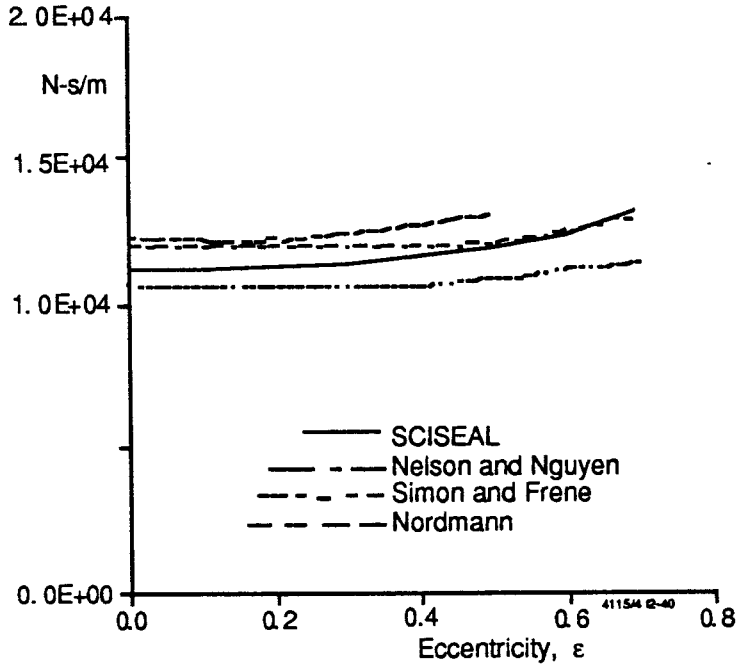


Figure 59. Direct Damping, $C_{zz}$, Annular Eccentric Seal

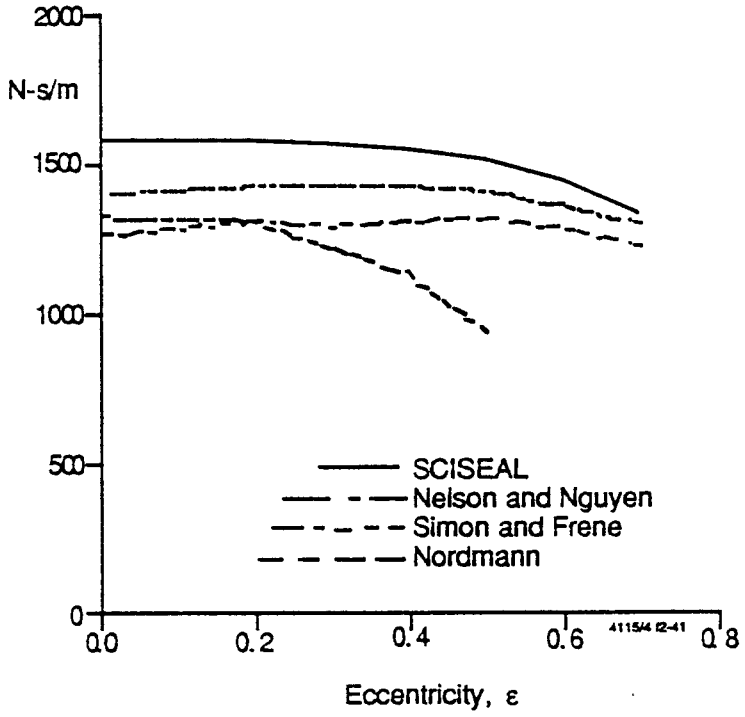


Figure 60. Cross Coupled Damping, $C_{yz}$, Annular Eccentric Seal

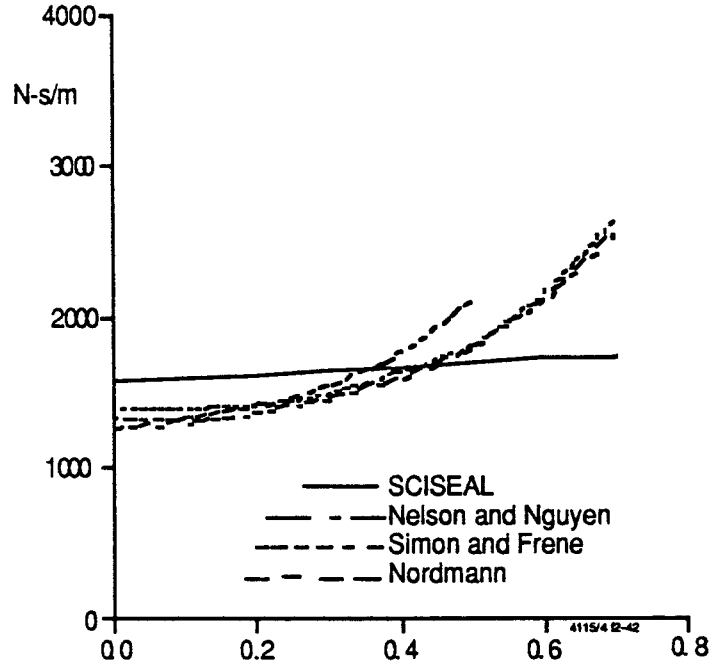


Figure 61. Cross Coupled Damping, $C_{zy}$, Annular Eccentric Seal

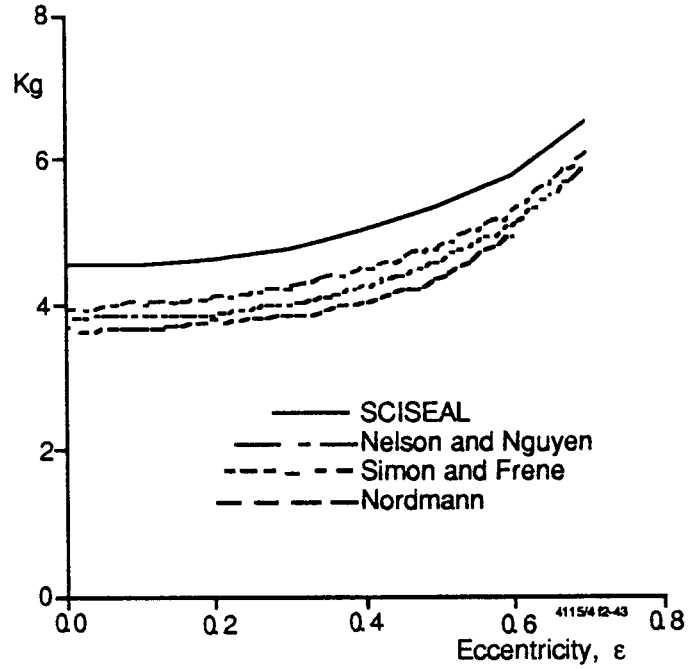


Figure 62. Direct Inertia, $M_{yy}$, Annular Eccentric Seal

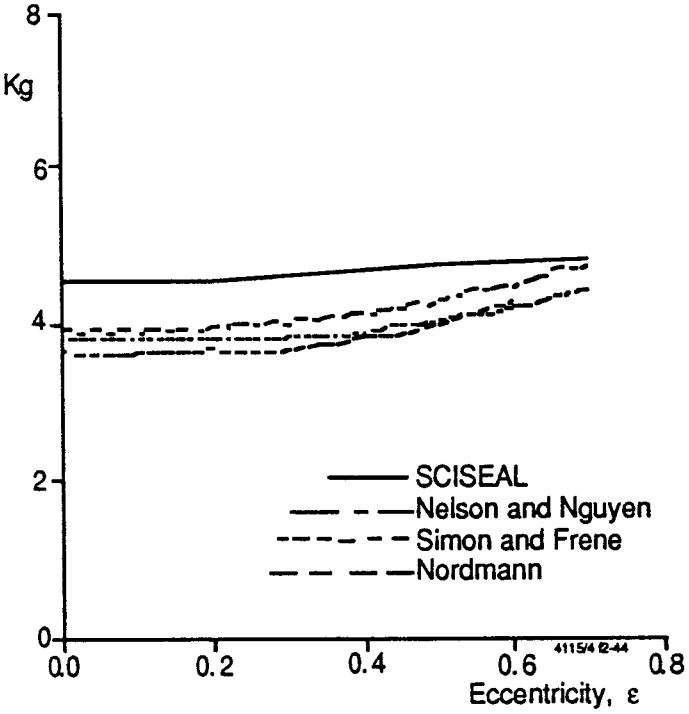


Figure 63. Direct Inertia, $M_{zz}$, Annular Eccentric Seal

## 30. Flow in a Whirling Annular Seal

Problem Specification

Computation of the flow in a whirling annular seal to investigate the behavior and comparison with experimental velocity and pressure measurements.

Grid, Geometry, Physical Models and Results

Please refer to Reference 45 for detailed description of the problem, boundary conditions and results.

## 31. Flow and Cooling Effectiveness of Rim Seals

Problem Specification

Evaluation of the flow in a generic disc cavity and rim seal configuration. Use passive scalar transport of a tracer gas to evaluate the cooling effectiveness of four different types of rim seals at different flow conditions and compare with experiments.

Grid, Geometry, Physical Models and Results

Please refer to Reference 48 for a detailed description of the problem and results

## 32. Interaction of Secondary Flow and Mainpath Flow in Multiple Disc Cavities

Problem Specification

Analysis of the flow dynamics in a multi-cavity turbine disc configuration. Account for the coupling between cavities and main path flow. Use tracer gas transport to identify flow features and compare with experimental date.

Grid, Geometry, Physical Models and Results

Please refer to Reference 50 for a detailed description of the problem and results

## 33. Flow and Conjugate Heat Transfer Analysis in Turbine Disc Cavities

Problem Description

Simulation of flow and heat transfer in the turbine disc cavities of an actual turbine engine (Allison T-56). Evaluate mass flow rates and gas temperatures at various rim seals, effect of interstage labyrinth seal and conjugate heat transfer in labyrinth seal support discs.

Grid, Geometry, Physical Models and Results

Please refer to Reference 52 for a detailed description of the problem and results

## 5.0 REFERENCES


1. SCISEAL: "A Computer Program for Study of Fluid Dynamic Forces in Seals," CFD Research Corporation, May 1995.
2. Thompson, J.F., Warsi, Z.U.A., and Mastin, C.W., *Numerical Grid Generation*, North-Holland, NY, 1985.
3. Cebeci, T. and Smith, A.M.O., *Analysis of Turbulent Boundary Layers*, Academic Press, New York, 1974.
4. First Interim Report, NASA Contract NAS3-25644, "Study of Fluid Dynamic Forces in Seals," Mechanical Technologies, Inc., 1991.
5. Harlow, F.H., and Welch, J.E., "Numerical Calculation of Time-Dependent Viscous Incompressible Flow of Fluid with Free Surface," *Physics Fluids*, vol. 8, pp. 2182-2189, 1965.
6. Rhie, C.M., and Chow, W.L., "Numerical Study of the Turbulent Flow Past an Airfoil with Trailing Edge Separation," *AIAA Journal*, vol. 21, pp. 1525-1532, 1983.
7. Peric, M., "A Finite-Volume Method for the Prediction of Three-Dimensional Fluid Flow in Complex Ducts," PhD Thesis, University of London, 1985.
8. Patankar, S.V. and Spalding, D.B., "A Calculation Procedure for Heat, Mass and Momentum Transfer in Three-Dimensional Parabolic Flows," *Int. J. Heat Mass Transfer*, vol. 15, pp. 1787-1806, 1972.
9. Van Doormal, J.P., and Raithby, G.D., "Enhancements of the SIMPLE Method for Predicting Incompressible Fluid Flows," *Numerical Heat Transfer*, vol. 7, pp. 147-163, 1984.
10. Issa, R.I., "Solution of the Implicitly Discretised Fluid Flow Equations by Operator-Splitting," *J. of Comp. Phys.*, Vol. 624, 1985, pp. 40-65
11. Demirdzic, I., and Peric, M., "Finite Volume Method for Prediction of Fluid Flow in Arbitrarily Shaped Domains with Moving Boundaries," *Int. J. of Num. Methods in Fluids*, vol. 10, pp. 771-790, 1990.
12. Baldwin, B.S. and Lomax, H., "Thin Layer Approximation and Algebraic Model for Separated Flows," AIAA Paper 78-257, 1978.
13. Launder, B.E., and Spalding, D.B., *Comp. Methods Appl. Mech. Eng.*, vol.3, p. 269, 1974.
14. Hanjalic, K., Launder, B.E., and Schiestel, R., "Multiple Time-Scale Concepts

in Turbulent Shear Flows," Turbulent Shear Flows, Eds. L. J. S. Bradbury, Springer Verlag, New York, 1980.

15. Fabris, G., Harsha, P.T., and Edelman, R.B., "Multiple-Scale Turbulence Modeling of Boundary Layer Flows for Scramjet Applications," NASA CR-3433, 1981.
16. Kim, S. W. and Chen, C.P., "A Multiple Time-Scale Turbulence Model Based on Variable Partitioning of Turbulent Kinetic Energy Spectrum," Paper No. AIAA-88-1771, 1988.
17. Patel, V. C., Rodi, W. and Scheuerer, G., "Turbulence Models for Near-Wall and Low Reynolds Number Flows: A Review," *AIAA Journal*, Vol. 23, No. 9, pp. 1308-1319, 1985.
18. Brankovic, A. and Stowers, S.T. "Review of Low-Reynolds Number Turbulence Models for Complex Internal Separated Flows," AIAA-88-3006. 1988.
19. Avva, R.K., Smith, C.E., and Singhal, A.K., "Comparative Study of High and Low Reynolds Number Versions of k-ε Models," AIAA-90-0246, Aerospace Sciences Meeting, 1990.
20. Chien, K. Y., "Predictions of Channel and Boundary-Layer Flows with Low-Reynolds-Number Turbulence Model," *AIAA J.*, Vol. 20, pp. 33-38, 1982.
21. Rodi, W., "Experience wit Two-Layer Models Combining the k-ε Model with a One-Equation Model Near the Wall," AIAA-91-0216, 29th Aerospace Sciences Meeting, 1991.
22. Nordmann, R., and Dietzen, F.J., "Finite Difference Analysis of Rotordynamic Seal Coefficients for an Eccentric Shaft Position," NASA CP-3026, Workshop on Rotordynamic Stability Problems in High Performance Turbomachinery, College Station, TX 1988.
23. Schlicting, H., *Boundary Layer Theory*, McGraw-Hill, 1979.
24. Ghia, U., Ghia, K.N., and Shin, C.T., "High-Re Solutions for Incompressible Flow Using the Navier-Stokes Equations and a Multi-Grid Method," *J. of Comp. Physics*, vol. 48, pp. 387-411, 1982.
25. Armaly, B.F., Durst, F., Pareira, J.C.F., and Schonung, B., "Experimental and Theoretical Investigation of Backward-Facing Step Flow," *J. Fluid Mech.*, vol. 127, pp. 473-496, 1983.
26. Laufer, J., "Investigation of Turbulent Flow in a Two-Dimensional Channel," NASA Report 1053, 1951.

27. Daily, J.W., and Nece, R.E., "Chamber Dimension Effects of Induced Flow and Frictional Resistance of Enclosed Rotating Disks," *Trans. of ASME, J. of Basic Eng.*, vol. 82, pp. 217-232, 1960.
28. Dibelius, G., Rodtke, F., and Ziemann, M., "Experiments on Friction, Velocity, and Pressure Distribution of Rotating Disks," D.E. Metzger and N.H. Afgan ed.s, *Heat and Mass Transfer in Rotating Machinery*, pp. 117-136, 1984.
29. Morrison, G.L., Johnson, M.C., and Tatterson, G.B., ""Three-Dimensional Laser Anemometer Measurements in an Annular Seal," *Trans. ASME J. of Trib.*, vol. 113, pp. 421-427, 1991.
30. Morrison, G.L., Johnson, M.C., and Tatterson, G.B., "3-D Laser Anemometer Measures in a Labyrinth Seal," *Trans. ASME, J. of Eng. for Gas Turbines and Power*, vol. 113, pp. 119-125, 1991.
31. Athavale, M.M., Przekwas, A.J., and Hendricks, R.C., "A Numerical Study of the Flow Field in Enclosed Turbine Disk Cavities in Gas Turbine Engines," presented at the Fourth International Symposium on Transport Phenomena and Dynamics of Rotating Machinery, (ISROMAC-4), Honolulu HA, 1992.
32. Taylor, A.M.K.P., Whitelaw, J.H., Yianneskies, M., "Measurements of Laminar and Turbulent Flow in a Curved Duct with Thin Inlet Boundary Layers," NASA CR-3367, 1981.
33. Athavale, M.M., Przekwas, A.J., and Hendricks, R.C., "Driven Cavity Simulation of Turbomachinery Blade Flows with Vortex Control," AIAA-93-0390, Jan. 1993.
34. Fuller, D.D., *Theory and Practice of Lubrication for Engineers*, pp. 364-365, 1984.
35. Cameron, A., *Principles of Lubrication*, Longman's, pp. 308-313, 1966.
36. Dietzen, F.J., and Nordmann, R., "Calculating Rotordynamic Coefficients of Seals by Finite-Difference Techniques," *Trans. ASME J. of Trib.*, vol. 109, pp. 388-394, 1987.
37. Nelson, C.C., "Rotordynamic Coefficients for Compressible Flow in Tapered Annular Seals," *Trans. ASME J. of Trib.*, vol. 107, pp. 318-325, 1985.
38. Kanemori, Y., and Iwatsubo, T., "Experimental Study of Dynamic Fluid Forces and Moments for a Long Annular Seal," *Trans. ASME, J. of Trib.*, vol. 114, pp. 773-778, 1992.
39. Athavale, M.M., Przekwas, A.J., and Hendricks, R.C., "A 3-D CFD Code for Accurate Prediction of Fluid Flows and Fluid Forces in Seals," 7th Workshop

for Rotordynamic Instabilities in High-Performance Turbomachinery, College Station, TX, 1993.

40. Witting, S., Shelling, U., Kim, S., and Jacobsen, K., "Numerical Predictions and Measurements of Discharge Coefficients in Labyrinth Seals," ASME Paper 87-GT-88, 32nd Gas Turbine Conference and Exhibition, Anaheim, CA, 1987.
41. Tipton, D.L., Scott, T.E., and Vogel, G.E., "Labyrinth Seal Analysis, Volume III: Analytical and Experimental Development of a Design Model for Labyrinth Seals," AFWAL-TR-85-2103, 1986.
42. Buggeln, R.C., and McDonald, H., "Labyrinth Seal Analysis, Vol. 1: Development of a Navier-Stokes Analysis for Labyrinth Seals," AFWAL-TR-85-2103, 1986.
43. Simon, F., and Frene, J., "Analysis for Incompressible Flow in Annular Pressure Seals," ASME Paper 91-Trib-50, presented at the STLE/ASME Tribology Conference, St. Louis, MO, 1991.
44. Athavale, M.M., Hendricks, R.C., and Steinetz, B.M., "Numerical Simulation of Flow in a Whirling Annular Seal and Comparison with Experiments," NASA TM-106961, July 1995.
45. Thames, H.D., III, "Mean Flow and Turbulence Characteristics in Whirling Annular Seals," M.S. Thesis, Texas A&M University, May 1992.
46. Morrison, G.L., DeOtte, R.E., Jr., and Thames, H.D., III, "Experimental Study of the Flow Field Inside a Whirling Annular Seal," *Tribology Trans.*, Vol. 113, pp. 425-429, 1994.
47. Winslow, R.B., "Dynamic Pressure and Shear Stress Measurements on the Stator Wall of Whirling Annular Seals," M.S. Thesis, Texas A&M University, 1994.
48. Przekwas, A.J., Athavale, M.M., Hendricks, R.C., "Progress in Advanced Modeling of Turbine Engine Seal Flows," AIAA-94-2803, AIAA 30th Joint Propulsion Conference, Indianapolis, IN June 1994.
49. Graber, D.J., Daniels, W.A., and Johnson, B.V., "Disk Pumping Test," AFWAL-TR-87-2050, 1987.
50. Athavale, M.M., Przekwas, A.J., Hendricks, R.C., and Steinetz, B.M., "Numerical Analysis of Intra-Cavity and Power-stream Flow Interaction in Multiple Gas-Turbine Disc Cavities, ASME Paper 95-GT-325, International Gas Turbine and Aeroengine Congress and Exposition, Houston, TX, June 1995.
51. Daniels W.A., and Johnson, B.V., "Experimental Investigation of Turbine

Disk Cavity Aerodynamics and Heat Transfer," Contractor Report, Contract NAS8-37462, VTRC Report 93-957878-27, 1993.

52. Athavale, M.M., Ho, Y.H., Forry, J.M., Munson, J.H., Hendricks, R.C. and Steinetz, B.M., "Simulation of Secondary Flow in Gas Turbine Disc Cavities and Interaction with the Main Flow Path," AIAA-95-2620, AIAA 31st Joint Propulsion Conference, San Diego, CA, July 1995.

# REPORT DOCUMENTATION PAGE

*Form Approved*
*OMB No. 0704-0188*



| 1. AGENCY USE ONLY (*Leave blank*) | 2. REPORT DATE | 3. REPORT TYPE AND DATES COVERED |
|---|---|---|
| | October 2004 | Final Contractor Report |

**4. TITLE AND SUBTITLE**

Numerical, Analytical, Experimental Study of Fluid Dynamic Forces in Seals
Volume 6—Description of Scientific CFD Code SCISEAL

**5. FUNDING NUMBERS**

WBS–22–5000–0013
NAS3–25644

**6. AUTHOR(S)**

Mahesh Athavale and Andrzej Przekwas

**7. PERFORMING ORGANIZATION NAME(S) AND ADDRESS(ES)**

CFD Research Corporation
215 Wynn Drive
Huntsville, Alabama 35805

**8. PERFORMING ORGANIZATION REPORT NUMBER**

E–14708–6

**9. SPONSORING/MONITORING AGENCY NAME(S) AND ADDRESS(ES)**

National Aeronautics and Space Administration
Washington, DC 20546–0001

**10. SPONSORING/MONITORING AGENCY REPORT NUMBER**

NASA CR—2004-213199-VOL6

**11. SUPPLEMENTARY NOTES**

Project Manager, Anita D. Liang, Aeronautics Directorate, NASA Glenn Research Center, organization code 2200, 216–977–7439. Responsible person, Robert C. Hendricks, Research and Technology Directorate, NASA Glenn Research Center, organization code 5000, 216–977–7507.

**12a. DISTRIBUTION/AVAILABILITY STATEMENT**

Unclassified - Unlimited
Subject Categories: 07, 20, and 34 Distribution: Nonstandard

Available electronically at http://gltrs.grc.nasa.gov

This publication is available from the NASA Center for AeroSpace Information, 301–621–0390.

**12b. DISTRIBUTION CODE**

**13. ABSTRACT** ***(Maximum 200 words)***

The objectives of the program were to develop computational fluid dynamics (CFD) codes and simpler industrial codes for analyzing and designing advanced seals for air-breathing and space propulsion engines. The CFD code SCISEAL is capable of producing full three-dimensional flow field information for a variety of cylindrical configurations. An implicit multidomain capability allow the division of complex flow domains to allow optimum use of computational cells. SCISEAL also has the unique capability to produce cross-coupled stiffness and damping coefficients for rotordynamic computations. The industrial codes consist of a series of separate stand-alone modules designed for expeditious parametric analyses and optimization of a wide variety of cylindrical and face seals. Coupled through a Knowledge-Based System (KBS) that provides a user-friendly Graphical User Interface (GUI), the industrial codes are PC based using an OS/2 operating system. These codes were designed to treat film seals where a clearance exists between the rotating and stationary components. Leakage is inhibited by surface roughness, small but stiff clearance films, and viscous pumping devices. The codes have demonstrated to be a valuable resource for seal development of future air-breathing and space propulsion engines.

**14. SUBJECT TERMS**

CFD seal code; Industrial seal codes; User-friendly seal codes; Fluid-film seal codes; Clearance seal codes; Seals; Dynamics; Design; Computational analysis; Fluid forces

**15. NUMBER OF PAGES**

161

**16. PRICE CODE**

| 17. SECURITY CLASSIFICATION OF REPORT | 18. SECURITY CLASSIFICATION OF THIS PAGE | 19. SECURITY CLASSIFICATION OF ABSTRACT | 20. LIMITATION OF ABSTRACT |
|---|---|---|---|
| Unclassified | Unclassified | Unclassified | |